



universität
wien

DIPLOMARBEIT

Titel der Diplomarbeit

Application of 3D tomography methods on a seismic 3D data set

angestrebter akademischer Grad

Magister der Naturwissenschaften (Mag. rer.nat.)

Verfasser: Klaus Mayer
Matrikelnummer: 9801587
Studienrichtung: Geophysik
Betreuer: O. Univ. Prof. Dipl.-Ing. Dr. Ewald Brückl
Institut für Geodäsie und Geophysik
Technische Universität Wien

Wien, im November 2008

Table of contents

| | | |
|----------|--|-----------|
| 1 | INTRODUCTION | 1 |
| 1.1 | Importance of the topic | 1 |
| 1.2 | Objectives | 2 |
| 1.3 | Modelling strategy | 2 |
| 2 | 3D SEISMIC SURVEY WASCHBERGZONE 1 | 2 |
| 2.1 | Geographical location of the survey area | 3 |
| 2.2 | Geology of the survey area | 3 |
| 2.3 | Data acquisition | 6 |
| 2.4 | Static correction | 8 |
| 3 | PRE-PROCESSING OF A SELECTED DATA SET | 11 |
| 3.1 | Pre-processing by OMV | 11 |
| 3.2 | Preparation of data | 14 |
| 3.2.1 | Geometry specification and picking of travel times from single fold traces | 14 |
| 3.2.2 | Application of stacking and picking of travel times from stacked traces | 18 |
| 4 | TRAVEL TIME MODELLING AND PRINCIPLES OF INVERSION TECHNIQUES | 24 |
| 4.1 | Fundamentals of elastic waves and ray theory | 24 |
| 4.1.1 | Basic definitions and relations | 24 |
| 4.1.2 | Stress tensor | 25 |
| 4.1.3 | Equation of motion | 27 |
| 4.1.4 | Separation of the equation of motion | 28 |
| 4.1.5 | The Eikonal equation | 29 |
| 4.1.6 | The ray tracing system and Fermat's principle for seismic rays | 30 |
| 4.2 | Inverse theory | 32 |
| 4.2.1 | Fundamentals of inverse problems | 33 |
| 4.2.2 | Simultaneous iterative reconstruction technique (SIRT) | 38 |
| 4.2.3 | Nonlinear 3D seismic travel time tomography | 39 |
| 4.2.4 | Seismic tomography based on 1D ray tracing and inversion | 41 |

| | | | |
|------------|--|--------------|--------------|
| 5 | APPLICATION OF SEISMIC TRAVEL TIME TOMOGRAPHY | _____ | _____ |
| | ON A SELECTED 3D DATA SET | _____ | 49 |
| 5.1 | Generation of 1D travel times and inversion | _____ | 49 |
| 5.1.1 | Inversion of travel times to a velocity-depth model | _____ | 49 |
| 5.1.2 | Composition and quality control of the seismic model | _____ | 54 |
| 5.1.3 | Visualization of a three dimensional velocity model | _____ | 55 |
| 5.2 | 3D travel time tomography with different initial models | _____ | 62 |
| 5.2.1 | Processing of nonlinear 3D travel time tomography | _____ | 62 |
| 5.2.2 | 1D and 3D starting models for travel time tomography | _____ | 64 |
| 5.2.3 | Results | _____ | 66 |
| 5.3 | Comparison of velocity models | _____ | 74 |
| 6 | STATIC CORRECTION | _____ | 77 |
| 6.1 | Computation of static correction | _____ | 77 |
| 6.2 | Comparison of static corrections with uphole times | _____ | 81 |
| 7 | CONCLUSIONS | _____ | 83 |
| 8 | REFERENCES | _____ | VIII |
| 9 | ABSTRACT | _____ | XI |
| 10 | APPENDIX | _____ | XII |
| 11 | CURRICULUM VITAE | _____ | XIII |

I Table of figures

| | |
|--|----|
| Figure 1: Geographically position of the Waschbergzone 3D survey area..... | 3 |
| Figure 2: Tectonically map of Weinviertel/Lower Austria..... | 4 |
| Figure 3: Geological cross section through the Waschberg unit/Lower Austria. | 4 |
| Figure 4: Development of turbidity currents..... | 5 |
| Figure 5: Bouma sequence | 5 |
| Figure 6: The Waschbergzone | 6 |
| Figure 7: Positions of receivers and sources | 7 |
| Figure 8: Schematically description of components of datum static correction | 9 |
| Figure 9: wave equation datuming..... | 10 |
| Figure 10: Illustration of basic steps of pre-processing | 11 |
| Figure 11: Extracting internal data information to database..... | 14 |
| Figure 12: Specification of geometry..... | 15 |
| Figure 13: Assigning of geometrical information..... | 15 |
| Figure 14: Processing flow 03-display..... | 16 |
| Figure 15: Demonstration of travel time picking on amplitude maximum..... | 17 |
| Figure 16: The layout of the 3D Waschbergzone1 | 18 |
| Figure 17: CMP assumption for a non flat layered structure..... | 19 |
| Figure 18: Grid raster | 20 |
| Figure 19: Scheme of a common midpoint sorting sequence. | 21 |
| Figure 20: Overview of the stacking and picking process | 21 |
| Figure 21: Offset bin stack of cell 7002200..... | 22 |
| Figure 22: Offset bin stack of cell 90009300..... | 23 |
| Figure 23: Offset bin stack of cell 70006000..... | 23 |
| Figure 24: Offset bin stack of cell 70006500..... | 23 |
| Figure 25: Deformation of an arbitrary body..... | 25 |
| Figure 26: The stress tensor and its components | 26 |
| Figure 27: Graphically representation of the singular value decomposition. | 36 |
| Figure 28: Separation of U , S^{-1} and V into submatrices..... | 37 |
| Figure 29: Affects of epsilon ε on the rank of the diagonal matrix S | 38 |
| Figure 30: Illustration of SIRT..... | 39 |
| Figure 31: 3D travel time tomography..... | 40 |
| Figure 32: Vidale's finite difference algorithm | 41 |
| Figure 33: Flowchart of 1D ray tracing and inversion..... | 42 |
| Figure 34: Ray tracing in a flat layered structure..... | 43 |
| Figure 35: Weighting curves for two weighting factors. | 46 |
| Figure 36: Graphically description of matrix W' | 47 |
| Figure 37: Illustration of using the default gradient δ_s | 48 |
| Figure 38: Illustrating of processing steps for a typical seismic tomography..... | 49 |
| Figure 39: Four initial models for 1D ray tracing and inversion | 50 |
| Figure 40: The offset bin stack of cell 8002000 | 51 |
| Figure 41: The offset bin stack of cell 9002400 | 52 |
| Figure 42: The offset bin stack of cell 10004800 | 53 |
| Figure 43: Deleting outliers by visually inspection | 54 |
| Figure 44: Illustration of a Voxet..... | 55 |

| | |
|---|-----|
| Figure 45: Depth slices along the z-axis (w-axis)..... | 56 |
| Figure 46: Cross sections along the x-axis (u-axis) | 57 |
| Figure 47: Cross sections along the y-axis (v-axis) | 58 |
| Figure 48: Depth slices along the z-axis (w-axis)..... | 59 |
| Figure 49: Cross sections along the x-axis (u-axis). | 60 |
| Figure 50: Cross sections along the y-axis (v-axis). | 61 |
| Figure 51: Schematically 2D velocity model..... | 62 |
| Figure 52: Depth slice through the model..... | 62 |
| Figure 53: The entire layout divided into two overlapping parts..... | 64 |
| Figure 54: 1D velocity function | 65 |
| Figure 55: Strongly smoothed 3D initial model..... | 65 |
| Figure 56: Depth slices along the z-axis (w-axis)..... | 68 |
| Figure 57: Depth slices along the z-axis (w-axis)..... | 69 |
| Figure 58: Cross sections along the x-axis (u-axis) | 70 |
| Figure 59: Cross sections along the x-axis (u-axis) | 71 |
| Figure 60: Cross sections along the y-axis (v-axis) | 72 |
| Figure 61: Cross sections along the y-axis (v-axis) | 73 |
| Figure 62: Mean velocity models..... | 74 |
| Figure 63: Model coverage as a function of depth..... | 75 |
| Figure 64: Standard deviation. | 75 |
| Figure 65: Iso-surfaces with constant velocity..... | 76 |
| Figure 66: Typical depth slice and cross section | 76 |
| Figure 67: Static corrections based on the mean velocities. | 77 |
| Figure 68: Static corrections down to a datum | 79 |
| Figure 69: Static corrections down to a datum | 80 |
| Figure 70: Model differences between calculated static corrections | 81 |
| Figure 71: The uphole measurements in the selected survey area..... | 82 |
| Figure 72: Cross section through V_H^{3D} along the x-axis at borehole WBZ 7..... | 83 |
| Figure 73: Height correlation of model T_1 | XII |
| Figure 74: Height correlation of model T_2 | XII |
| Figure 75: Height correlation of model T_3 | XII |

II Index of tables

| | |
|---|----|
| Table 1: Summary of the most important acquisition parameters | 8 |
| Table 2: ASCII files containing ten significant parameters for processing. | 17 |
| Table 3: Dimension and resolution of the final velocity model V_{lv}^{1D} | 55 |
| Table 4: <i>.hip file</i> with associated parameters | 63 |
| Table 5: <i>.hir file</i> with associated parameters..... | 63 |
| Table 6: Processing control file | 63 |
| Table 7: Geometric parameters | 64 |
| Table 8: 3D grid with cubic spaced velocity nodes. | 65 |
| Table 9: Iteration report of V_H^{1D} (part one) | 66 |
| Table 10: Iteration report of V_H^{1D} (part two) | 66 |
| Table 11: Iteration report of V_H^{3D} (part one) | 66 |
| Table 12: Iteration report of V_H^{3D} (part two)..... | 67 |
| Table 13: Dimension and resolution of V_H^{1D} and V_H^{3D} | 67 |
| Table 14: Significant parameters of static models with datum at 150[m] | 78 |
| Table 15: Significant parameters of static models with datum at 0[m] | 80 |

III Acknowledgements

I want to thank my parents and Karin for enduring my tension and supporting me during my study. I am very beholden to Prof. Dr. Ewald Brückl for the possibility to write my thesis at the Vienna University of Technology and for supervising it. I also want to thank the staff of the Institute of Geodesy and Geophysics, in particular Dr. Michael Behm and Mag. Werner Chwatal for their personal support. Finally, I am grateful to Mag. Bernhard Novotny from the OMV Department of Exploration and Production for providing the data for this study.

1 Introduction

1.1 Importance of the topic

This diploma thesis relies on one of the main differences between marine- and land-seismic processing and the fact that reflection waves are often affected by irregularities of the topography and in the near surface. Errors in geometry specification and near surface analysis have a considerably more deteriorious effect on the final product and so it is worthwhile to take this vitally important part of processing serious. Reducing topographic effects is normally introduced under the title of statics and field statics. *Sheriff, R.E., (1991)* defines in his encyclopaedia static correction as follows:

“Correction applied to seismic data to compensate for the effects of variation in elevation, weathering thickness, weathering velocity, or reference to a datum. The objective is to determine the reflection arrival times which would have been observed if all measurements had been made on a flat plane with no weathering or low velocity material present. These corrections are based on uphole data, refraction first breaks, and/or event smoothing. Uphole-based statics involve the direct measurement of vertical travel times from a buried source. This is usually the best static correction method where feasible. First break based statics are the most common method of making field static correction, especially when using surface sources. Data smoothing statistics methods assume the patterns of irregularity that most events have in common results from near surface variations and hence static correction trace shifts should be as to minimize such irregularities. Most automatic statics-determination programs employ statistical methods to achieve minimization. Underlying the concept of static corrections is the assumption that a simple time shift of an entire seismic trace will yield the seismic record which would had been observed if the geophones had been displaced vertically downward to the reference datum - an assumption not strictly true.”

This main issue of seismic standard processing will be explained more in detail (*Section 2.4*). Unfortunately most of these classical methods assume non-complex structures of the near surface, nearly flat stratigraphy with no or only gentle dips. To still achieve a reliable static correction of seismic traces a good approximation of the near surface, a near surface model, is of particular significance. The application of some specialized techniques may solve this problem and give information about necessary parameters as layer velocity and layer thickness as well as about the geometry of the model. In general the approach of the inverse theory and its applications is a most powerful instrument in solving complex seismic problems and some of them will be discussed in this thesis.

1.2 Objectives

The purpose of this diploma thesis is creating a near surface velocity model that is used as basis for static correction of a 3D data set. The data set was recorded during a seismic survey program in the years 2001/2002 which includes the 3D Waschbergzone1 seismic survey situated in the Weinviertel/Lower Austria. The goal of this survey was to resolve a more precise stratigraphic and tectonic image of this area (Spitzer, R., 2001).

For that reason the Vienna University of Technology received a 3D data set to analyze and create a subsurface model for static correction with methods, developed and partly specified for lithosphere research of the CELEBRATION 2000 (Guterch, et al., 2003) and ALP 2002 project (Brückl, et al., 2003).

1.3 Modelling strategy

The need of more sophisticated methods for static correction is required to estimate complex near surface structures. Especially in cases where the **three principles for sedimentary rocks** (principle of superposition, principle of horizontality and principle of lateral continuity), postulated in *Nicolaus Stenonis' Dissertationis prodromus (1669)*, are violated, static correction needs more than simple 1D velocity models of the underground. Thus the purpose of this thesis is to present some techniques of lithosphere research to sketch the bedding of the subsurface of a typical exploration area. Further it will be determined, if these seismological methods are also applicable for essentially smaller investigation areas with denser sampled data sets than for the seismological investigation areas. One of these routines is a robust 1D inversion based on ray tracing (e.g. Behm et al., 2007); those travel times are estimated from offset bin stacks. Another methodological different inverse routine represented in this thesis, is a tomographic travel time inversion procedure introduced by Hole, J. A., 1992, which can be used for densely sampled velocity models with large velocity contrasts. *Section 5.1* is focussed on the application of an iterative 1D inversion sequence of stacked travel times, while *section 5.2* describes the utilization of the tomographic travel time inversion method to enhance a velocity model of the subsurface.

2 3D seismic survey Waschbergzone 1

Section 2 gives a brief overview of the geographical position of the survey area as well as of the area, where the subsurface model is located (*Section 2.1*). *Section 2.2* illustrates some geological characteristics of the geological unit, the so called Waschbergzone (WBZ), which was investigated during seismic 3D Waschbergzone1 survey. While the acquisition parameters of this survey are explained in *section 2.3*, the fundamental principles of static correction, for that precise subsurface modelling is needed, are explained in *section 2.4*.

2.1 Geographical location of the survey area

The 3D Waschbergzone reflection survey was accomplished near the Czech border, approximately circumscribed by Staatsz, Drasenhofen, Schratzenberg and Erdberg (Figure 1).

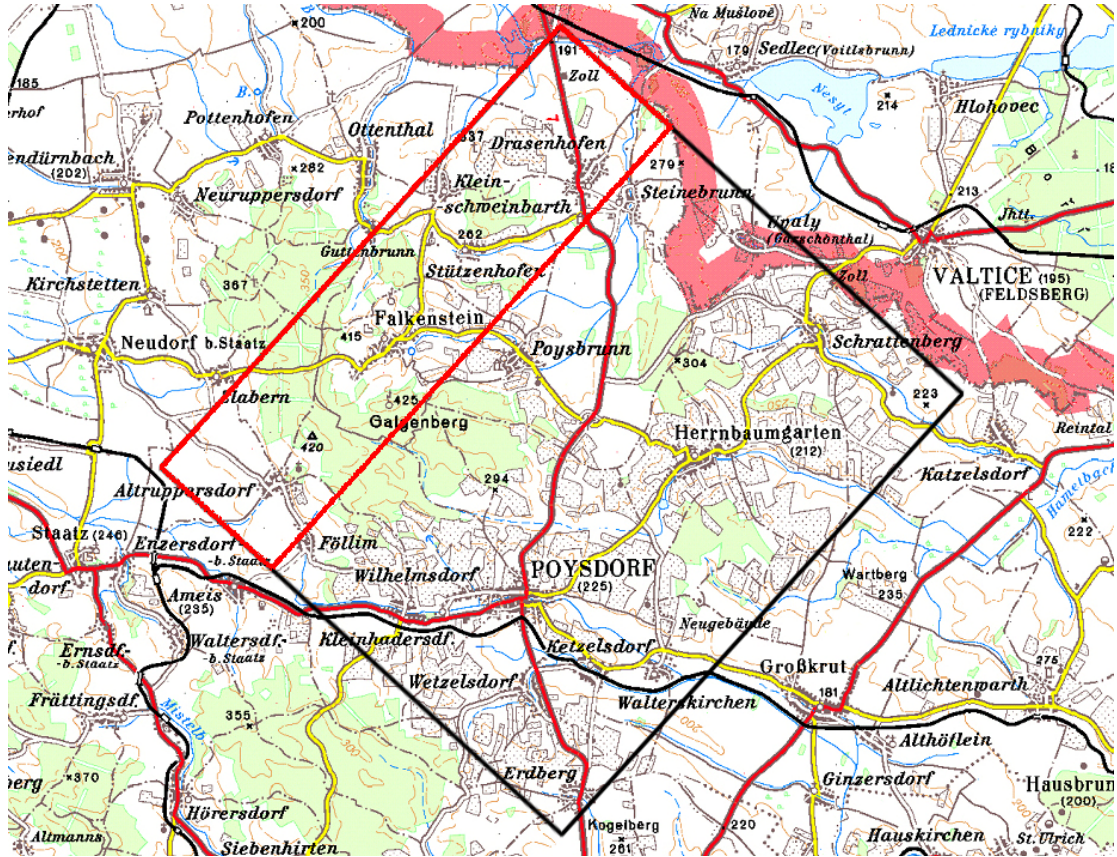


Figure 1: Geographically position of the Waschbergzone 3D survey area (black frame) and of the model area *Streifen1* (red frame).

2.2 Geology of the survey area

The study area is part of the external thrust rim of the Alpine system and can be separated in four tectonic units. The Steinberg fault isolates the pull-apart basin of the **Vienna basin area** from the Mistelbacher Scholle. The **Mistelbacher Scholle** consists of steeply dipping wedges of the frontier Flysch thrusts with thin piggy back basins of neogen sediments. The more or less undisturbed outer **Molasse** foreland establishes the tectonic north-west border of the Weinviertel and was deposited as terrestrial or shallow marine sediments during the rising period of the Alps. The tectonic unit of interest, the **Waschbergzone**, lies in between the Mistelbacher Scholle and the Molasse and consists of gentle to medium dipping wedges with incompetent layers of Mesozoic and tertiary sediments (Figure 2). The Waschbergzone extends from its eponym Waschberg (388 [m]) to Staatsz and Falkenstein and ends in the Czech Republic (“Zdanicka unit” in Czech).

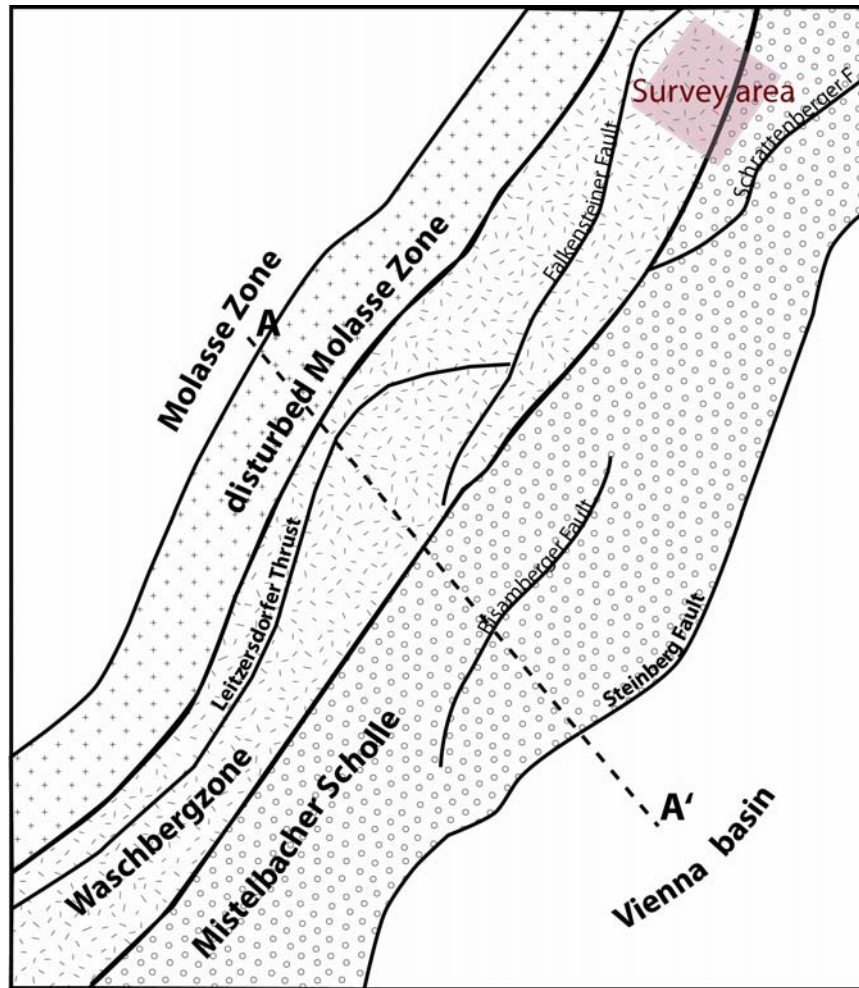


Figure 2: Tectonically map of Weinviertel/Lower Austria. The survey area is bordered by the Falkenstein fault and Schratzenberg fault and covers the Waschbergzone and the Mistelbacher Scholle.

An illustration of a representative vertical cross section is shown in *Figure 3*.

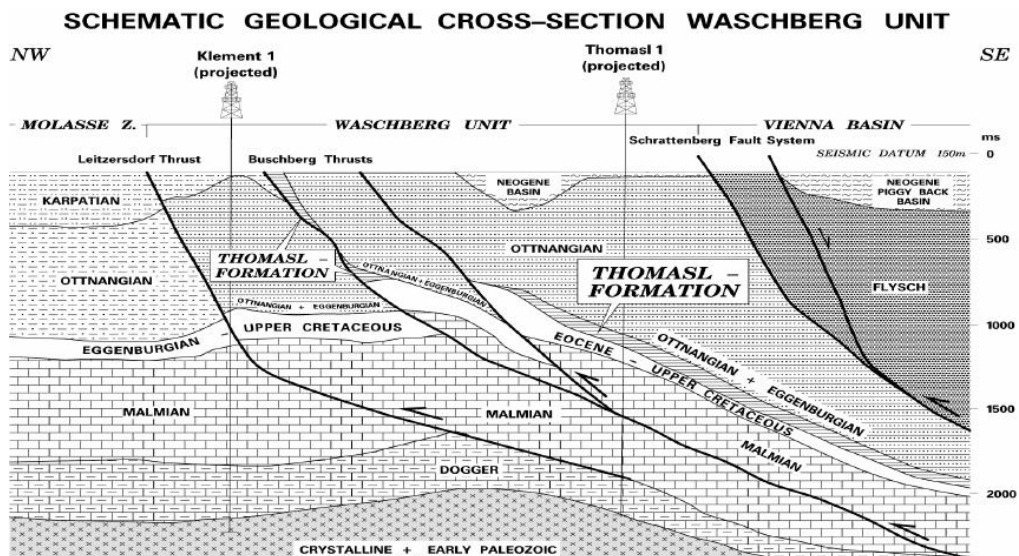


Figure 3 (from Herndler, E., 2001): Geological cross section through the Waschberg unit/Lower Austria.

The main material of the Waschbergzone rocks consists of layers of Eggenburgiens and Ottnangiens (*Brix, F., 1993*). This sequence of layers was created by turbidity currents (*Figure 4*), which are flows of sediment laden water down slope, because it is denser than surrounding water due to suspended clays. Such currents are often triggered by earthquakes and this will cause sediments to liquefy and move down a slope till the angle of slope dies out, so the current slows and loses competence and capacity and thus sediment settles out as turbidites in a characteristic sequence, defined as Bouma sequence (*Figure 5*).

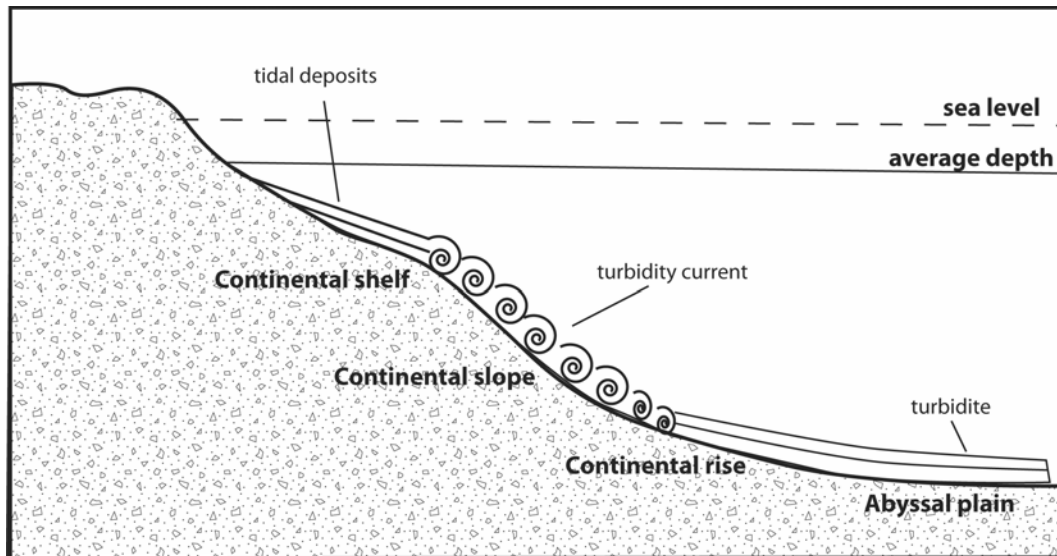


Figure 4: Development of turbidity currents, which settle out as graded beds, called Bouma sequences. Generally turbidity currents transport coastal sediments to submarine facies and form sedimentary submarine fans.

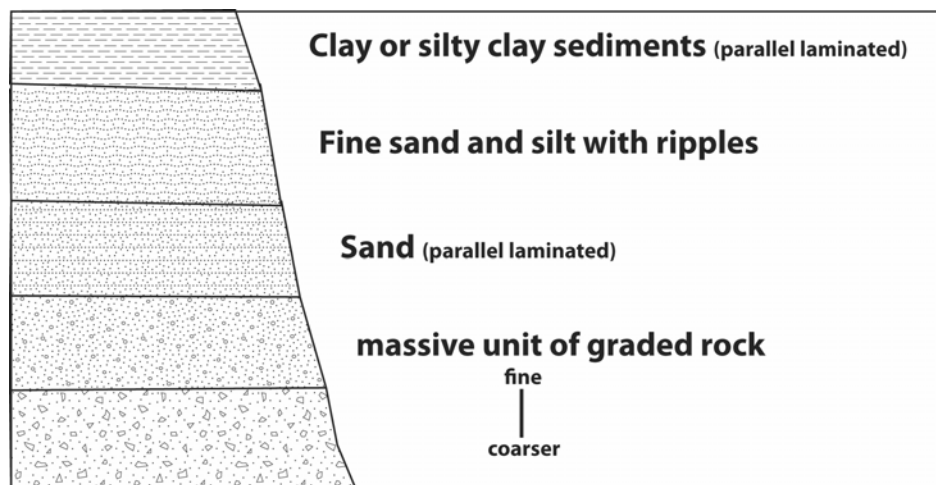


Figure 5: Bouma sequence. Overall it is a fining upwards sequence, those top and/or bottom parts are often missing due to various deposition and erosion processes.

These shallow sediments (also called “Auspitzer Mergel and Steinitzer Sandstein”) got lowered in deeper regions, were deposited in the late Miocene and covered rocks of the autochthon Mesozoic. In the investigated survey area these rocks (e.g. Ernstbrunner limestone) outcrop as Staatzer and Falkensteiner Klippen due to their density and hardness while surrounding sediments were eroded. At the end of the later Miocene the entire set of sedimentary layers and rocks was caught in the last phase of the alpine Carpathian movement and thrust over the Molasse. During this mechanism the Flysch zone was thrust over the Waschbergzone and so the present geological structure, a Neogene piggy back basin (Figure 6), was obtained (Brix, F., 1993).

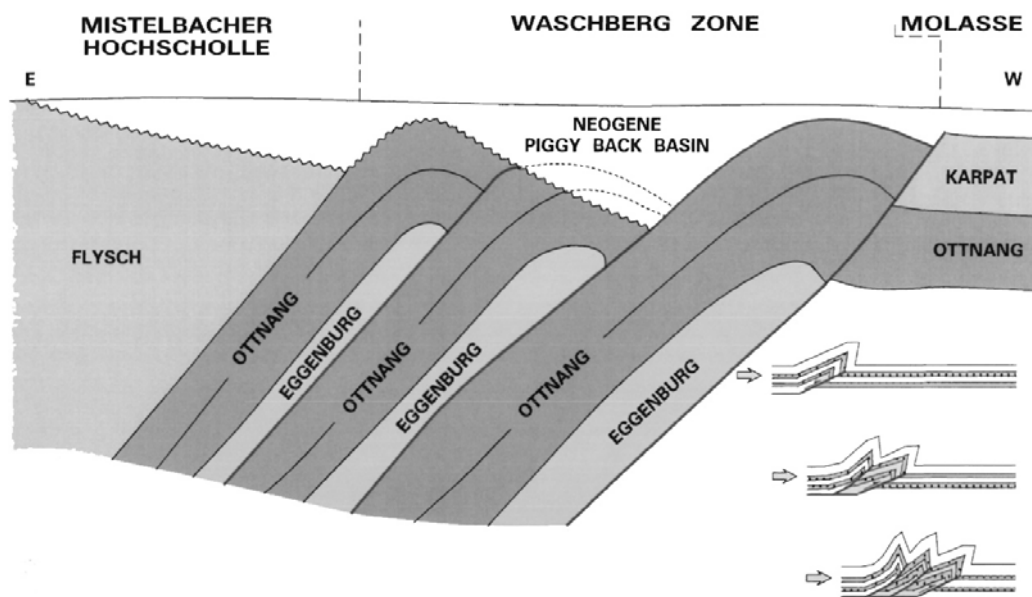


Figure 6 (from OMV GPH report 3D Waschberg, 2001): The Waschbergzone as an imbricate and thrust generated tectonically structure. Older thrust sheets (nappes) are carried piggyback by younger nappes due ramp fault propagation.

2.3 Data acquisition

The survey area consists of a hilly topography in the northwest, flattens south-eastwards and is covered by 20% fields, 20% forests, 60% vineyards, small villages and the small town Poysdorf. While the layout of receivers could be accomplished nearly straight, the sources were offset (e.g. due to agricultural reasons in vineyards).

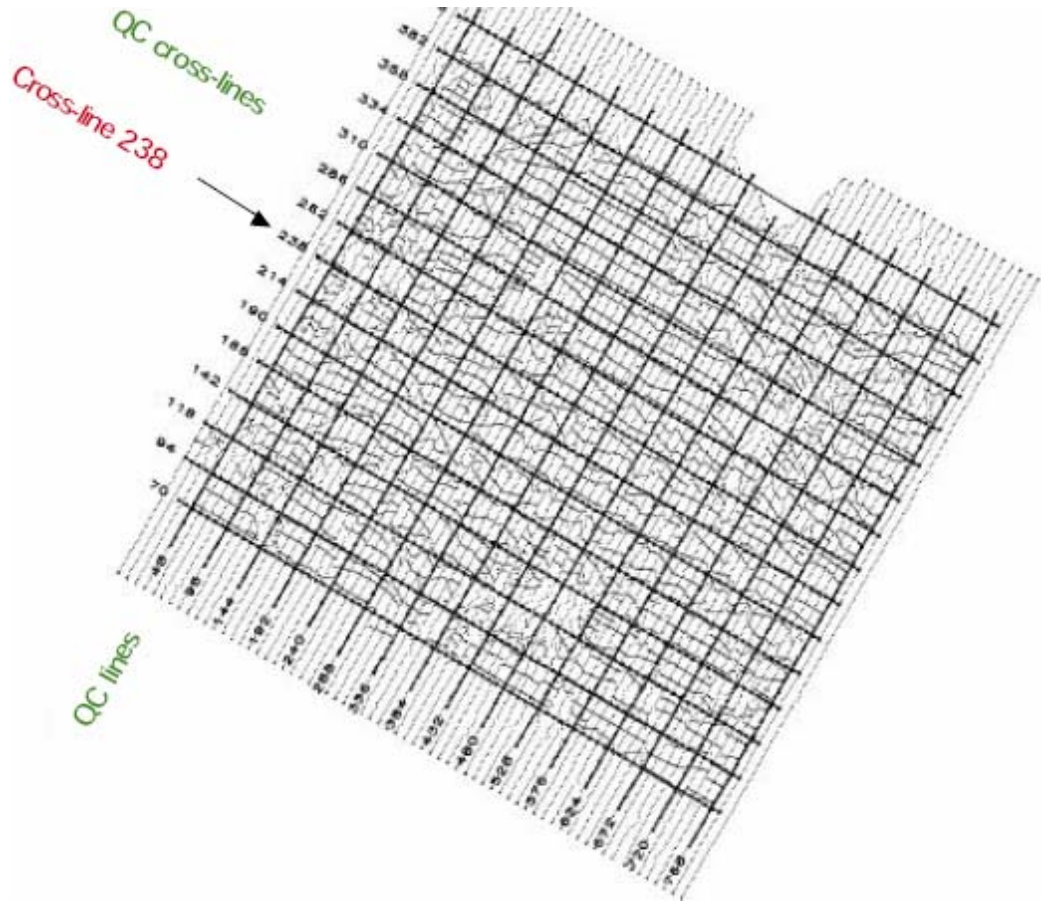


Figure 7 (from OMV GPH report 3D Waschberg, 2000): Positions of receivers (inline) and sources (cross-line). The bold coordinate points represent quality control (QC) lines.

The total number of receivers and sources was 14065 and 11461, respectively. The receivers have been laid out as 12 receiver groups with 60 channels. 97% of the sources were Vibroseis-generated and cut across the receiver lines. Since previous investigations for this area showed that frequencies over 80[Hz] are not advantageous, the frequency band amounts to 10-80[Hz]. The design considerations have been made about the bin size should secure that the bin size should be smaller than a third of the smallest target diameter and smaller than a quarter of the apparent wave length. These and further acquisition parameters are summarized in *Table 1*.

| | |
|--------------------------|-----------------|
| Bin size subsurface | 30x15[m] |
| Receiver group distance | 60[m] |
| Source distance | 30[m] |
| Fold | 36 |
| Receiver line distance | 180[m] |
| Source line distance | 300[m] |
| Spread | 12x60 |
| Source points per spread | 36 |
| Channels per record | 720 |
| Sample rate | 2[ms] |
| Record length | 4[s] |
| Vibroseis source | 4vibs |
| Sweep frequency | 10-80[Hz] |
| Sweep length | 12[s] |
| Vertical stack | 5 |
| Pattern | 60[m] |
| Move on | 4x3[m], 1x18[m] |

Table 1: Summary of the most important acquisition parameters (developed and distributed by DMT)

2.4 *Static correction*

The reason for the application of static correction is minimizing local topographic and near surface effects due to inhomogeneous weathering layers (*e.g. Cox, M., 1999*). Such a replacement surface is called datum and lies below the real acquisition surface. If it is not chosen to be flat for any reason, it is known as floating datum. Relative to the datum, the seismic data have a more regular structure, free of elevation effects. Otherwise problems during seismic standard processing will arise; especially the velocity analysis and the stacking sequence are affected by deviations of the hyperbolic trends. Virtually all current velocity analysis procedures are based on the idea of the hyperbolic moveout, which itself is predicated on the idea of a horizontally layered subsurface. Even if this is true, complications arise in land data by virtue of the fact that the top layer, the surface, is not flat. Hence one of the important objectives of static correction is to reinstate something approaching hyperbolic moveout relative to the datum. Errors in doing this will manifest themselves as non hyperbolic residuals with consequently effects on velocity analysis and, ultimately, the stack. To see how static correction is applied, a simple near surface model is shown in *Figure 8*.

There are two surface locations A and B for whose vertical projections on the datum A_d , B_d and the associated static corrections t_a , t_b are defined.

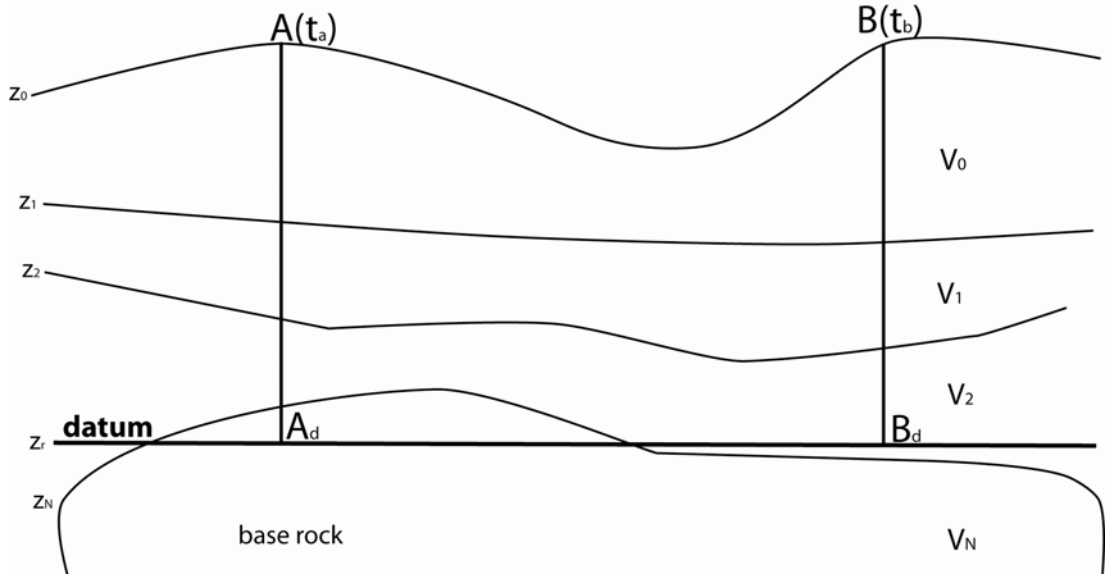


Figure 8: Schematically description of components of datum static correction. The static time shift t_a for point A represents the static correction for all layers above the datum and the second term in equation (1) is positive, since $Z_r > Z_n$. The second term for t_b , on the other hand, is negative, as $Z_r < Z_n$ and it can be assumed as filling up of the area beyond the datum with V_N . The second term vanishes in the special case $Z_r = Z_n$.

In general, computation of datum static correction t_{static} therefore requires source and receiver elevations Z_0 , the thickness $Z_{i+1} - Z_i$ and velocities of the weathering layers V_i . Furthermore the elevation of the chosen datum Z_r and the velocity from the base of the weathering layer to the reference datum V_N is needed. The following relations based on a simple example of $N - 1$ weathering layers highlights the computing of datum static correcting with parameters mentioned above. The required time shifts for static correction will be calculated as follows:

$$t_{static} = \sum_{i=0}^{N-1} \frac{Z_{i+1} - Z_i}{V_i} + \frac{Z_r - Z_N}{V_N} \quad (1)$$

If there is more than one weathering layer, the first term will be the sum of static corrections of $N - 1$ weathering layers, while the second term represents the correction value between datum and the base of the last weathering layer. It is obvious that the reliability of the datum static correction strictly depends on the accuracy of the parameters constituting the equations above and so it will be recommended to create a near surface velocity model for calculating datum based travel times.

Datum static correction implies an assumption of vertical rays in the near-surface layers. In most survey areas, ray path differences with respect to vertical rays through near surface layers are small and can be neglected. This basic assumption of classical datum static correction is not true in areas, where the weathered layers are thick, significant lateral near-surface velocity changes occur, the reflectors are not deep or have large dips and the velocity ratio between the substratum and the near-surface is small. An alternative to conventional datum static corrections is **wave equation**

datuming or **re-datuming**. This method allows upward or downward continuation of the seismic data, is consistent to wave theory and thus static shifts derived from this method are closest to reality. One wave equation datuming algorithm was formulated by *Berryhill, J., 1979* and differs from conventional datuming methods in the repositioning of seismic reflections laterally as well as vertically in response to observed time dips. This method is based on the Kirchhoff integral and continues seismic data from the surface down to an intermediate datum and then up to the final datum (*Figure 9*). Even though wave equation datuming is the best method for the removal of the overburden above the target horizon, in any case it requires significant computer time, why in many standard processing sequences the classical approach of datum correction is used.

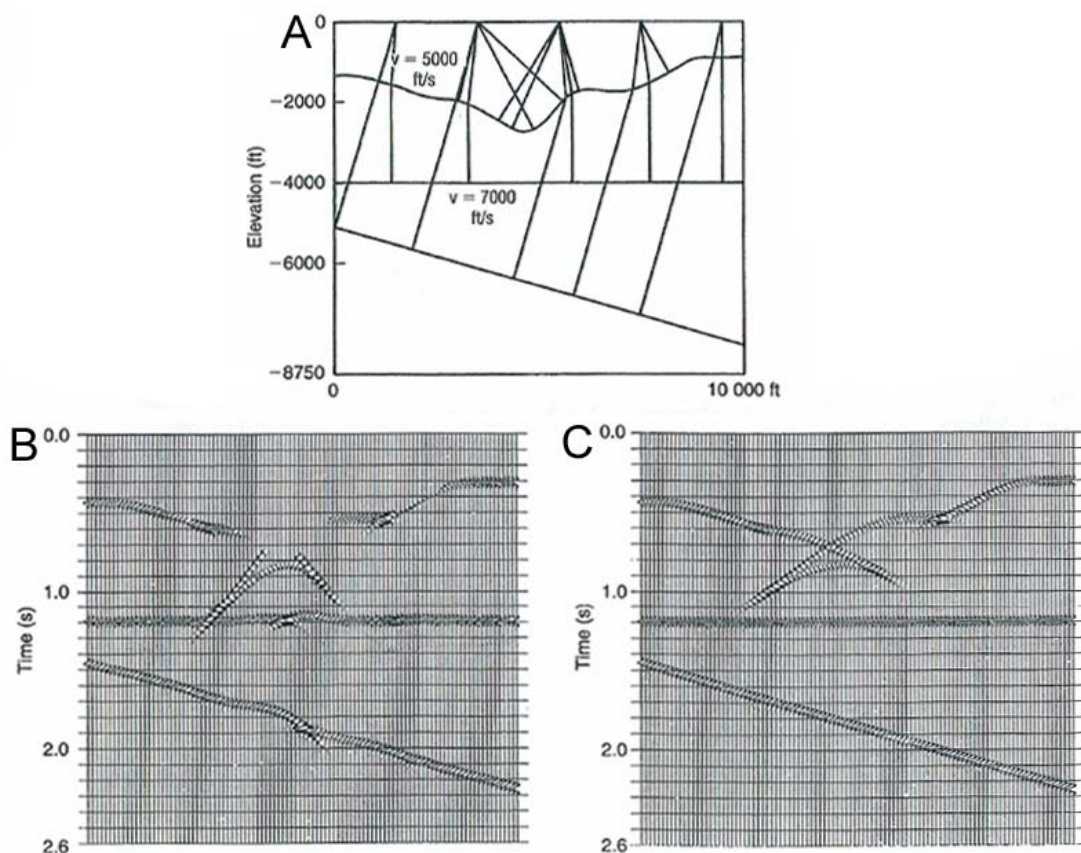


Figure 9 (from Berryhill, J., 1979): (A) Synthetic seismic structure with an irregular substratum and a dipped reflector. (B) Conventional static correction was applied to data and (C) wave equation datuming was applied. It is obvious that after the approach of re-datuming the reflectors became linear and all distortions associated with the overburden vanished.

There is a wide range of classical seismic techniques, like uphole surveys, refraction and ray methods to achieve satisfying results for static corrections.

3 Pre-processing of a selected data set

Certain pre-processing steps have already been accomplished in the department *OMV Exploration & Production GmbH* and will be specified in *section 3.1*. Finally the entire data set was portioned in 10 SEG Y files and put at the disposal for further processing. The next step was to import data into one of the main processing units of this project, the ProMAX 2D software (Version 2003.0; Landmark Graphic Corporation 1989-2001), which is an interactive seismic processing system (*Section 3.2*).

3.1 Pre-processing by OMV

In this section some of the issues involved in practical pre-processing of seismic data will be described and are schematically illustrated by *Figure 10*.

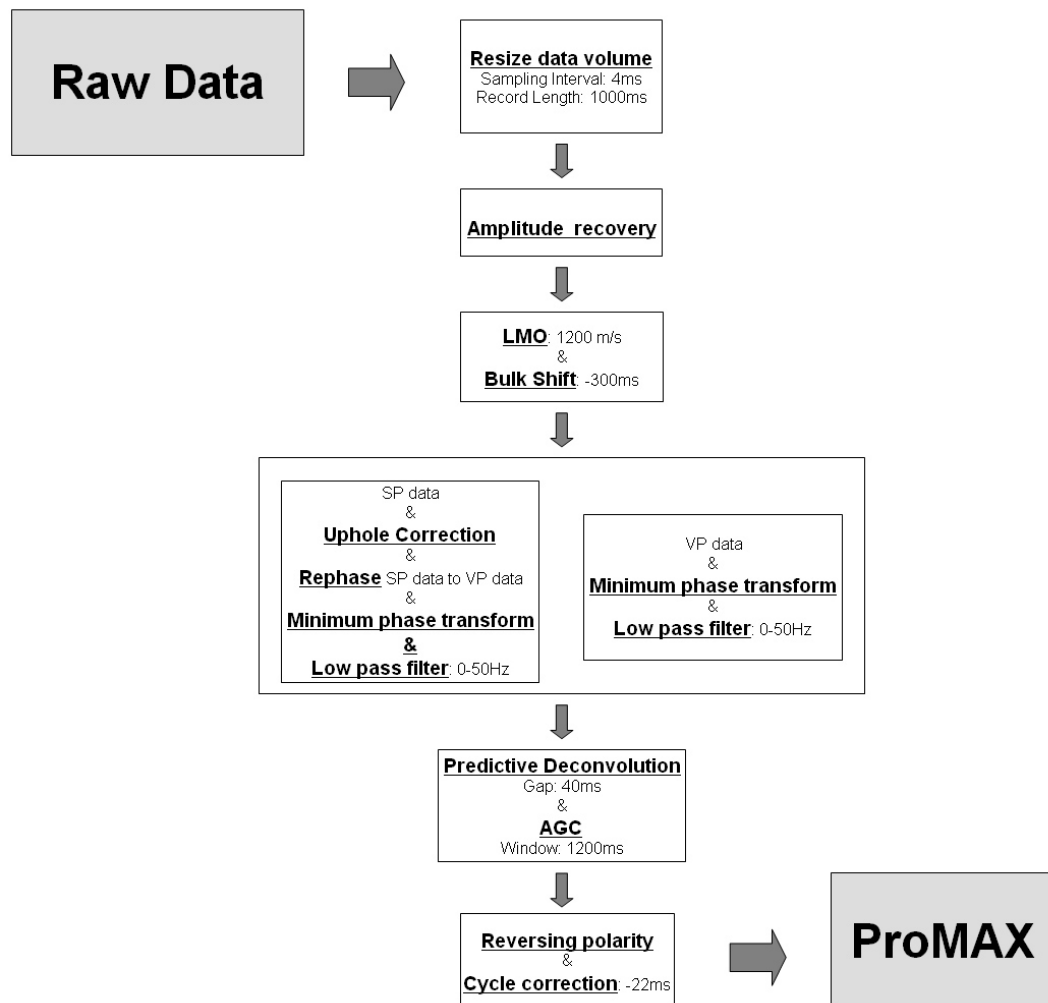


Figure 10: Illustration of basic steps of pre-processing performed by OMV processing.

The size of the entire data set, which was subdivided into ten sections and saved as swath1-10.sgy files, was downsized by re-sampling data (sample interval: 4[ms]) and by cutting off the total record length.

Since seismic traces show in their raw state a decrease in amplitude with time, a correction of geometric spreading effects have to be applied early in processing to avoid this amplitude decay. Loss mechanisms are divergence (geometrical spreading according to the inverse square law), absorption by inelastic propagation, scattering from small heterogeneities and transmission losses (*e.g. Hatton, L., 1986*). As not every contribution (*e.g. noise, some diffraction anomalies*) varies like other contributions of a seismic trace, equalization methods have to be applied.

The Linear Moveout correction (LMO) either removes or applies a static shift based on following formula:

$$T = d / v \quad (2)$$

where T [ms] is the static shift, d is the offset between the recorded trace and the source point and v is the average velocity from the source and the receiver. So each trace of the processing data set will be shifted by the length of the offset d divided by the specified LMO correction velocity $v(d)$ (2500[m/s]). Thereby offset dependence of the seismic traces will be reduced and the reliability of first breaks picks will be increased. Additionally a bulk shift (-300[ms]) was applied to prevent any information losses.

The seismic survey used Vibroseis and dynamite as sources and thus the recorded traces are also different due to the particular signature of the seismic input signal. To use both data sets for deconvolution, the data sets with different source signatures have to be equalized and transformed to minimum phase. As the number of shot points (SP) is essentially smaller than the number of Vibroseis points (VP), traces with an explosive input signal have been converted to Vibroseis generated traces with minimum phase. Additionally an up-hole correction is required to compensate for the burial of the shot (4[ms]).

Vibroseis is an extremely useful method for environmental reasons and consists of a controllable sweep signal in form of a frequency modulated sinusoid (*e.g. up-sweep and down-sweep*). The distribution of input energy over time is in sharp contrast to explosive sources in which the source is generated in a small fraction of a second. In Vibroseis processing, the **Vibroseis correlation** is an important tool to transform the sweep signal to a short time duration signal. Further the obtained signal has to be transformed to minimum phase, so that deconvolution now is applicable.

Predictive deconvolution is filtering of predict future values attempted from a time series from past and present values. The input x is a time series recorded up to a present time index t with $[..., x_{t-2}, x_{t-1}, x_t]$, then the desired output at the time $t + q$ can be written as

$$d_t = x_{t+q} \quad (3)$$

where q is the prediction distance or lag. It is obvious from equation (3) that predictive deconvolution is identical to spiking deconvolution in the case of using the sample rate as lag or it can predict wavelets at a future time. For this purpose a prediction filter can be created and applied on the input time series to obtain the desired time advanced output. The success of this operation depends on how predictable the time series is. In general multiples are highly predictable, whereas the reflection series, with which they are convolved, is normally highly unpredictable (*Hatton, L., 1986*). While the **prediction filter** yields the multiples of a seismic trace, the remaining error series (reflection series) can be determined by a constructing prediction error filter. Based on the general form of the matrix equation for a filter of length n , the generalized form of an n -long prediction filter and a α -long prediction lag can be written as:

$$\begin{bmatrix} r_0 & r_1 & r_2 & \dots & r_{n-1} \\ r_1 & r_0 & r_1 & \dots & r_{n-2} \\ r_2 & r_1 & r_0 & \dots & r_{n-3} \\ \cdot & \cdot & \cdot & \dots & \cdot \\ \cdot & \cdot & \cdot & \dots & \cdot \\ r_{n-1} & r_{n-2} & r_{n-3} & \dots & r_0 \end{bmatrix} \cdot \begin{bmatrix} f_0 \\ f_1 \\ f_2 \\ \cdot \\ \cdot \\ f_{n-1} \end{bmatrix} = \begin{bmatrix} g_\alpha \\ g_{\alpha+1} \\ g_{\alpha+2} \\ \cdot \\ \cdot \\ g_{\alpha+n-1} \end{bmatrix} \quad (4)$$

where r_i are the autocorrelations of the input wavelet, f_i are the desired predictive filter coefficients and g_i are the crosscorrelations of the desired output with the input wavelet. The **prediction error filter** a_i is obtained from the prediction filter f_i , which is the solution to equation (4). For $\alpha = 1$, which is identical to the special case spiking deconvolution, the filter coefficients for a_i are

$$a_i = (1, -f_0, -f_1, \dots, -f_{n-1}) \quad (5)$$

The length n of a prediction (error) filter is ideally determined by using the autocorrelation of the input wavelet, which has the squared amplitude spectra of the unknown wavelet (*Aki, K., Richards, P., 2002*). Increasing the prediction lag α leads to suppressing higher frequencies and preserves the overall spectral shape of the input data (for the processed data set, a prediction lag $\alpha = 40$ [ms] was used. In spite of the band limiting character of predictive deconvolution a low pass filter (0 – 50 [HZ]) was applied to the data set before deconvolution).

In the end automatic gain control ($AGC = 1200$ [ms]) was applied and polarity of traces was reversed.

3.2 Preparation of data

This section illustrates a critical step in processing to prepare data for static correction, the estimation of seismic travel times. This highly subjective processing step affects the solution of classical refraction static correction as well as the investigated tomography modelling methods. On the one hand side the first breaks of original, single traces were picked (*Section 3.2.1*) and on the other side the first breaks of stacked traces were picked (*Section 3.2.2*) to create two data sets serving as input for the travel time inversions in *Section 5.2* and *Section 5.1*, respectively.

3.2.1 Geometry specification and picking of travel times from single fold traces

The seismic field tape was recorded as SEG Y format which is used by various workstations including Sierra, Landmark, Charisma, MS-DOS, Prakla and Western and documented in detail in a SEG monograph entitled *Digital tape standards*. This section provides a brief overview about three essential flows to pick seismic travel times, the import and assigning of geometrical information to the seismic data (*Section 3.2.1.1*), as well as the picking of the seismic travel times (*Section 3.2.1.2*). At the end of this section, geometrical and travel time information was extracted to an external data base and the allocation of the data set to an orthogonal coordinate system was accomplished, which is essentially for further processing steps (*Section 3.2.1.3*).

3.2.1.1 Specification of geometry

First of all one partition swath1, renamed as **Streifen1** was imported as SEG Y file by defining disk file path name and some standard parameters and written on the disk in compressed 16 bit format with real scalars. To extract pre-geometry information from recorded trace headers and to write them into the database, the tool **Extract Database Files** was executed (*Figure 11*).

```
Editing Flow: 01-input
Add      Delete      Execute      View      Exit
SEG-Y Input
>Trace Length<
Disk Data Output -> rohdaten
Disk Data Input <- rohdaten
Extract Database Files
>Automatic Gain Control<
>Linear Moveout Correction<
>Trace Display<
>Interactive Spectral Analysis<
```

Figure 11: Extracting internal data information to database

Processing data with any seismic processing system requires information of the field geometry recorded during the data acquisition process. Coordinates of source and receiver locations for all traces are stored on traces headers. Geometry assignment can be accomplished using a number of processes in subsequent processing flows (Figure 12).

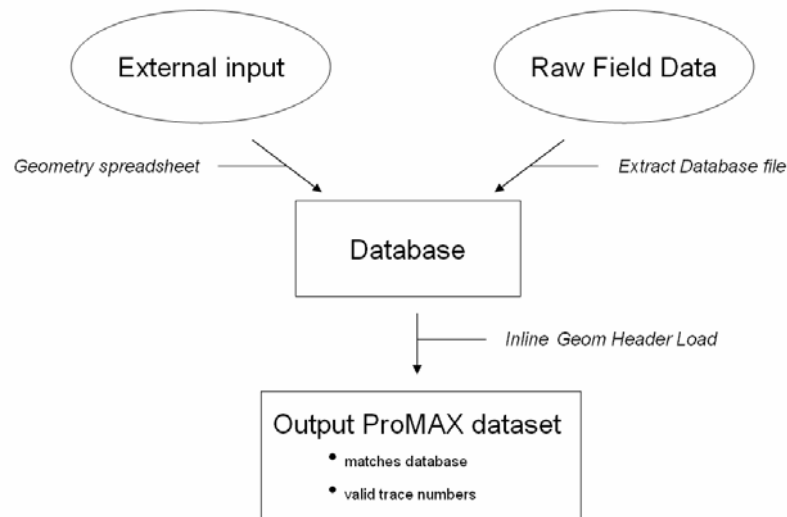


Figure 12: Specification of geometry

Information for the geometry description will be typically obtained from trace headers of the field tapes or from observer's notes, which can be imported and edited by hand with the **2D Land Geometry Spreadsheet editor**. This editor serves as the basic interface to the database and is a correction tool for changes in receiver and source locations.

```

Editing Flow: 02-geometrie
Add      Delete      Execute      View      Exit
2D Land Geometry Spreadsheet*
>Disk Data Input<
>Inline Geom Header Load<
>Disk Data Output<
  
```

Figure 13: Assigning of geometrical information from observer's notes to data base.

To complete the geometry assignment, a standard set of information was rewritten from the database to the trace headers of the dataset which will be used for further processing. This step is accomplished by including **Inline Geom Header Load** within the processing flow.

3.2.1.2 Picking of travel times from single fold traces

Picking of travel times from single fold traces serves as input for the travel time tomography (Section 5.2). Since signal quality depends on the source type and the conditions of the near surface, the detection of the onset of signal is not trivial. Especially Vibroseis sources yield a low signal to noise ratio for first breaks in comparison to explosive sources and therefore picking is much more difficult. Effectiveness of both reflection and refraction-based methods of static correction depends on the reliability of the picking process (Yilmaz, Ö., 2001). To display and pick a certain number of traces the flow 03-display has been executed (Figure 14).

| Editing Flow: 03-display | | | | |
|---|---------------|----------------|-------------|-------------|
| Add | Delete | Execute | View | Exit |
| Disk Data Input <- geometrie_gedreht | | | | |
| >Interactive Spectral Analysis< | | | | |
| >Header Statics< | | | | |
| >Linear Moveout Correction< | | | | |
| >First Break Picking< | | | | |
| >CDP/Ensemble Stack< | | | | |
| >Linear Moveout Correction< | | | | |
| >Linear Moveout Correction< | | | | |
| Trace Display | | | | |

Figure 14: Processing flow 03-display. First break picking and/or application of optional tools.

There are several methods to estimate first-break picks, in particular automatic, interactive and manual methods, or combinations of thereof. For the picking process a combination of an interactive Neural Network FB Picker and manually picking was performed (Figure 15). Insufficiently estimated first picks by neural network tool (due to a low signal to noise ratio) have been corrected or killed. This subjective influence on travel time estimation will be discussed later.

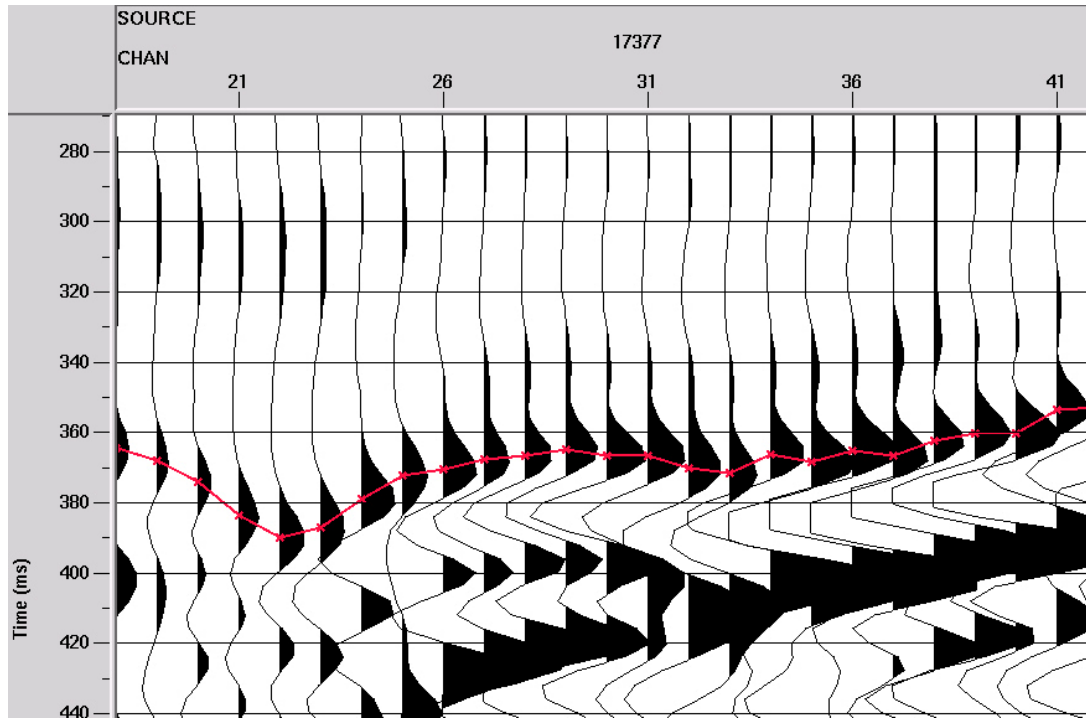


Figure 15: Demonstration of travel time picking on amplitude maximum.

3.2.1.3 Export of travel times and geometric information

It is a pre-condition that LMO correction, as well as the bulk shift, will be reduced from traces before creating data sets to export. Two data sets with all in all ten parameters will be created and exported as ASCII files (*Table 2*).

| | |
|-------------|--|
| SIN | Source Index Number |
| Sou_X | X coordinate of the source |
| Sou_Y | Y coordinate of the source |
| Sou_Elev | Z coordinate (elevation) of the source |
| SRF_loc | Receiver Index Number |
| Rec_X | X coordinate of the geophone |
| Rec_Y | Y coordinate of the geophone |
| Rec_elev | Z coordinate (elevation) of the geophone |
| FB_Mayerlin | First Breaks |
| Aoffset | Absolute Offset |

Table 2: Two ASCII files containing all in all ten significant parameters for further processing.

The two data sets were merged to one OASIS database and essentially modified in three steps. Geosoft's OASIS serves database and mapping tool for earth sciences. As the maxima of the first arrivals were picked, an additional bulk shift (-15ms) was applied and rows with no travel times have been eliminated. Further traces with negative travel times as a result of LMO correction and bulk shift also have been eliminated. To finalize the OASIS database, the coordinates of sources and receivers must have been rotated about an angle ϕ and shifted to an origin (0, 0) of an

imaginary orthogonal coordinate system. For original coordinates X_o and Y_o this will be accomplished by

$$\begin{pmatrix} X \\ Y \end{pmatrix} = \begin{pmatrix} X_o - \overline{XO}_{\min} \\ Y_o - \overline{YO}_{\min} \end{pmatrix} \quad (6)$$

and

$$\begin{pmatrix} X_n \\ Y_n \end{pmatrix} = \begin{pmatrix} \cos \phi & -\sin \phi \\ \sin \phi & \cos \phi \end{pmatrix} \cdot \begin{pmatrix} X \\ Y \end{pmatrix} \quad (7)$$

where \overline{XO}_{\min} and \overline{YO}_{\min} are the minimum distances. The modified source and receiver locations, as well as the entire dataset can be used for further processing steps, especially for 3D travel-time tomography by *Hole, J. A., (1992)*, which requires the assumption of an orthogonal geometry (*Figure 16*).

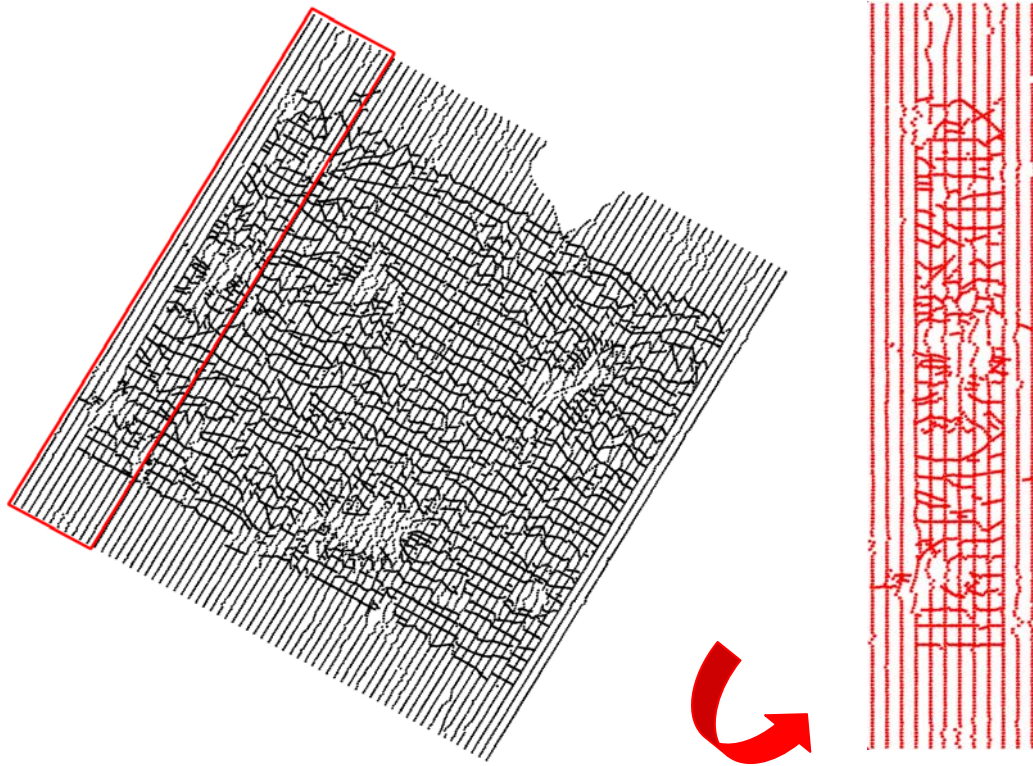


Figure 16: The right sketch shows the entire layout of the 3D Waschbergzone1 seismic survey (black symbols). The selected area (red labelling) is identical to the partition *swath 1*, which will be processed in future applications. Since some inverse applications require a data set parallel to an orthogonal coordinate system, the source and receiver locations of *swath 1* will be rotated. The left sketch shows the rotated receiver locations (inline) and source locations (cross line) by red symbols.

3.2.2 Application of stacking and picking of travel times from stacked traces

This section deals with the estimation of travel times from stacked traces used for a seismic tomography based on 1D inversion. The substantial thought of this robust 1D

inversion is sorting traces by CMP and assigning them to cells on a regular grid raster (*Section 3.2.2.1*). The outcome of this is a data set of sorted traces which can be stacked by their common offset. Finally the first arrivals of the resulting stacked traces are evaluated (*Section 3.2.2.2*) and serve as data input for *Section 5.1*.

3.2.2.1 Sorting data by CMP

Common midpoint (CMP) sorting underlies the assumption that the reflection points lay half way between source and receiver location. This assumption is correct for flat layered structures, but for more realistic structures the reflection points no longer lie in the midpoint plane (*Figure 17*).

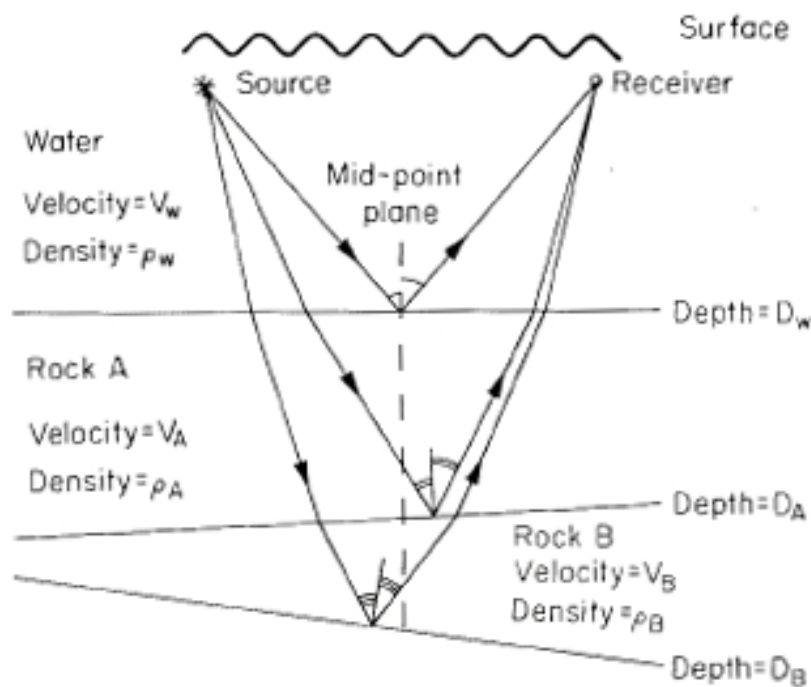


Figure 17 (from Hatton, L., 1986): CMP assumption for a non flat layered structure. Simple geometric consideration shows that the assumption is not valid for strong dipping layers.

At least in areas where dips are slight and the stratigraphy is not complicated, this assumption serves as usable approximation and allows stacking of traces. CMP sorting is also applicable for refraction as well as diving waves and provides the best resolution for the 1D case as it reduces the influence of dipping interfaces. This common tool in seismic data processing improves data quality as well as the signal to noise ratio. For this purpose a regular spaced grid will be defined by its corners and the grid spacing, which is equivalent to the initial width of the cells, whose midpoints are assigned to a particular grid point (*Figure 18*).

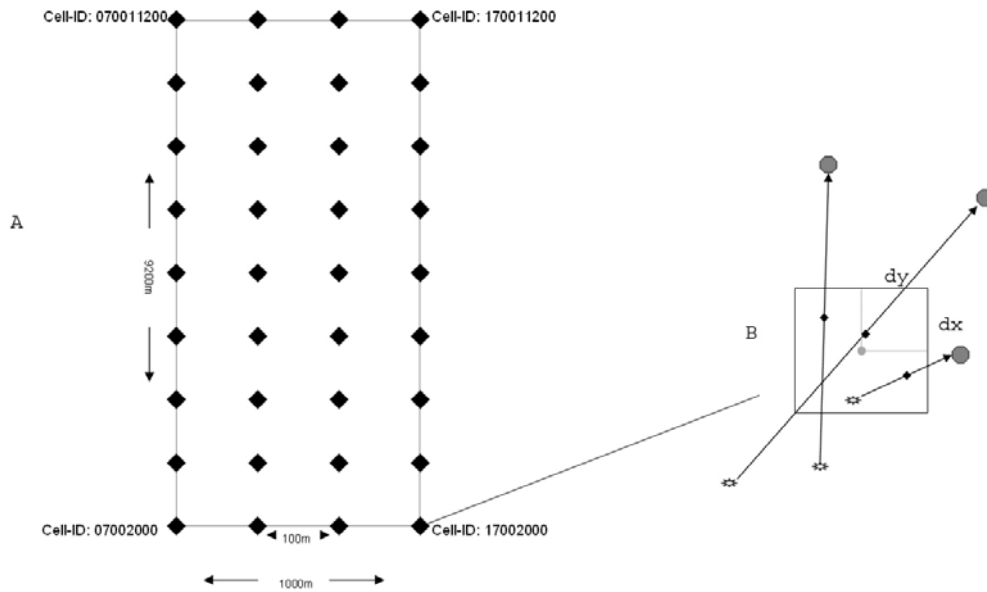


Figure 18: Part A: Grid raster, where the black diamonds symbolize the cell centres with associated cell ID, which is obtained from grid coordinates. Part B: Scheme of a usually quadratic cell (light grey midpoint), which is spanned up by variable half width dx and dy . Seismic sources and receivers are represented by suns and grey octagons, while their CMP's are represented by black diamonds.

These cells do not need to be standard sized, as they can vary from $100\text{ [m]} \times 100\text{ [m]}$ to $200\text{ [m]} \times 200\text{ [m]}$. This is controlled by a defined minimum condition, which secures a certain number of common midpoints within a cell. Additionally a certain number of CMP sorted traces with short offsets can be defined, which are required to resolve the top layers of a near surface structure. For this, minimum 50 traces with an offset from $0\text{--}300\text{ [m]}$ were chosen, otherwise the half width of the cells increase with an increment of $20\text{ [m]} \times 20\text{ [m]}$.

To compensate undesired effects due to the irregular distribution of the common midpoints, the definition of the CMP is extended to small areas. These usually rectangular areas are called bins, in which items of similar nature are grouped (e.g. CMP's). Choosing the bin size should provide an advantageous trade-off between a sufficiently large amount of suitable traces and the spatial resolution. So a standard bin size of $30\text{ [m]} \times 30\text{ [m]}$ was chosen and thus traces within a bin were assigned to a particular common offset bin.

The parameters above are summarized as sorting conditions, which control the sorting process of any imported data set. For computational reasons, the data set prepared in *Section 3.2.1.1* was divided into two parts and was used together with a digital terrain model (DTM) derived from regular gridded receiver elevations, as data input (*Figure 19*).

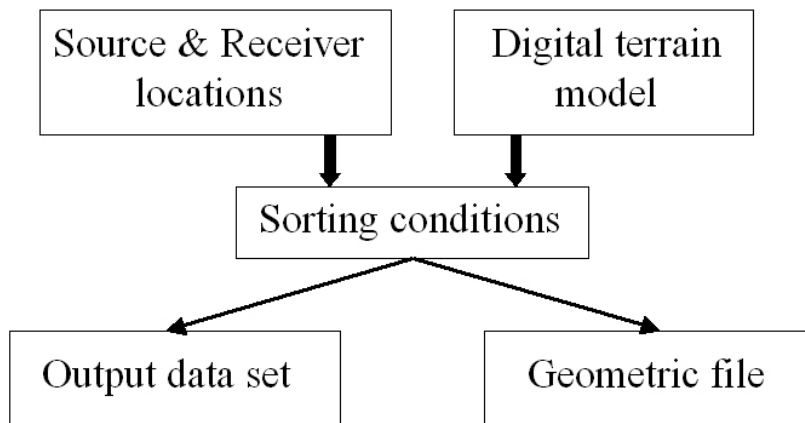


Figure 19: Scheme of a common midpoint sorting sequence.

This sorting process yields either an output file containing CMP sorted traces, which will be stacked in *Section 3.2.2.2*, or a file with geometric information used later for inverting a stacked data set (*Section 5.1.1*).

3.2.2.2 Stacking and picking data

After all seismic traces were sorted by their common midpoint, traces with the same offset bin were superimposed, which is in seismic terms known as stacking. Beside those advantageous attributes as improving data quality, stacking is also a process of data volume compression. This section provides an overview onto the computationally realization of stacking and the estimation of the first arrivals assigned to this new data set (*Figure 20*).

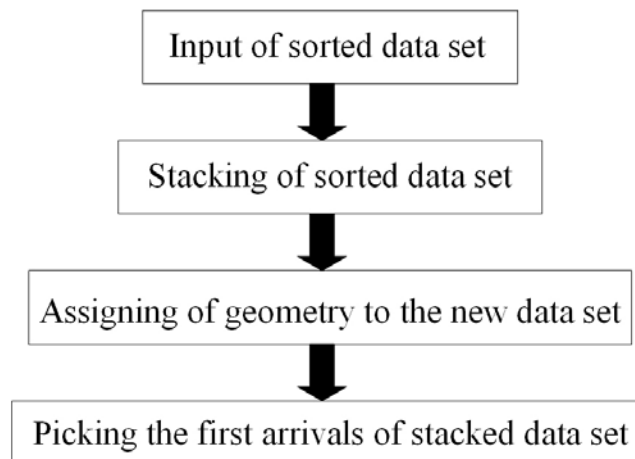


Figure 20: Overview of the stacking and picking process to estimate first break times for 1D ray tracing and inversion.

The imported SEGY files were collected in a database and the tool reflection strength was applied. Reflection strength computes the amplitude of the analytical signal that corresponds to the envelope of the seismic trace (*e.g. Hatton, L., 1986*). This should

prevent, that the output trace after stacking is not affected by different input traces with probably shifted maxima or minima and for that reason all amplitudes will be positive. Before stacking, any applied LMO correction will be removed and substituted by a LMO correction with a reduction velocity near to the limestone velocity (e.g. 4000[m/s]) and after stacking this process will be reversed. Since some bins are empty due to missing traces, the absent output traces will be substituted by auxiliary traces with no seismic signal. Specification of geometry is very similar to those for single traces (*Section 3.2.1.1*), but with an additional binning option, which defines the binning grid, the bin centre and the fold for ProMAX database. Applying these mentioned tools leads to a visualization of stacked traces within one cell. The required travel times can be estimated by picking the first arrival times. For this purpose two assumptions were made:

- Velocity inversions (low velocity zones) in the offset bin stack will be not picked.
- 1D inversion can only resolve spatial flat structures and no short wavelength variations.

With these assumptions only clear first breaks were picked, which will be visualized by the following examples:

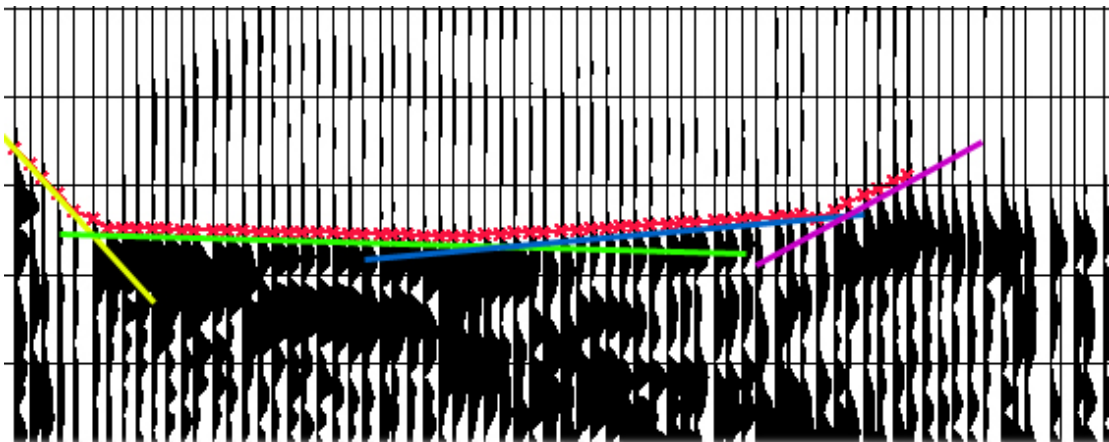


Figure 21: Offset bin stack of cell 7002200 indicates a four layer case. The first layer is a weathering layer with a very low seismic velocity (yellow labelling), which is followed by two sediment layers (green and blue labelling) with velocities between 2500-3000[m/s]. The violet labelling is associated with a high velocity medium that can be considered as the Waschberg limestone in deeper regions for this grid point.

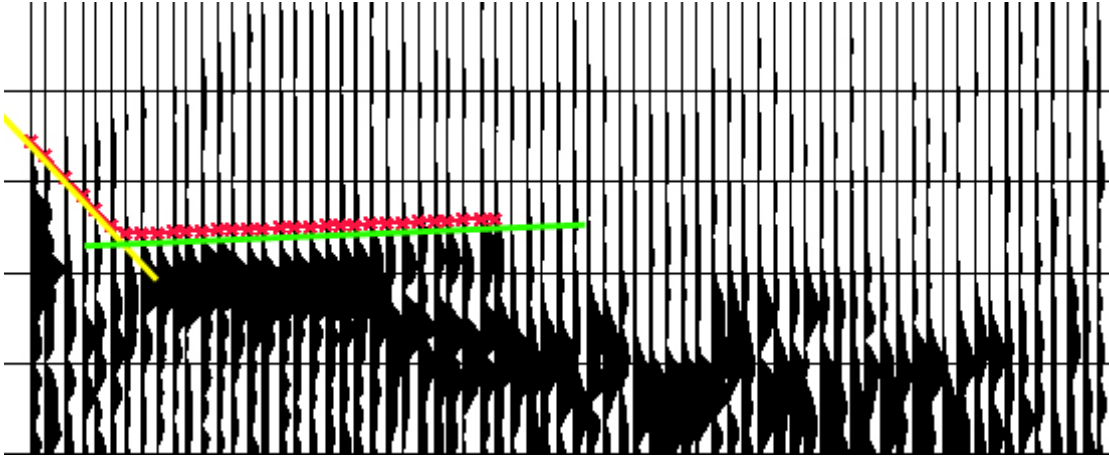


Figure 22: Offset bin stack of cell 90009300 indicates a two layer case. Only the first two layers are estimated by first break picking, while other layers are indeterminably due the complex geological structure.

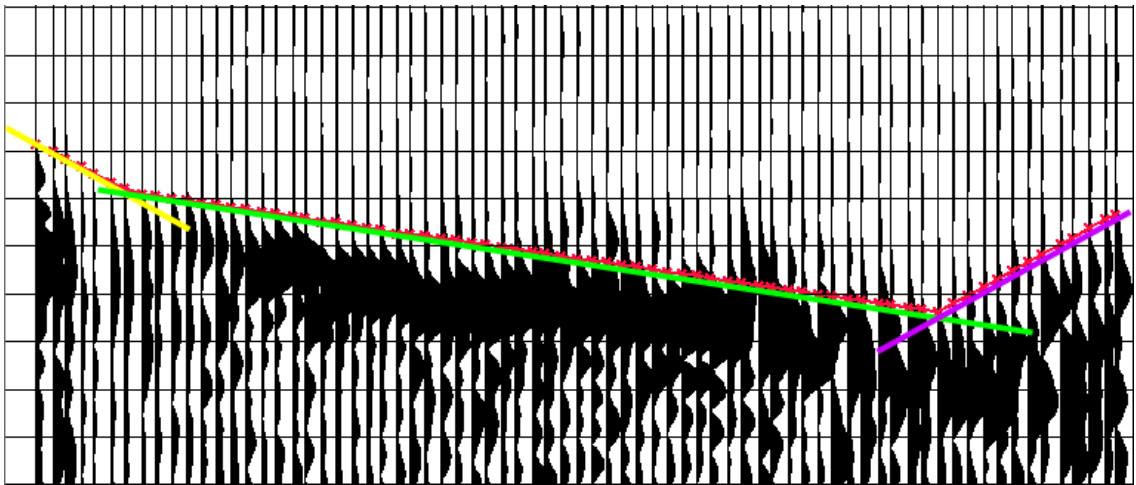


Figure 23: Offset bin stack of cell 70006000 indicates a three layer case with a detected weathering layer (yellow labelling), a low velocity sediment layer (green labelling) and a high velocity layer associated with Waschberg limestone (violet labelling)

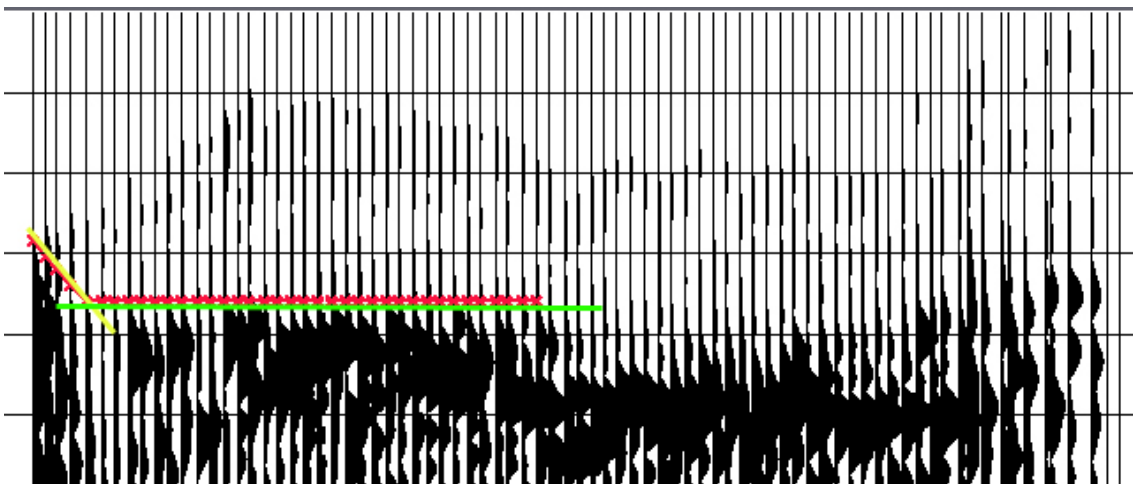


Figure 24: Offset bin stack of cell 70006500 indicates a two layer case. Based on the made assumptions, only the weathering layer (yellow labelling) and one sediment layer are detected and thus the high velocity layer on the right side is not determineable.

4 Travel time modelling and principles of inversion techniques

Inversion simply means that a parameter (e.g. seismic velocity) can be determined directly from observed data (e.g. travel times) (*Hatton, L., 1986*). There are many inverse methods underlying this principle adaptive to a wide range of geophysical problems. Inversion is strongly interrelated with the forward problem, which describes an iterative way of solving inverse problems. For this calculated model parameters will be compared to observed parameters, such that the error between them will be minimized. The following sections deal with inverse theory and its application on a 3D data set (*Section 4.2*), after a brief introduction about the fundamentals of continuum mechanics and the basic relations of ray theory (*Section 4.1*).

4.1 Fundamentals of elastic waves and ray theory

Elasticity theory usually describes the physical behaviour of elastic solids and fluids. In our case the behaviour of particular particles creating in sum the elastic earth, under influence of seismic waves is the aim of investigation. *Section 4.1.3* gives an overview of the equation of motion which describes the propagation of seismic waves as function of time and space. Next to some fundamentals of continuum mechanics (*Section 4.1.1*), the Eikonal equation and its relevance for ray tracing, one of the underlying principles of inverse methods, will be briefly discussed (*Section 4.1.5*). The following description follows works by *Aki, K., Richards, P., 2002, Moczo, P., 2004, Hatton, L., 1986* and *Nolet, G., 1987*.

4.1.1 Basic definitions and relations

The motion of particles of earth can be described in terms of displacement as a function of space and time, written as $u_i = u_i(x_i, t)$. A relative descriptive illustration of the deformation term can be made by comparing to infinitesimal neighbouring particles at the position $P(x_i)$ and $Q(x_i + dx_i)$ (*Figure 25*). To examine the deformation of a medium, it is necessary to analyze the new positions at $P'(x_i + u_i)$ and $Q'(x_i + dx_i + u_i + du_i)$ of those particles after some displacement. It can be testified that the gradient of displacement $u_{i,j}$ is directly related to any change of relative position du_i as following

$$du_j = u_{i,j} dx_i \quad (8)$$

with using the index notation

introduced by defining nine quantities, so that τ_{ij} is the i -th component of force acting on a plane perpendicular to the x_j -axis (*Figure 26*). The quantities of the stress tensor τ_{ij} are therefore sufficient to describe the stresses acting on the coordinate planes through a point.

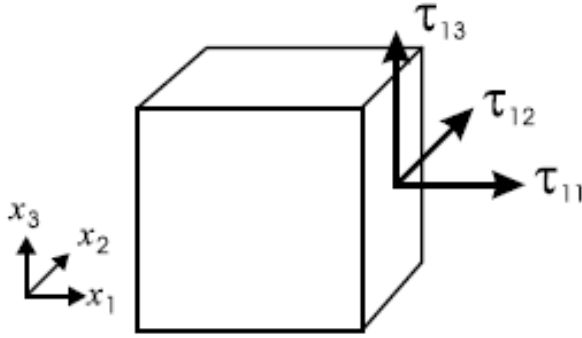


Figure 26: The stress tensor and its components. In this example τ_{11} is the normal component and τ_{12} , τ_{13} are the tangential components of the stress tensor acting along the x_1 -axis.

Traction T_i is a vector, being the force acting per unit area across an internal surface within the continuum, and quantifies the force with which the particles on the one side of a surface act upon particles on the other side (*Aki, K., Richards, P., 2002*). The maximum of force acts in direction of the unit normal n_i perpendicular to the surface and the resulting traction is denoted as $T_i(n_i)$. The component parallel to n_i is called normal strain (pressure) and the component perpendicular to n_i is called tangential strain (shear strain).

If the traction components are known within a body for each unit normal vector n_i , it is possible to define the stress tensor τ_{ij} and vice versa.

$$T_i = \tau_{ij}n_j \quad (13)$$

Volume forces and surface forces are in equilibrium state for an arbitrary volume, if

$$\int (\rho u_{i,t} - f_i) dV - \int (T_i) dF = 0 \quad (14)$$

where u_i is the component of the displacement of a particular particle due to the influence of stress τ_{ij} and the body force component f_i . With these definitions and relations mentioned above, one of the most crucial relations of the theory of seismic waves, the equation of motion can be derived (*Section 4.1.3*).

Via a simple consideration of the equilibrium of torques within an arbitrary volume, the number of independent components can be reduced to six, which means that the stress tensor is symmetric.

$$\tau_{ij} = \tau_{ji} \quad (15)$$

4.1.3 Equation of motion

The equation of motion for a particular particle can be formulated in a small, continuous and elastic continuum as follows:

$$\rho u_{i,tt} = \tau_{ij,j} + \bar{f}_i \quad (16)$$

The mechanical behaviour is directly related with Hooke's law, which describes the linear relation between stress and strain. It named Cauchy's generalized formulation for the elastic continuum and reads as

$$\tau_{ii} = C_{ijkl} e_{kl} \quad (17)$$

C_{ijkl} is the 4th-order tensor of elastic coefficients and has 81 components, which can be reduced to 21 independent coefficients due to symmetry and the law of thermodynamics. In a simple, isotropic continuum, material parameters depend only on position and there remain only two independent elastic coefficients λ and μ , the Lamé constants and can be proven that

$$C_{ijkl} = \lambda \delta_{ij} \delta_{kl} + \mu (\delta_{ik} \delta_{jl} + \delta_{il} \delta_{jk}) \quad (18)$$

and inserting (18) into (17) gives

$$\tau_{ij} = \lambda \delta_{ij} e_{kk} + 2\mu e_{ij} \quad (19)$$

which is the Hooke's law for the isotropic continuum. Strain e_{ij} is a local measure of the relative change of a particular particle in position and displacement field due to deformation and is also described in terms of displacement. Inserting (11) into (19) yields

$$\tau_{ij} = \lambda \delta_{ij} u_{k,k} + \mu (u_{i,j} + u_{j,i}) \quad (20)$$

Equations (16) and (20) are called the displacement stress formulation of the equation of motion for the perfectly elastic, unbounded isotropic heterogeneous continuum and inserting (20) in (16) leads to the displacement formulation of the equation of motion.

$$\rho u_{i,tt} = (\lambda u_{k,k})_{,i} + (\mu u_{i,j})_{,j} + (\mu u_{j,i})_{,j} + \bar{f}_i \quad (21)$$

If the Lamé coefficients and the density are spatial constants, equation (21) can be rewritten as

$$\rho u_{i,tt} = (\lambda + \mu) u_{k,ki} + \mu u_{i,jj} + \bar{f}_i \quad (22)$$

There are many methods developed to solve the equation of motion. The entirety of these methods can be separated in two groups. The analytic (exact) methods are generally applicable in the case of a homogeneous medium or simple heterogeneous, e.g. horizontally layered model with a smooth velocity gradient. The numerically (approximate) methods can roughly be divided in high frequency and low frequency methods. The ray method, which will be used later, belongs to high frequency based methods (*Section 5.1* and *Section 5.2*).

4.1.4 Separation of the equation of motion

Neglecting the body force term of equation (22) and applying Helmholtz decomposition lead to wave equations of longitudinal and shear waves. The Helmholtz decomposition to the displacement vector u_i is defined as

$$u_i = \phi_{,i} + \varepsilon_{ilk} \psi_{k,l} \quad (23)$$

where ϕ and ψ are scalar and vector potentials. Inserting Helmholtz decomposition (23) into (22) gives us:

$$\rho \phi_{,tti} + \rho \varepsilon_{ilk} \psi_{k,ttl} = (\lambda + \mu)(\phi_{,jji} + \varepsilon_{jlk} \psi_{k,lji}) + \lambda \phi_{,ijj} + \lambda \varepsilon_{ilk} \psi_{k,ljj} \quad (24)$$

$$(\rho \phi_{,tt} - (\lambda + 2\mu)\phi_{,jji})_{,i} + \varepsilon_{ilk}(\rho \psi_{k,tt} - \mu \psi_{k,jj})_{,l} = 0 \quad (25)$$

Equation (25) is obviously satisfied, if

$$\rho \phi_{,tt} - (\lambda + 2\mu)\phi_{,jji} = 0 \quad (26)$$

and

$$\rho \psi_{k,tt} - \mu \psi_{k,jj} = 0 \quad (27)$$

The following definition of the speed of the primary wave α

$$\alpha = \sqrt{\frac{\lambda + 2\mu}{\rho}} \quad (28)$$

and of the secondary wave β

$$\beta = \sqrt{\frac{\mu}{\rho}} \quad (29)$$

leads to **wave equations in terms of the potential:**

$$\phi_{,tt} = \alpha^2 \phi_{,jji} \quad (30)$$

$$\psi_{k,tt} = \beta^2 \psi_{k,ij} \quad (31)$$

So the equation of motion for an unbounded isotropic medium can be separated in two wave equations, where P-waves propagate accompanied with changes in volume and S-waves propagate accompanied with changes in shape. Equations (30) and (31) form the point of origin for the derivation of the Eikonal equation.

4.1.5 The Eikonal equation

The desired harmonically solution for the P-wave potential ϕ of differential equation (31) consists of the amplitude decay A in respect of the distance x_i and the phase function θ as general time delay:

$$\phi = A(x_i) e^{i\omega[t-\theta(x_i)]} \quad (32)$$

Inserting the spatial derivative

$$\phi_{,ij} = \left[A_{,ij} - A\omega^2 |\theta_{,ij}|^2 - i(2\omega A_{,j}\theta_{,j} + A\omega\theta_{,ij}) \right] e^{i\omega[t-\theta(x_i)]} \quad (33)$$

and the time derivative

$$\phi_{,tt} = -A\omega^2 \cdot e^{i\omega[t-\theta(x_i)]} \quad (34)$$

into wave equation (30) by dividing factor $e^{i\omega[t-\theta(x_i)]}$ gives

$$A_{,ij} - \omega^2 A |\theta_{,ij}|^2 - i[2\omega A_{,j}\theta_{,j} + \omega A_{,ij}\theta] = -\frac{A\omega^2}{\alpha^2} \quad (35)$$

Decomposing equation (35) into the real part (36) and the imaginary part yields for the real part:

$$A_{,ij} - \omega^2 A |\theta_{,ij}|^2 = -\frac{A\omega^2}{\alpha^2} \quad (36)$$

Dividing by $A\omega^2$ leads for compressional waves to

$$|\theta_{,ij}|^2 - \frac{1}{\alpha^2} = \frac{A_{,ij}}{A\omega^2} \quad (37)$$

and analogous for shear waves to

$$|\theta_{,ij}|^2 - \frac{1}{\beta^2} = \frac{A_{,ij}}{A\omega^2} \quad (38)$$

Assuming high frequencies, the wave field in a smoothly varying heterogeneous, isotropic and perfectly elastic medium separates into two wave types. So the wave field consists of compression waves (P waves) and shear waves (S waves). Increasing the frequency $\omega \rightarrow \infty$, the terms on the right hand side of equations (37) and (38) vanish, thus both equations only differ in velocity (α or β). We consider only one of them and denote the velocity of propagation by v ,

$$|\theta_{,j}|^2 = \frac{1}{v^2} \quad (39)$$

where v is either α or β . Equation (39) is called **Eikonal equation** or equation of the travel time field. The Eikonal equation is a good approximation of the wave equation at the high frequency limit and thus only valid for short wavelengths. In other words, the approximation is valid if the fractional change in the velocity gradient is much less than the wave frequency (*Officer, C. B., 1958*). In inhomogeneous regions with strong velocity gradients, P and S waves are coupled, at least for lower frequencies. Such situations cannot be investigated by the standard ray method (*Cerveny, V., 1987*).

4.1.6 The ray tracing system and Fermat's principle for seismic rays

The basic equation of computing rays and travel times is the Eikonal equation, which is as the mathematical formulation of Huygens's principle, which states that each point of an advancing wave is regarded as source of secondary waves. Vice versa the sum of all secondary waves can be considered as one wave, or in other terms, as propagating wavefront. Introducing the slowness vector p_i , which is perpendicular to the wavefront ($\theta = const$).

$$p_i = \theta_{,i} = \frac{1}{v} n_i = \frac{1}{v} \frac{dx_i}{ds} \quad (40)$$

where n_i is the unit vector perpendicular to the wavefront or the tangent along the ray with an arc length ds .

Seismic rays can be described as characteristics of equation (39). This nonlinear partial differential equation can be solved by a system of ordinary differential equations, the so called **ray tracing system**. Using the travel time τ along the ray measured from some reference point instead of the phase function θ yields

$$\frac{dx_i}{d\tau} = v^2 p_i \quad (41)$$

$$\frac{dp_i}{d\tau} = -\frac{1}{v} \frac{\partial v}{\partial x_i} \quad (42)$$

If arc length ds is considered instead of the ray travel time τ , so $ds = v d\tau$, the system of first order differential equations (41) and (42) will be transformed to a first order system:

$$\frac{dx_i}{ds} = vp_i \quad (43)$$

$$\frac{dp_i}{ds} = -\frac{1}{v^2} \frac{\partial v}{\partial x_i} \quad (44)$$

Choosing initial values for $p_i(\tau = 0)$ and $p_i(s = 0)$ or $x_i(\tau = 0)$ and $x_i(s = 0)$, the ray tracing systems can be solved and the components of the slowness vector, $p_i(\tau)$ and $p_i(s)$, or the coordinates of any point along the ray, $x_i(\tau)$ and $x_i(s)$, can be computed. Rays are extremes of Fermat's function and can be described by the following relation:

$$\tau = \int_A^B \frac{1}{v} ds \quad (45)$$

Fermat's principle states that the ray path geometry is such that it renders the travel time stationary and it can also be proven that travel times are unaffected for small ray path perturbations. The evidence of Fermat's principle for seismic rays can be supplied by showing the validity of the Eikonal equations in the case of small slowness perturbations (Nolet, G., 1987).

The travel time dt for small ray path segments dx_i is with $(dx_i dx_i)^{1/2} = n_i dx_i$

$$\frac{n_i dx_i}{v} = dt \quad (46)$$

and if the ray is perturbed, the modified travel time $dt + \delta dt$ will be:

$$dt + \delta dt = \frac{n_i(dx_i + \delta dx_i)}{v + \delta v} = n_i(dx_i + \delta dx_i) \cdot \left[\frac{1}{v} + \delta \left(\frac{1}{v} \right) \right] \quad (47)$$

The travel time perturbation δdt of a small ray segment can be explicitly formulated in first approximation as

$$\delta dt = \frac{1}{v} n_i \delta dx_i + \delta \left(\frac{1}{v} \right) n_i dx_i \quad (48)$$

where n_i is the unit vector of the unperturbed ray. The relation (48) for a travel time perturbation in a sufficient small ray path segment can be extended to the entire ray path by integrating from two fixed points A to B:

$$\delta\tau = \int_A^B \frac{1}{v} n_i \delta dx_i + \int_A^B \delta \left(\frac{1}{v} \right) n_i dx_i = \int_A^B \frac{1}{v} n_i \frac{\delta dx_i(s)}{ds} ds + \int_A^B \delta \left(\frac{1}{v} \right) n_i \frac{dx_i(s)}{ds} ds \quad (49)$$

The first integral can be integrated by parts and with $n_i = dx_i / ds$ and $\delta(1/v) = \delta dx_i (1/v)_{,i}$ equation (49) can be rewritten as

$$\delta\tau = \frac{1}{v} n_i \delta dx_i(s) \Big|_A^B - \int_A^B n_i \frac{d}{ds} \left(\frac{1}{v} \right) \delta dx_i(s) ds + \int_A^B \delta dx_i(s) \left(\frac{1}{v} \right)_{,i} n_i ds \quad (50)$$

and due to the fact that δdx_i has to be zero at the fixed end points of the ray path, the formulation of the total travel perturbation is:

$$\delta\tau = \int_A^B \delta x_i \left[- \frac{d}{ds} \left(\frac{n_i}{v} \right) + \left(\frac{1}{v} \right)_{,i} \right] ds \quad (51)$$

By definition of Fermat's principle, the travel time is stationary and thus $\delta\tau = 0$. This will be valid for equation (51), if for an arbitrary ray path, the integral kernel will be zero and it follows that

$$\frac{d}{ds} \left(\frac{n_i}{v} \right) = \left(\frac{1}{v} \right)_{,i} = \frac{dp_i}{ds} \quad (52)$$

which is identical with the second ray tracing equation (44). Therefore Fermat's principle is valid for seismic rays, which are described by the ray tracing system based on the Eikonal equation.

4.2 Inverse theory

The determination of three-dimensional seismic structures of a survey has been more and more important, since computers have been developed which are capable to process enormous data sets. The historically origin of 3D tomographic inversion methods was its application on teleseismic travel times to find a model of the global seismic structure by *Aki, et al., 1977*. Since this work many authors modified 3D inversion for specific applications that are substantially refraction and reflection seismology and the use of observed teleseismic or local earthquake data for modelling subsurface structures. The 3D inversion of local travel times is computationally much more complex than that of teleseismic ones (*Koch, M., 1992*). Although the 3D seismic problem requires linearity between the observed data values

and parameters of the medium, many geophysical inversion methods do not fulfil this condition because they are non-linear problems.

The simplest methods of deducing model parameters, which do not require assumptions concerning linearity, are “trial and error” methods, like the “Monte Carlo Inversion”. Earth scientists first used Monte Carlo Inversion techniques more than 30 years ago and since that time they have been applied to a wide range of problems, from the inversion of free oscillation data for whole Earth seismic structure to studies at the meter-scale lengths encountered in exploration seismology (*Sambridge, M., 2002*). A variant of this method, known as “Hedgehog Inversion” tests the nearest neighbours to a successfully determined parameter and if once an apparent realistic model is found, non random subroutines enhance model within the generated model space. The main advantage of these random methods comparing to more sophisticated inversion schemes is the independence from complexity of model constraints. With the advent of more powerful computers 3D inversion techniques became more and more state of the art.

For a general 3D subsurface model, the travel time τ for a ray is a function of the slowness $u = v^{-1}$ and the ray path geometry given by the integral equation (45). The problem is to estimate u from a number of time measurements at the surface, since it is implicitly present in the ray path $s[u]$. This is a non linear inverse problem and non linear equations are difficult to solve (*Nolet, G., 1987*). Analytic solutions are possible for simple, homogeneous media and if a sufficiently good coverage of ray paths is available. For more realistic problems which commonly arise on earth, we have to apply more general numerical methods. Inversion usually allows to explore the whole model space and to delimit a range of possible models, which fit to data within its experimental and observational error interval equally well (*Koch, M., 1992*).

The following subsections of this chapter will provide an insight into fundamentals of inverse problems (*Section 4.2.1*) as well as an overview of two selected particular inverse methods, namely the simultaneous iterative reconstruction technique SIRT (*Section 4.2.2*) a nonlinear 3D seismic travel time tomography (*Section 4.2.3*) and a seismic tomography based on 1D ray tracing and inversion (*Section 4.2.4*).

4.2.1 Fundamentals of inverse problems

The inverse problem is stated in seismology as

$$\tau = \int_{s[u(r_i)]} u(r_i) ds \quad (53)$$

and describes the relationship between observed travel times τ and the desired model parameter, the seismic slowness $u(r_i)$ as function of the position vector r_i .

Since the slowness is strongly intertwined with the ray path $s[u(r_i)]$, the integral equation becomes nonlinear. Either the seismic slowness values $u(r_i)$ will be determined by iterative trial and error forward modelling, otherwise relating geophysical observations to earth parameters needs to linearizing the nonlinear inverse problem (58), which can be achieved by considering small slowness perturbations compared to the predefined reference slowness $u_0(r_i)$. Hence equation (53) can be rewritten as:

$$\tau = \int_{s[u_0(r_i) + \delta u(r_i)]} u_0(r_i) ds + \int_{s[u_0(r_i) + \delta u(r_i)]} \delta u(r_i) ds \quad (54)$$

Using Fermat's principle (Section 4.1.6), travel times becomes unaffected by small ray path perturbations and the integral over the ray path $s[u_0(r_i) + \delta u(r_i)]$ can be replaced by the unperturbed ray path $s_0[u_0(r_i)]$ and thus the travel time perturbation can be formulated as:

$$\delta\tau = \tau - \tau_0 = \int_{s_0[u_0(r_i)]} \delta u(r_i) ds \quad (55)$$

For n travel time observations, one obtains a linear system of equations for m slowness perturbations $\delta u(r_i)$

$$y = Ax \quad (56)$$

where the known travel times $y = (\delta\tau_1, \delta\tau_2, \dots, \delta\tau_n)^T$ and the unknown slowness perturbations $x = (\delta u_1, \delta u_2, \dots, \delta u_m)^T$ are related by the model matrix A , which is a $n \times m$ matrix describing the kernel of the integral. The validity of this linearization depends on the nonlinearity of the model matrix A (e.g. Koch, M., 1985a), so for inverse problems with stronger nonlinearities, the final inverse solution for x can only be achieved by iterative updating. The inverse solution of equation (56) can be formally stated as

$$x = A^{-1}y \quad (57)$$

Tikhonov A. and Arsenin V. (1977) define three major issues in respect to **existence**, **uniqueness** and **stability** of the inverse solution. Any inverse problem which doesn't fulfil these issues is denoted as ill-posed inverse problem. For that purpose a variety of techniques to restore the well-posed solutions exist, they are known as regularization methods.

One of the methods for solving geophysical inverse problems is the **generalized matrix inversion (GMI)**. While the existence of the ordinary inverse of a square

matrix A^{-1} , or the inverse in least square methods $A_s^{-1} = (A^T A)^{-1} A^T$ is not so trivial, the generalized inverse (g-inverse) A^+ of a general $n \times m$ matrix A with $rank(A) = p$ exists, regardless of the existence of the nullspaces $N(A)$ and $N(A^T)$ (for more information about GMI and the aspects of the Hilbert space, see Koch, M., 1992 or Bjerhammar, A., 1973).

The $rank(A) = p$ determines the uniqueness of the solution, which is shown in the following cases:

The general least squares solution x_s can only be directly found by

$$x_s = A^+ y \quad (58)$$

with

$$A^+ = (A^T A)^{-1} A^T \quad (59)$$

if the system is fully determined $rank(A) = p = m = n$ or overdetermined $rank(A) = p = m < n$. In both cases the covariance matrix $(A^T A)$ stays regular and a unique solution is obtained. For more common cases and for most of the tomographic models, an underdetermined case, $rank(A) = p = n < m$, is considered, with

$$A^+ = A^T (A^T A)^{-1} \quad (60)$$

and an over determined, but singular case, $rank(A) = p < m < n$ or $rank(A) = p < n < m$, with

$$A^+ = (A^T A + \beta I)^{-1} A^T \quad (61)$$

and

$$A^+ = A^T (A^T A + \beta I)^{-1} \quad (62)$$

proven by Bjerhammar, A., 1973. In both cases the covariance matrix $(A^T A)$ is singular and the solution of the inverse problem will be non unique and probably not stable. For the overdetermined, but singular case the product between a damping factor $\beta \rightarrow 0$ and the identity matrix I makes inverting the covariance matrix $(A^T A)$ stable and thus regularized. Equation (61) is a special form of the g-inverse, obtained for the **damped least square (LSQ) method**.

One of the most powerful techniques to solve singular problems was developed by Eckart, G. and Young, G., 1939 and is known as **singular value decomposition (SVD)**. This method is used to decompose the matrix A into three matrices U , S and V for computing the g-inverse A^+ and can be written as

$$A = USV^T \quad (63)$$

where U is an $n \times n$ orthogonal matrix of normalized eigenvectors of the associated eigenvalue problem $AA^T U = US^2$ and V^T is an $m \times m$ orthogonal matrix of normalized eigenvectors of the associated eigenvalue problem $A^T A V = VS^2$. S is a $n \times m$ matrix containing the singular values of the covariance matrix $(A^T A)$ assigned to the main diagonal of S in a decreasing order, which means that the first n diagonal elements denote the singular values $s_{mn} \neq 0$, while the remaining $s_{mn} = 0$ (Figure 27).

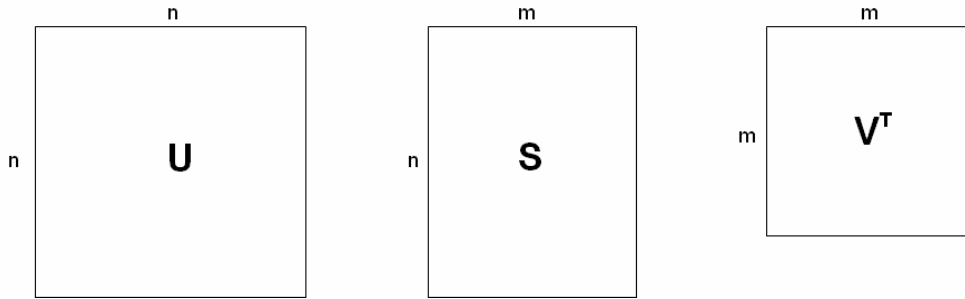


Figure 27: Graphically representation of the singular value decomposition, $A = USV^T$.

Thus the two eigenvector matrices U and V^T can be separated in two submatrices associated with $s_{mn} \neq 0$ (U_p, V_p^T) and $s_{mn} = 0$ (U_0, V_0^T). *Lanczos, C., 1961*, states that the submatrices U_0 and V_0^T do not enter the decomposition process, because they only span up the Null space, which does not contribute to the solution. The rank of U_p and V_p^T , $rank(U_p) = p$ and $rank(V_p^T) = p$, is now identical to the amount of singular values larger than zero. Since S can be treated in the same way, the generalized inverse A^+ can be calculated for the over determined case, $p = m < n$, as follows:

$$A^+ = V_p S_p^{-1} U_p^T \quad (64)$$

where S^{-1} is a $p \times p$ diagonal matrix containing only reciprocal singular values of A with $s_{pp}^{-1} \forall s_{pp} \neq 0$. V_p and U_p^T are $m \times p$ and $p \times n$ matrices, respectively (Figure 28).

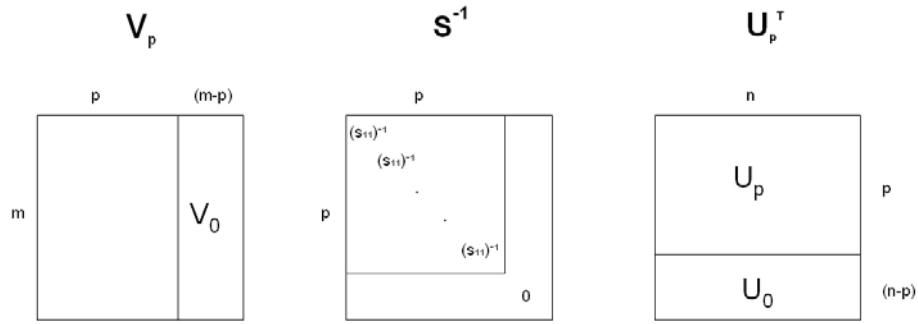


Figure 28: Separation of U , S^{-1} and V into submatrices and graphically representation of the generalized inverse $A^+ = V_p S_p^{-1} U_p^T$.

For more general rank deficient cases $p < \min[m, n]$ the **truncated singular value decomposition (TSVD)** can be applied, which is identical to the damped least square method. Practically, very small singular values are replaced by zero values, $s_{mm} = 0$ and the matrix gets a new pseudorank which leads to stable and smooth solution. In general it is a trade-off between robustness and small travel time residuals. So decreasing the rank p in TSVD is identical to increasing the damping factor β in the damped LSQ method, while the sum of the resulting time residuals increases.

The parameter **epsilon** ε specifies the pseudo rank of the diagonal matrix S and is determined by a relation between the maximum singular value s_{11} and each individual singular value s_{ii} .

$$\varepsilon = \frac{s_{ii}}{s_{11}} \Rightarrow \varepsilon s_{11} = s_{ii} \quad (65)$$

In other words, the product between ε and the first element of the diagonal matrix S , s_{11} , specifies the smallest possible singular value s_{ii} , which will be used in TSVD. Increasing ε provides a lower resolution of the model and higher travel time residuals (*Figure 29*).

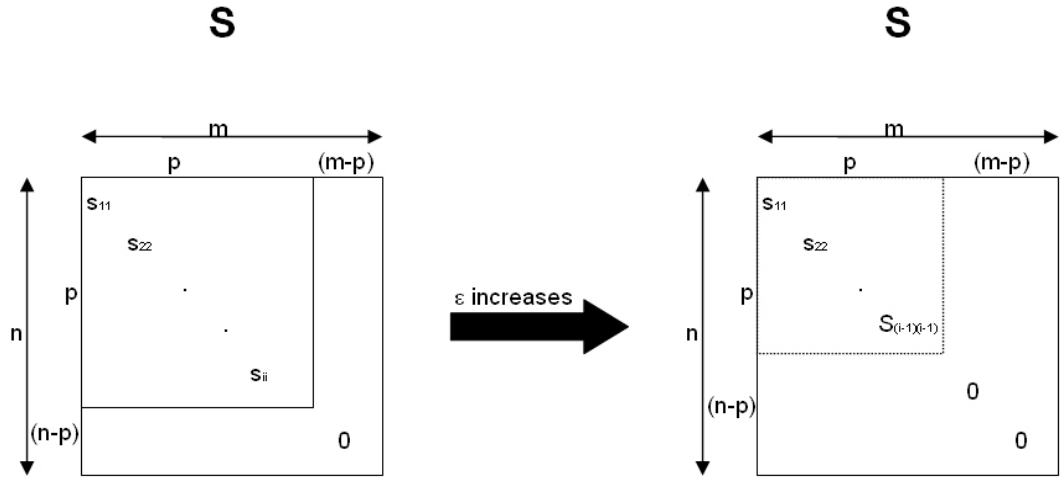


Figure 29: Affects of epsilon ε on the rank of the diagonal matrix S . This case shows that an increasing epsilon decreases the rank of the diagonal matrix S . The singular values of the inverse diagonal matrix S^{-1} are defined by $(s_{ii})^{-1} = (s_{ii})^{-1} \forall s_{ii} \geq \varepsilon \cdot s_{11}$ and $(s_{ii})^{-1} = 0 \forall s_{ii} < \varepsilon \cdot s_{11}$.

Alternatively to the above discussed methods for solving nonlinear and singular problems, back projection techniques are also able to solve such kind of problems. Two of them will be characterized in *Section 4.2.2* and *Section 4.2.3*, while the implementation of TSVD into a robust 1D inversion is discussed in *Section 4.2.3*.

4.2.2 Simultaneous iterative reconstruction technique (SIRT)

The simultaneous iterative reconstruction technique was developed for ray tomography and was applied firstly for high frequency electromagnetic and seismic travel time methods (*Dines and Lytle, 1979*). It improves iteratively the slowness model by projecting slowness perturbations on the ray path. For that reason the model space will be divided into 3D grid cells and travel times $\tau_{calc_i,j}$ for all ray segments through each cell will be calculated so that

$$\tau_{calc_i} = \sum_j u^{idx-1}_{,j} x_{i,j} \quad (66)$$

is the total travel time for the i -th ray, where $u^{idx-1}_{,j}$ is the slowness of the j -th cell and $x_{i,j}$ is the length of the i -th ray through the j -th cell (*Figure 30*). The superscript idx defines iteration index.

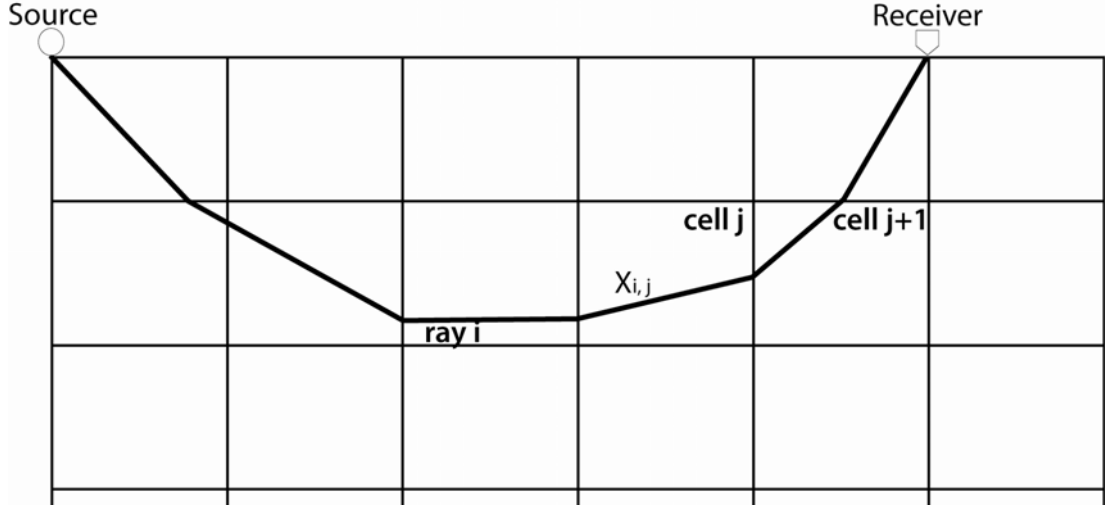


Figure 30: Illustration of SIRT. The model space is subdivided into grid cells with an assigned slowness value u_j .

The comparison with the observed travel times yields to the slowness perturbation of the i -th ray

$$\delta u_i = \frac{\tau_{obs_i} - \tau_{calc_i}}{x_{r_i}} \quad (67)$$

where x_{r_i} is the total length of the i -th ray. Thus the relation for the improved slowness of the i -th ray through the j -th cell $u^{idx}_{,j}$ can be formulated in terms of the reference slowness $u^{idx-1}_{,j}$ and of the perturbation slowness δu_i weighted by the cumulative length of all rays of the j -th cell

$$u^{idx}_{,j} = u^{idx-1}_{,j} + \frac{\lambda}{x_{c_j}} \sum_i \delta u_i x_{i,j} \quad (68)$$

where λ is the relaxation factor. The solution produces a smearing of the slowness perturbations along the ray path. In a homogeneous medium the rays can be assumed as straight, while in heterogeneous media rays have to be calculated by ray tracing.

4.2.3 Nonlinear 3D seismic travel time tomography

This section characterizes a nonlinear travel time tomography based on a processing routine developed by *Hole, J.A., 1992*, to derive a 3D velocity model by forward modelling and inversion of travel times.

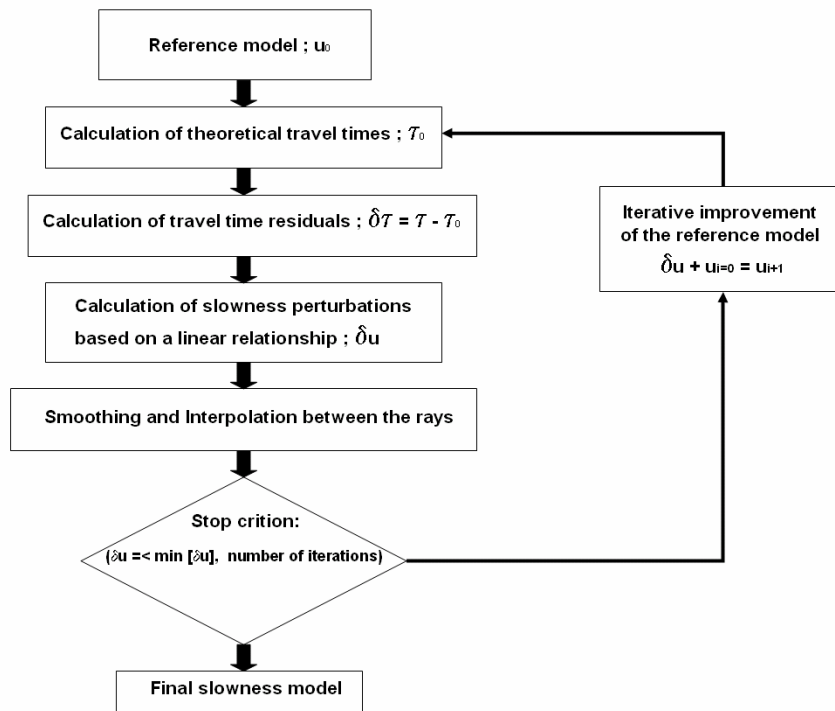


Figure 31: 3D travel time tomography by *Hole, J.A., 1992.*

The calculation of the desired final slowness model requires an iterative process to improve the reference model, beside the reference model is sufficiently close to the real structure of the subsurface. First and foremost initial model and real structure should resemble at their relative structure, as absolute differences can be negligible. Further it is generally better to underestimate peak anomalous values by using a spatially averaged version of the real structure (smoothed initial model) to avoid ray bending, since wrong pre-allocated velocity anomalies can hardly be removed during the iteration sequences.

The method requires a rectangular 3D grid with assigned slowness values. The entirety of the discrete slowness nodes serves as reference model u_0 for the computation of associated theoretical first arrival times τ_0 by a 3D finite difference time algorithm described by *Vidale, J.E., 1990.* This algorithm extrapolates travel times from point to point by using three different schemes based on the Eikonal equation. The calculation of the slowness within the cells depends on the utilized finite difference scheme. The finite difference schemes are formulated to treat also head waves and diffractions properly (*Nelson and Vidale, 1990*) and compared with computational slower ray tracing methods, they also achieve accurate travel times for smooth models and fine grids. Ray paths $S[u_0]$ are calculated by tracing them along the gradient backward from receivers through the computed travel time field. Single rays within a cell can be assumed as straight as the cell size is small enough and are directed along the average slowness gradient across a cell (*Figure 32*).

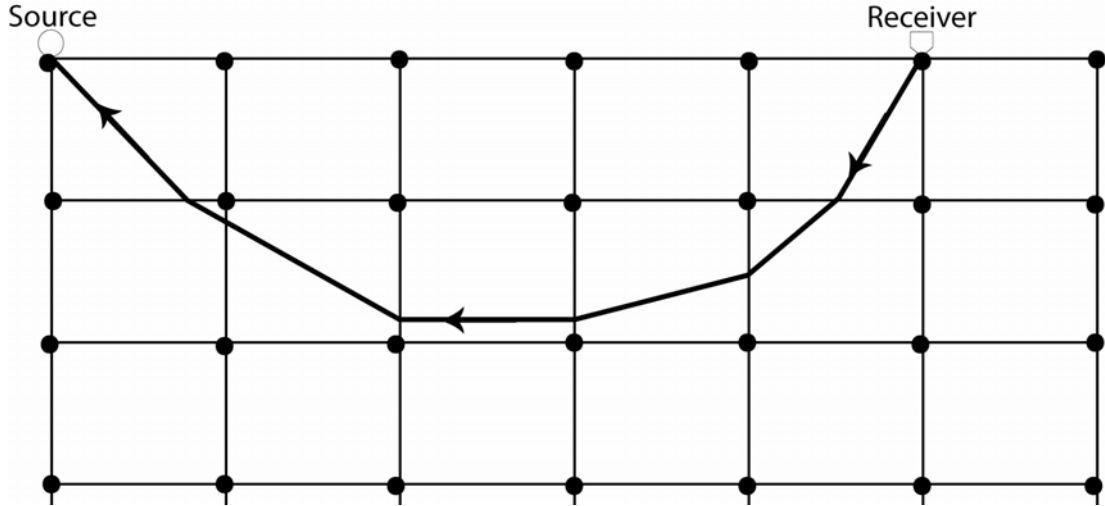


Figure 32: Two dimensional view onto a 3D grid model, which is subdivided into quadratic cells and parameterized at the grid points. *Vidale's* finite difference algorithm identifies the grid points next to the sources as starting points of extrapolation. The ray paths between source and receiver pairs are assumed as straight within the cells and will be calculated backwards from the receiver.

The slowness perturbation δu for a single ray is calculated by solving integral equation (56) by using the ray path $S[u_0]$ and the calculated travel time residuals

$$\delta\tau = \tau - \tau_0 \quad (69)$$

between observed and calculated travel times. The slowness perturbation δu can be distributed over the entire ray path, such that each cell obtains a particular slowness perturbation value δu_j . Since the slowness model is parameterized at the grid points, the slowness perturbation value at each grid point is estimated by taking the arithmetic average of those values assigned to the eight neighbouring grid cells. This operation spreads single perturbation values over a wider area of the model and maintains the validity of the linearization assumption. Additional smoothing can be applied by using a moving 3D average filter. Once all rays have been traced, the slowness perturbation model is added to the reference model, which will be used to start further iteration sequences. During forward modelling the root mean square travel time residual (RMS error) from the previous model is calculated and compared to a defined stop criterion. This procedure is like simple back-projection and the algorithm is very similar to simultaneous iterative reconstruction technique (SIRT) (see also *Section 4.2.2*).

4.2.4 Seismic tomography based on 1D ray tracing and inversion

Based on reference model $v_0(z) = u_0(z)^{-1}$, this inverse method improves the slowness model iteratively, until predefined stop criterions are fulfilled. The iteration process is subdivided in several steps (*Figure 33*). Starting with the calculation of the ray geometry for a simple model by ray tracing (*Section 4.2.4.1*), a linear relationship

between travel time residuals Δt and unknown parameters Δu has to be established by introducing a linear model matrix W (Section 4.2.4.2). The calculation of the model matrix inverse and thus the inversion for Δu is accomplished by applying truncated singular value decomposition (TSVD) (Section 4.2.4.3). The description follows the work by Behm, et al., 2007.

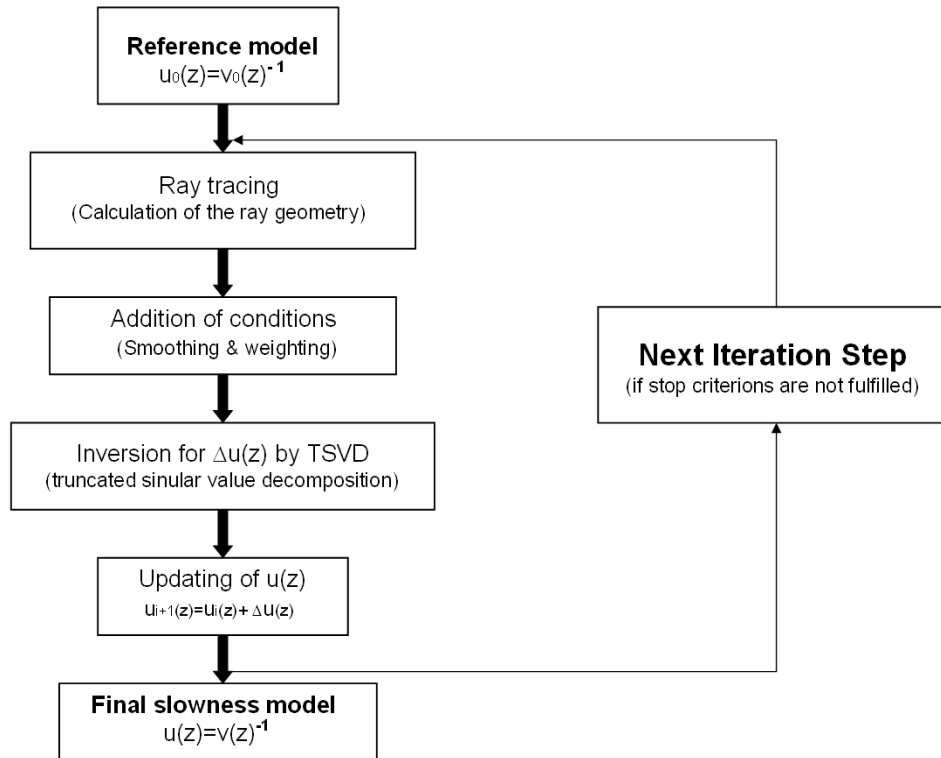


Figure 33: Flowchart of 1D ray tracing and inversion for a velocity function $v(z)$ derived from an observed 1D travel time curve $t_{observed}$.

4.2.4.1 Calculation of ray geometry with 1D ray tracing

From observed travel times, one can reconstruct different ray paths penetrating the model space, which is assumed as sequence of layers with constant velocity gradients (Figure 34).

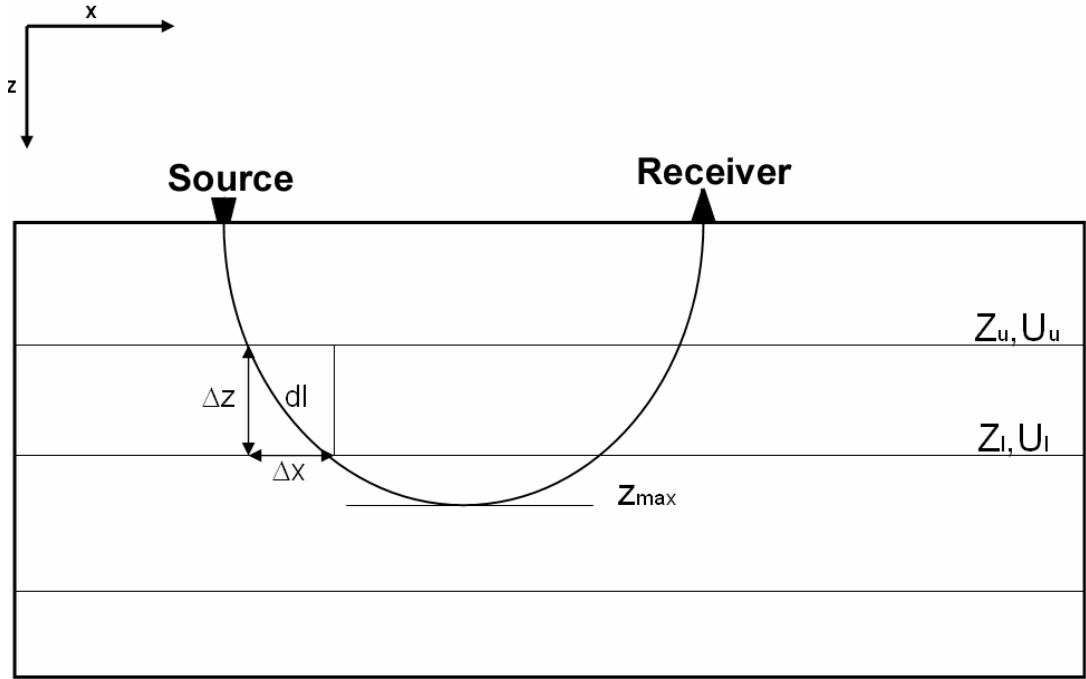


Figure 34: Ray tracing in a flat layered structure. The slowness in each layer $u(z)$ is a function of depth z and can be calculated from the slowness of the upper boundary $u_u(z_u)$ and from the slowness of the lower boundary $u_l(z_l)$. The ray parameter is $p = \frac{1}{v(z_{\max})} = u(z_{\max})$, where $\Delta z = z_l - z_u$.

Ray geometry and travel times for a single ray with a given ray parameters are related as follows:

$$dx = \frac{v(z)p}{\sqrt{1 - (pv(z))^2}} dz \quad (70)$$

$$dt = \frac{1}{v(z)} dl = \frac{1}{v(z)} \cdot \frac{1}{\sqrt{1 - (pv(z))^2}} dz \quad (71)$$

The **basic equations for 1D ray tracing** in a horizontally layered media are derived by integrating the relations above and describe the horizontal offset $x(i)$, which a single ray travels in the time $t(i)$ within the i -th layer.

$$x(i) = \frac{1}{kp} \left(\sqrt{1 - \eta_u^2} - \sqrt{1 - \eta_l^2} \right) \quad (72)$$

$$t(i) = \frac{1}{kp} \left(\arccos\left(\frac{1}{\eta_u}\right) - \arccos\left(\frac{1}{\eta_l}\right) \right) \quad (73)$$

with

$$k = \frac{1}{u_u u_l} \cdot \frac{u_u - u_l}{z_l - z_u} \quad (74)$$

$$\eta_u = \frac{p}{u_u} \quad (75)$$

$$\eta_l = \frac{p}{u_l} \quad (76)$$

4.2.4.2 Generation of the model matrix

The slowness $u(z)$ in an arbitrary layer with a constant velocity gradient and depth z can be formulated as:

$$u(z) = \frac{1}{v(z)} = u_u + \frac{u_l - u_u}{z_l - z_u} (z - z_u) \quad (77)$$

Since the slowness $u(z)$ is a reciprocal function of the linear velocity $v(z)$, it is not really linear, but it can be considered as linear approximation. Thus equation (77) can be used to derive an alternative equation (78), which is introduced to define a linear relation for $u(z)$ in terms of $u_u(z_u)$ and $u_l(z_l)$.

$$u(z) = \frac{1}{v(z)} = u_u \frac{z_l - z}{z_l - z_u} + u_l \frac{z - z_u}{z_l - z_u} \quad (78)$$

Based on equation (79), which can be extended to a linear system of equations for n travel time observations (*see equation (85)*),

$$\Delta t = W^T \begin{pmatrix} u_u \\ u_l \end{pmatrix} \quad (79)$$

one achieves a linear relationship between travel time Δt and slowness $\Delta u(z)$ for a single ray by inserting equation (78) into equation (71). This is expressed by a model matrix W , which is specified by the initial velocity model $v_0(z) = u_0(z)^{-1}$. This will be possible, if one assumes, that the initial model $v_0(z) = u_0(z)^{-1}$ is approximately in accordance with the real velocity model $v(z) = u(z)^{-1}$, see equation (80).

$$W = \begin{bmatrix} \int_{z_u}^{z_l} \frac{z_l - z}{z_l - z_u} \frac{1}{\sqrt{\sqrt{1 - (pv_0(z))^2}}} dz \\ \int_{z_u}^{z_l} \frac{z - z_u}{z_l - z_u} \frac{1}{\sqrt{\sqrt{1 - (pv_0(z))^2}}} dz \end{bmatrix} = \begin{bmatrix} C_u A + B \\ C_l A - B \end{bmatrix} \quad (80)$$

$$A = \arcsin(\eta_u) - \arcsin(\eta_l) \quad (81)$$

$$B = \frac{\sqrt{1 - \eta_u^2} - \sqrt{1 - \eta_l^2}}{p^2 k^2 (z_u - z_l)} \quad (82)$$

$$C_u = \frac{1 + k \cdot u_u (z_l - z_u)}{p \cdot u_u \cdot k^2 (z_u - z_l)} \quad (83)$$

$$C_l = \frac{-1}{p \cdot u_u \cdot k^2 (z_u - z_l)} \quad (84)$$

4.2.4.3 Inversion for Δu by truncated singular value decomposition (TSVD)

The linearization of the inverse problem in *Section 4.2.4.2* yields a linear relationship between n travel time residuals Δt and m unknown slowness improvements Δu , expressed by the product between a $n \times m$ model matrix W and the slowness improvements Δu .

$$\Delta t = W \Delta u \quad (85)$$

Since fully determination of the linear system is not a priori assumed, $\text{rank}(W) = p = m = n$, the utilization of TSVD (*Section 4.2.1*), is an important issue of solving equation (85). Multiplication with the generalized inverse W^+ gives a unique solution for the slowness perturbation in the linear equation system:

$$W^+ \Delta t = \Delta u \quad (86)$$

with

$$W^+ = VS^{-1}U^T \quad (87)$$

Epsilon ε is not the exclusive parameter controlling the inversion process, there are several other parameters affecting the final velocity–depth model, which will be discussed below.

The weighting of observed travel times with respect to their offset minimizes the effect of lacking travel times with short offsets and is controlled by a weighting

factor f_w . Mathematically the weighting $w(x)$ of observed travel times can be formulated as function of the offset x :

$$x \leq \frac{x_{\max}}{f_w} \Rightarrow w = f_w \quad (88)$$

$$x > \frac{x_{\max}}{f_w} \Rightarrow w = \frac{x_{\max}}{x} \quad (89)$$

| | |
|------------|--|
| x | Offset |
| x_{\max} | Maximum offset |
| f_w | Weighting factor |
| $w(x)$ | Weighting of travel times in respect to the offset |

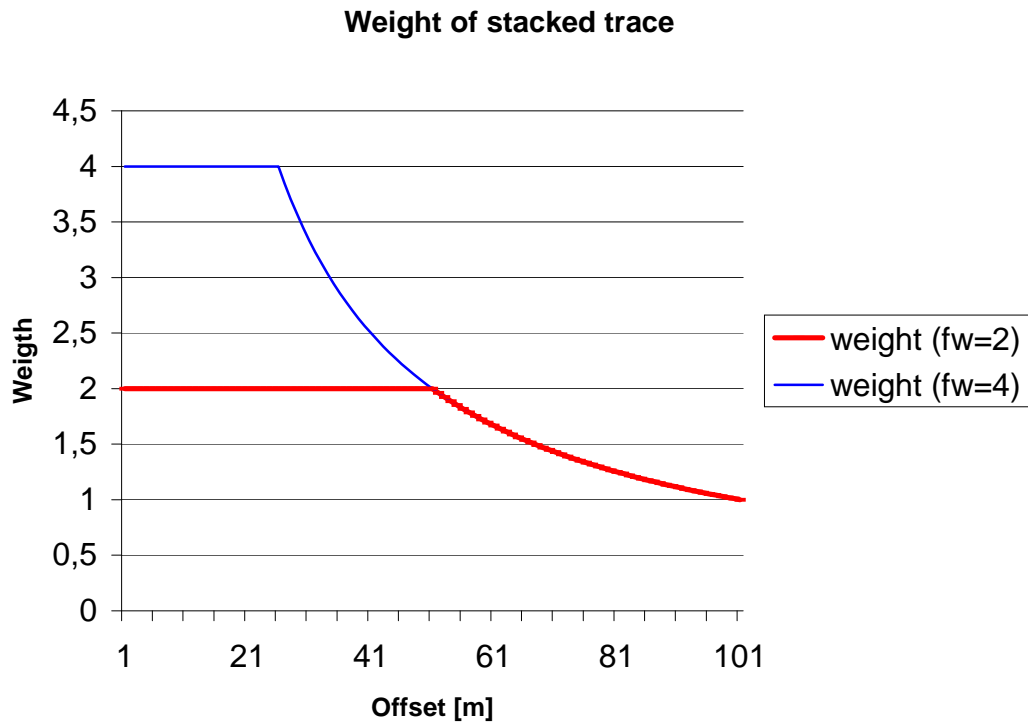


Figure 35: Weighting curves for two weighting factors, $f_w = 2$ and $f_w = 4$. It is obvious, that f_w specifies weighting as a function of the offset.

Smoothing factor f_s scales the smoothing operator Ψ . The smoothing operator is based on the second derivation of the velocity-depth function and can be alternatively formulated as

$$f_s \in \mathbb{N} \Rightarrow f_s \cdot \Psi \quad (90)$$

and for $f_s = 1$ as:

$$\Psi = [-1 \quad 2 \quad -1] \quad (91)$$

By adding m rows with those three elements of the smoothing operator Ψ to model matrix W , the model matrix will be extended to a $n+m \times m$ matrix W' . The smoothing operator Ψ is arranged diagonally (Figure 36) and fulfils the following side condition:

$$\Psi \Delta u = -1u_1 + 2u_2 - 1u_3 = 0 \quad (92)$$

Equation (85) can be rewritten as:

$$\Delta t' = W' \Delta u \quad (93)$$

The side condition (92) will be valid for $u_1 = u_2 = u_3$. The smoothing operator demands that the slowness improvements for three adjacent velocity nodes should be as smooth as possible, thus the curve of the resulting slowness model becomes minimal. The application of the smoothing condition proceeds before SVD.

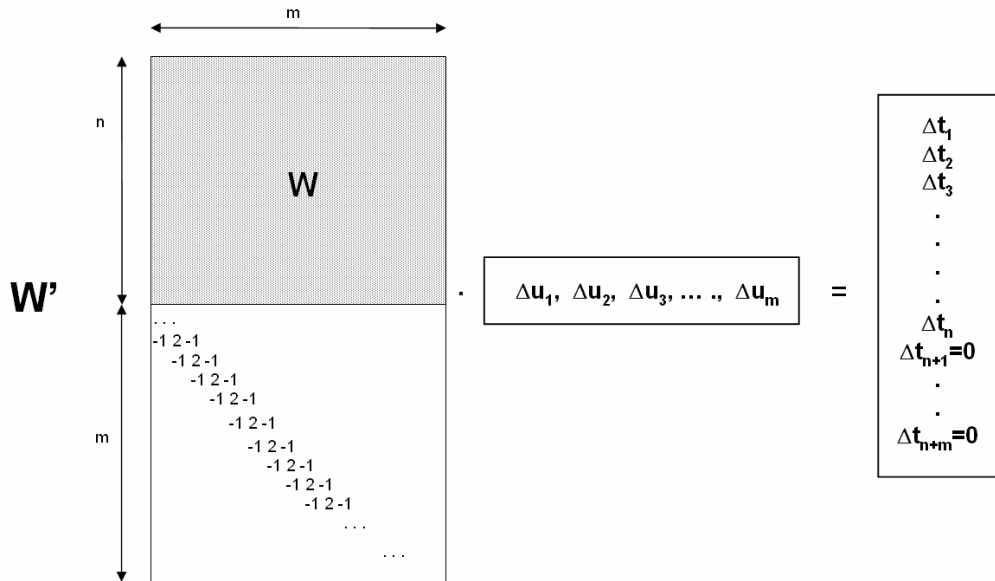


Figure 36: Graphically description of $n+m \times m$ matrix W' and equation (93). Due to side condition (92), the $n+1$ travel time elements are reduced to zero.

Relaxation factor f_R scales the calculated slowness perturbations Δu , before adding them to the present slowness model $u_i(z)$ during the iteration process. The purpose of this scaling operation is that the iterative inversion process will converge rather, if the slowness perturbations are small.

$$u_i(z) + f_R \cdot \Delta u = u_{i+1}(z) \quad (94)$$

The **default gradient** δ_s is used to define the velocities below the deepest penetration depth of all rays by multiplication with the velocity of the deepest estimated layer. If this default gradient is not included in the inverse operation, the calculated velocity model will implement the missing velocity structures below the deepest velocity node from the initial model (*Figure 37*).

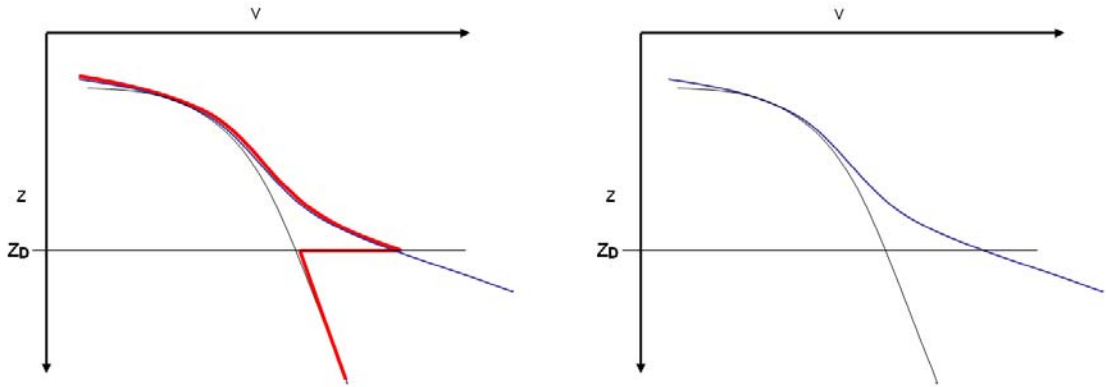


Figure 37: Illustration of using the default gradient δ_s . The right sketch shows a velocity-depth model $v(z)$ (blue line) with an assumed default gradient for deeper regions $z > z_D$ and the assigned reference model $v_0(z)$ (black line). The left sketch shows the effects of not using a default velocity gradient below the deepest defined velocity node with depth z_D (red line). For $z > z_D$ the reference model is used to calculate velocities below and thus $v(z)$ becomes discontinuous.

The parameter **number of rays** defines the total amount of rays, which are utilized for ray tracing. Increasing this parameter provides a better coverage of rays with different offsets. This ensures reliable modelling of the subsurface even though strong and weak velocity gradients alternate.

Finally iteration process will be finished, if one of the selected stop criterions is fulfilled. If the difference between two iterative calculated travel times will be smaller than **stop criterion** Δt_{\min} , the iteration sequence will abort and if not, the iteration process will stop anyway after a **maximum number of iterations**.

$$\Delta t_{\min} \leq \Delta t \Rightarrow \text{Iteration stops!} \quad (95)$$

5 Application of seismic travel time tomography on a selected 3D data set

Seismic travel time tomography, whose name is proper derived from a medical imaging technique, describes two- and three-dimensional imaging of attributes of a medium. *Section 5.1* describes the processing of a seismic tomography based on 1D inversion and *Section 5.2* describes the processing of a 3D travel time tomography developed by *Hole, J.A., 1992*.

5.1 Generation of 1D travel times and inversion

1D ray tracing and inversion enables imaging of a horizontally layered model based on the first arrivals of stacked traces. To achieve this, traces were sorted by their common mid point and associated to a common offset bin. Finally those common offset binned data sets were stacked, picked (*Section 3.2.2.2*) and inverted to a velocity-depth model (*Section 5.1.1*). This processing sequence is illustrated in *Figure 38*.

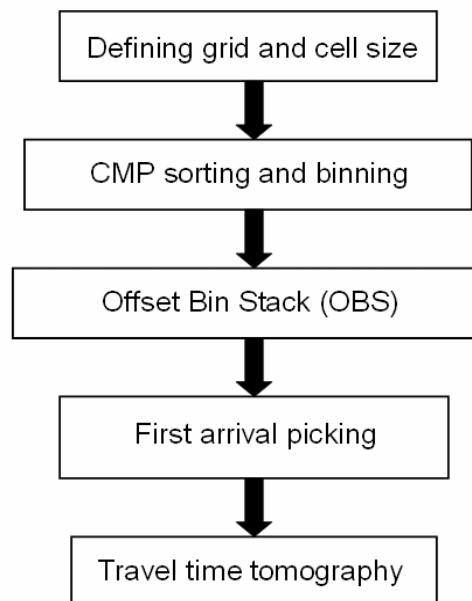


Figure 38: Illustrating of necessary processing steps for a typical seismic tomography sequence based on 1D ray tracing and inversion.

5.1.1 Inversion of travel times to a velocity-depth model

Running the 1D inversion algorithm, which is described in *Section 4.2.3*, requires the creation of an input file containing travel time information and geometric information. The ProMAX pick file contains CMP numbers, the absolute offset of each stacked trace and the travel times of the first arrivals. Next to the geometry file,

which is described in *Section 3.2.2.1*, the inversion of travel times requires an initial model that will be iteratively improved. *Behm, et al. (2007)* confirmed in tests that results of 1D inversion are independent from the initial model and only affect the computational speed. For testing purposes four different starting models (*Figure 39*) were chosen.

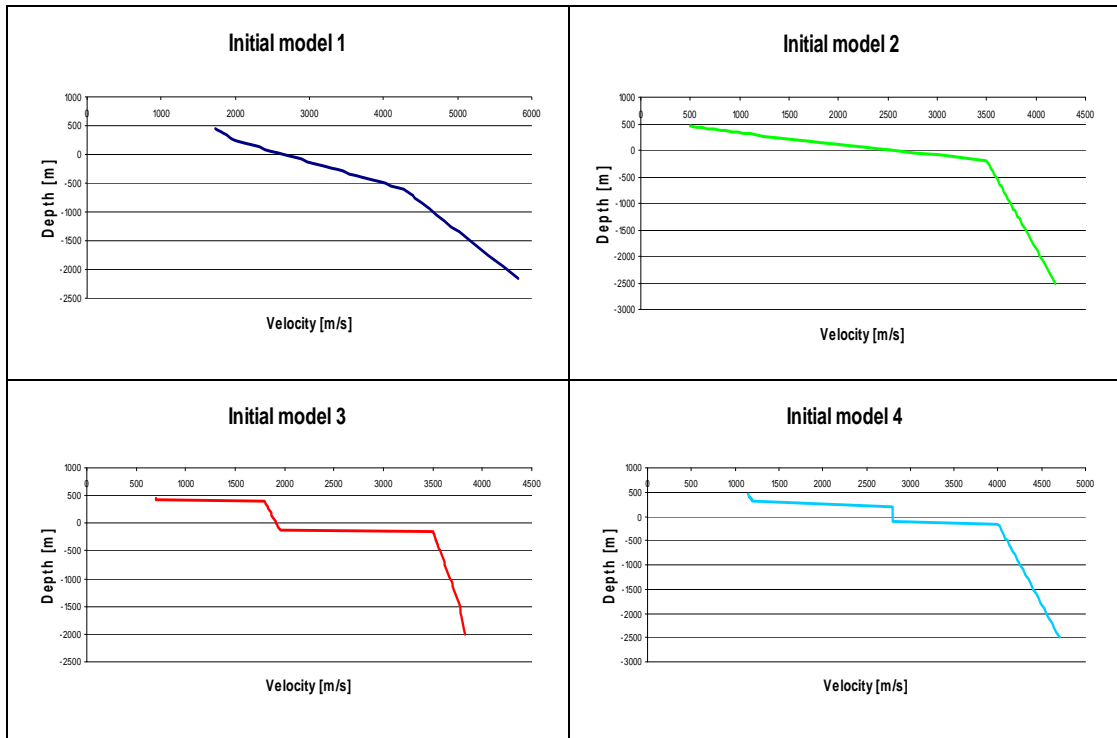


Figure 39: Four initial models for 1D ray tracing and inversion with varying velocity steps and velocity gradients.

In addition to the input file eight parameters controlling the 1D inversion sequence (*Section 4.2.4.3*) were defined. Decreasing ε values leads to the best improvement of the calculated model and minimizes the travel time error down to 10^{-3} [s]. Increasing the size of the smoothing operator leads to steadily approaching of the calculated model to the initial model. The reason of this behaviour is based on the fact that the smoothing operator is only applied on slowness improvements instead of the entire model and thus iterative improvements are virtually zero for non smooth initial models. As a result it can be stated that initial models should be as smooth as possible with a reasonable velocity gradient. The remaining parameters do not show significant effects on the resulting model, therefore they were appointed as default and the numbers of iterations were also abridged to reduce computational time.

Initial model 2 was chosen as initial model, as it provides the best fitting, the smallest travel time errors and the calculated model also shows a higher grade of independence on it. *Figure 40* to *Figure 42* represent the inverse solution for some selected offset bin stacks in comparison to the picked travel times of the assigned single fold section. In general, strong slope changes can only be resolved in a smoothed way and the calculated travel time curves correlate with single picks. Even

in areas with low stack quality, computed travel time curves represent trend lines (Figure 42).

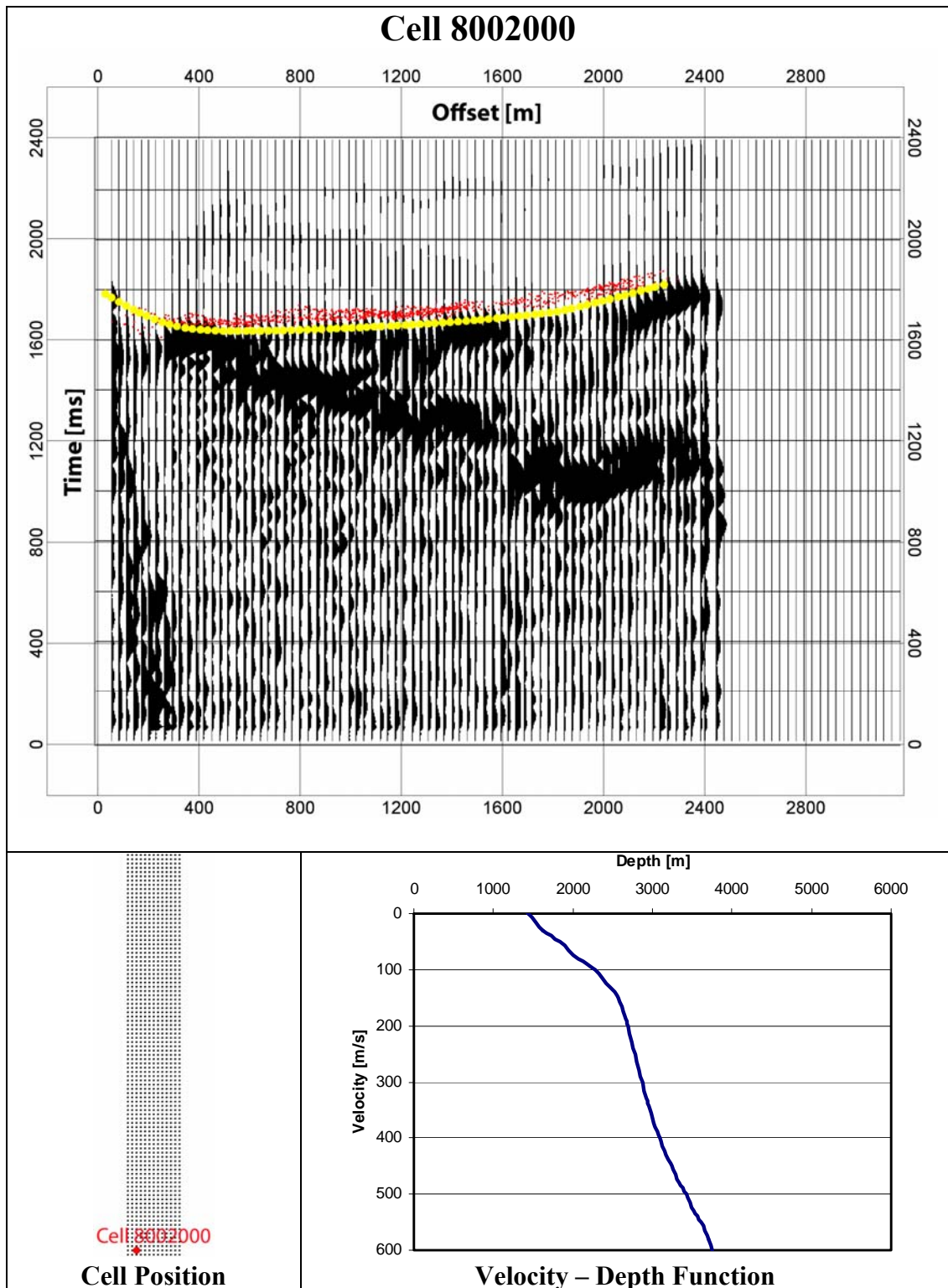


Figure 40: The top part shows the offset bin stack of cell 8002000, the inverted travel times from the stacked section (yellow dots) and the picked travel times from a single fold section (red dots). The time axis is reversed and scaled. The bottom left part shows the position and the bottom right part shows the velocity-depth function of the offset bin stack.

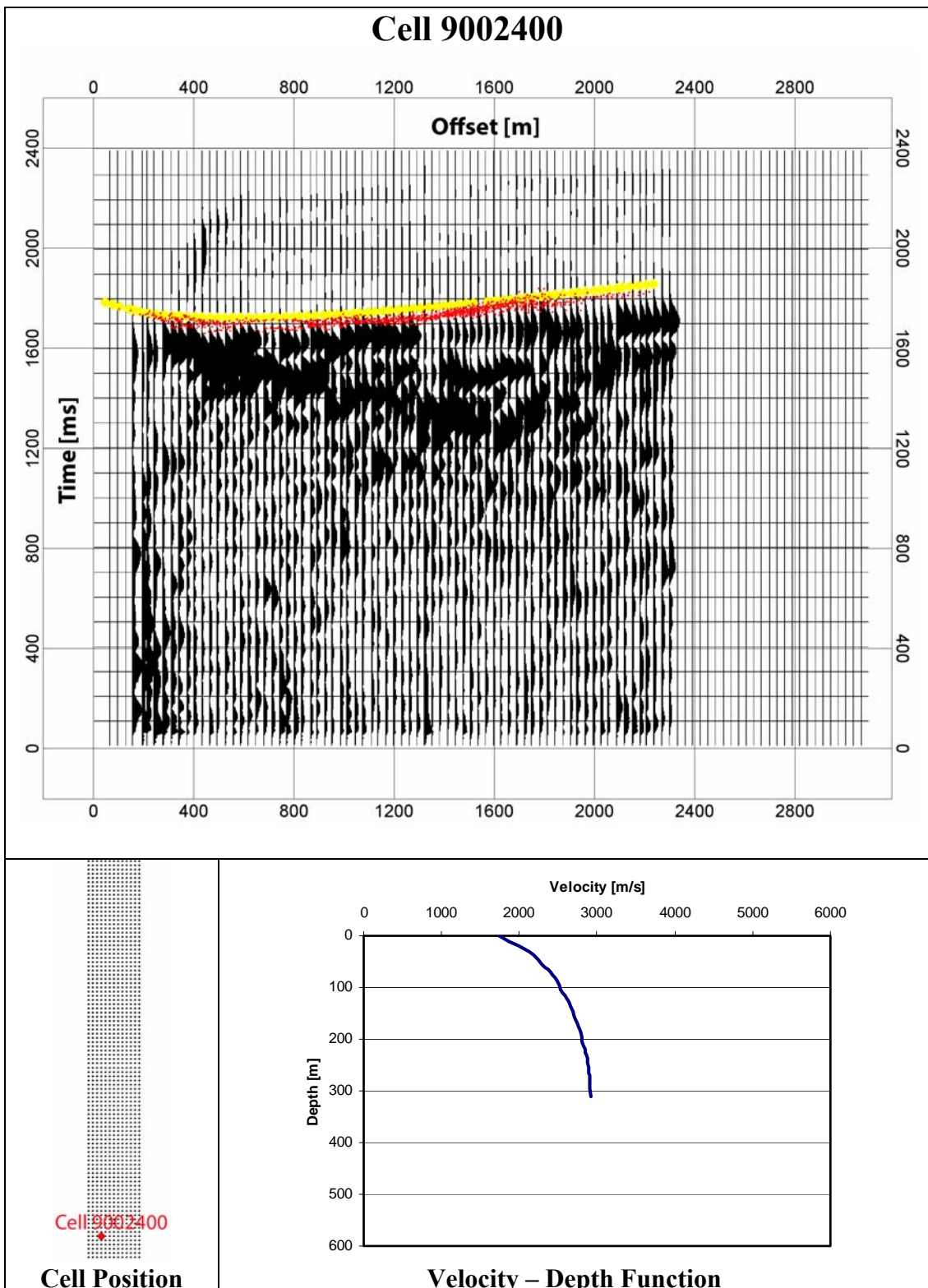


Figure 41: The top part shows the offset bin stack of cell 9002400, the inverted travel times from the stacked section (yellow dots) and the picked travel times from a single fold section (red dots). The time axis is reversed and scaled. The bottom left part shows the position and the bottom right part shows the velocity-depth function of the offset bin stack.

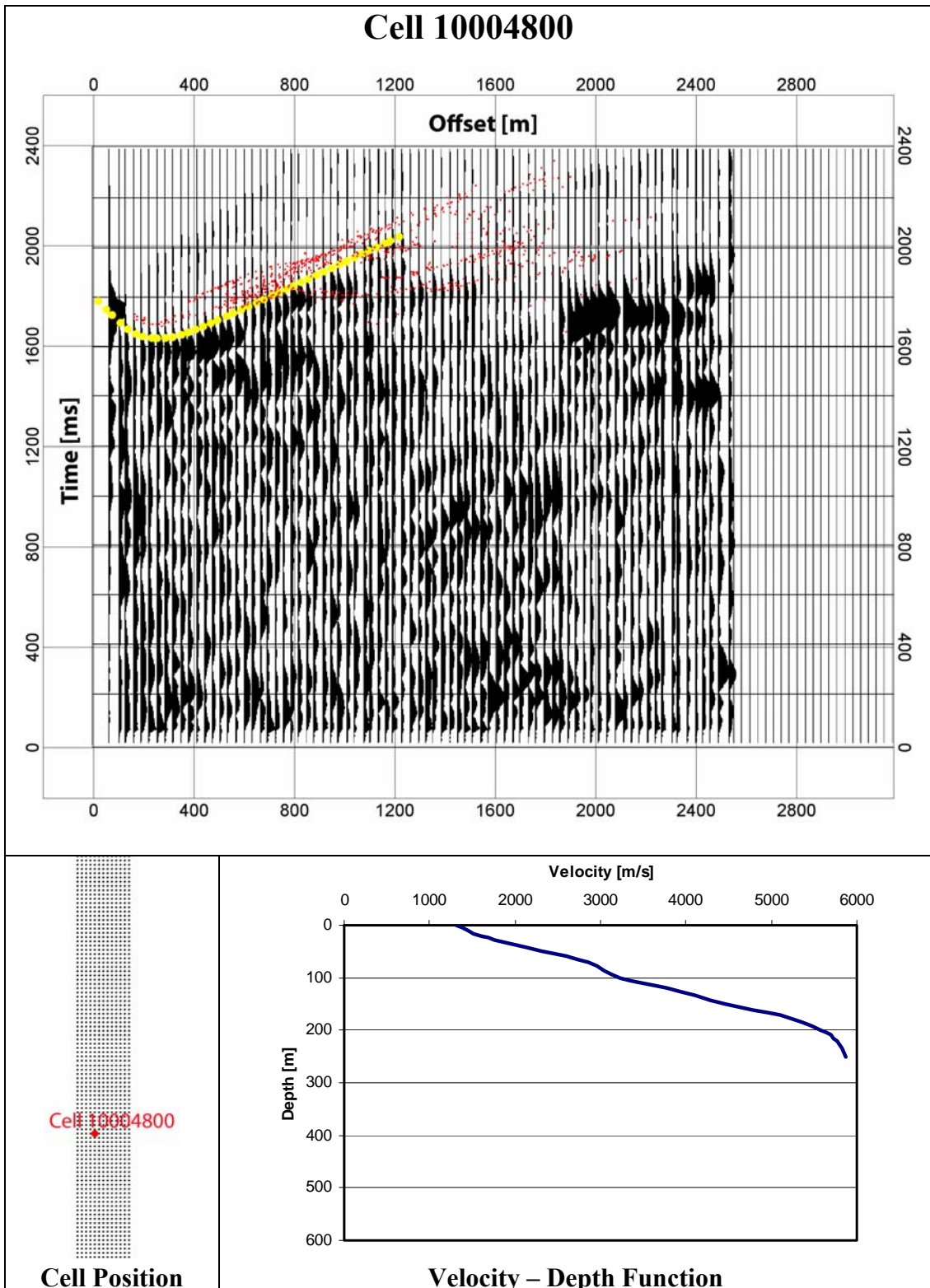


Figure 42: The top part shows the offset bin stack of cell 10004800, the inverted travel times from the stacked section (yellow dots) and the picked travel times from a single fold section (red dots). The time axis is reversed and scaled. The bottom left part shows the position and the bottom right part shows the velocity-depth function of the offset bin stack.

5.1.2 Composition and quality control of the seismic model

The 1D inversion was performed for all in all 1023 cells regular arranged on a grid (Figure 18). To improve the near surface model, some outliers have to be removed and for that purpose an iso-surface was defined which the first elevation point determines within a certain velocity interval (3500-3700[m/s] - corresponding to assumed limestone velocity). This surface represents points within a constant velocity window corresponding to their maximum elevation. The outliers were detected by visually inspection (Figure 43) and removed from data set.

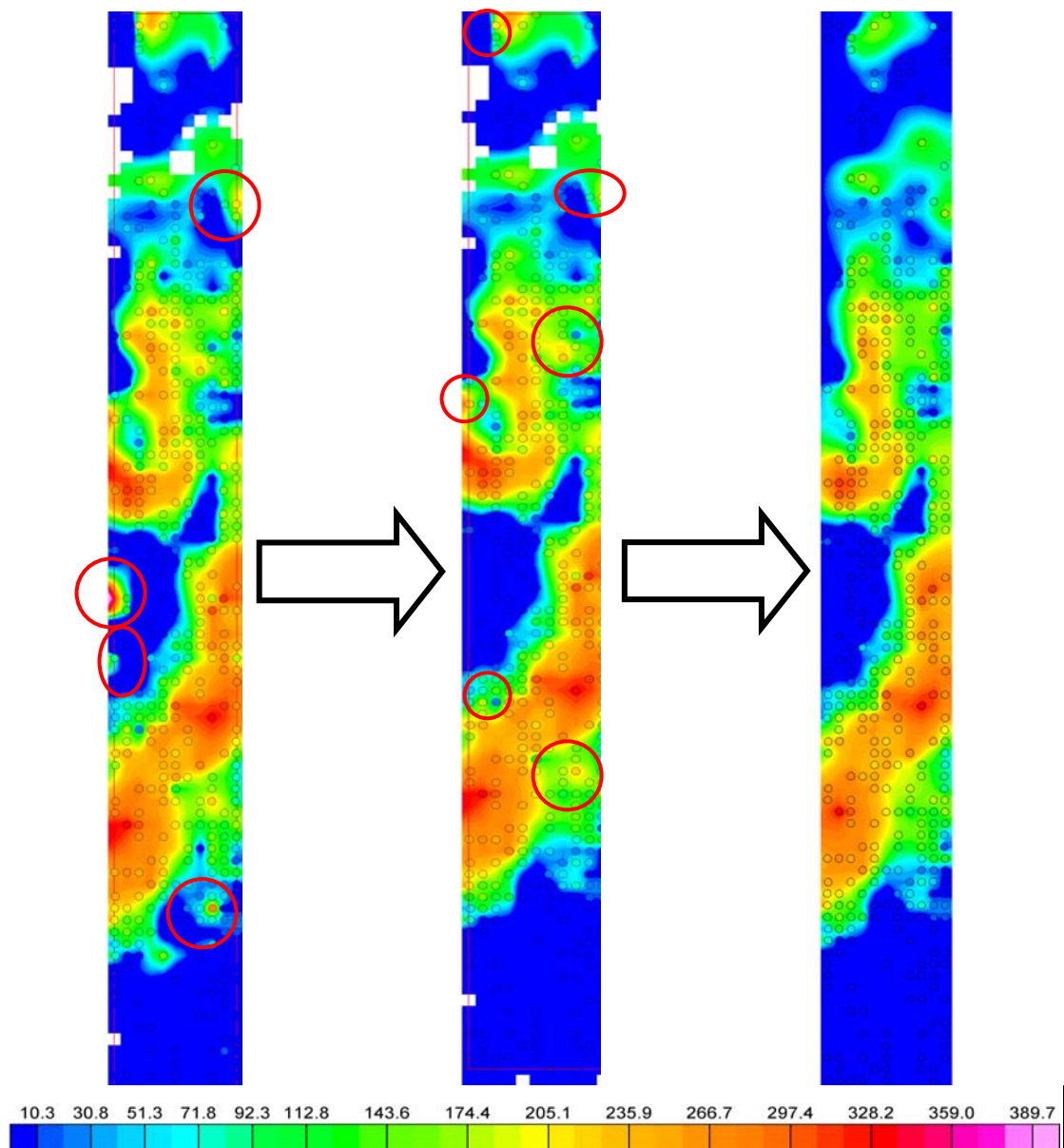


Figure 43: Deleting outliers by visually inspection. The elevation grid with a maximum depth identically to the mean sea level is derived from the elevation of inverted velocity nodes within a velocity interval between 3500-3700 m/s. Selected outliers (some of them are represented as red circles), which are elevation points varying more than 60-80 metres from their neighbouring points, were removed from original data set in steps. The final version on the right hand side shows a homogeneous and smooth iso-surface.

5.1.3 Visualization of a three dimensional velocity model

The edited data set was imported into the seismic modelling and interpretation platform GOCAD as point set. With this point set the investigated velocity model space can be modelled by creating a Voxet, which is a regular 3D grid consisting of volume elements called Voxels. A Voxet is defined by its origin (X_0, Y_0, Z_0), by the number of grid points along each axis (n_u, n_v, n_w) and by its end points (point_u(X, Y, Z), point_v(X, Y, Z), point_w(X, Y, Z)). The velocity information is carried at the grid points, which are representing the centre of the cells. The entire cell gets the same property (e.g. velocity) and is called Voxel (Figure 44).

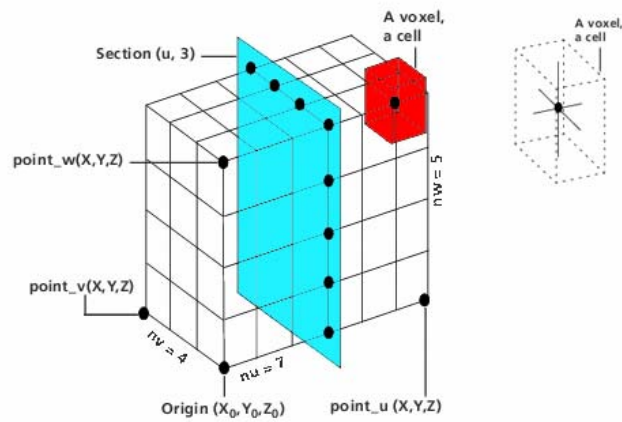


Figure 44: Illustration of a Voxet defined by its end points and of its components, called Voxels.

The cell size and thus the spatial resolution were chosen according to cell geometry of the 1D inversion and the deepest possible model plane was assumed at -450[m] below sea level (Table 3).

| Origin of the Voxet | Number of grid points | End points of the Voxet |
|---------------------|-----------------------|--|
| $X_0=750$ [m] | $N_u=10$ | point_u(X, Y, Z)=(1650, 2050, 450) |
| $Y_0=2050$ [m] | $N_v=92$ | point_v(X, Y, Z)=(750, 11150, 450) |
| $Z_0=450$ [m] | $N_w=64$ | point_w(X, Y, Z)=(750, 2050, -450) |

Table 3: Dimension and resolution of the final velocity model V_{Inv}^{1D} derived by 1D ray tracing and inversion.

To obtain a image of resolved three dimensional velocity structures, the model was divided in a several representative cross sections along each axis. Further the bird's eye view of the digital terrain model including the survey area should provide an overview of the relative dimension of the model and a comparison of the topography with structures of the subsurface. For this only original seismic velocities derived from 1D inversion were assigned to volume elements of the model with an expected velocity interval between 1000[m/s] and 5500[m/s], while volume elements with no data values got transparent (Figure 45 - Figure 47).

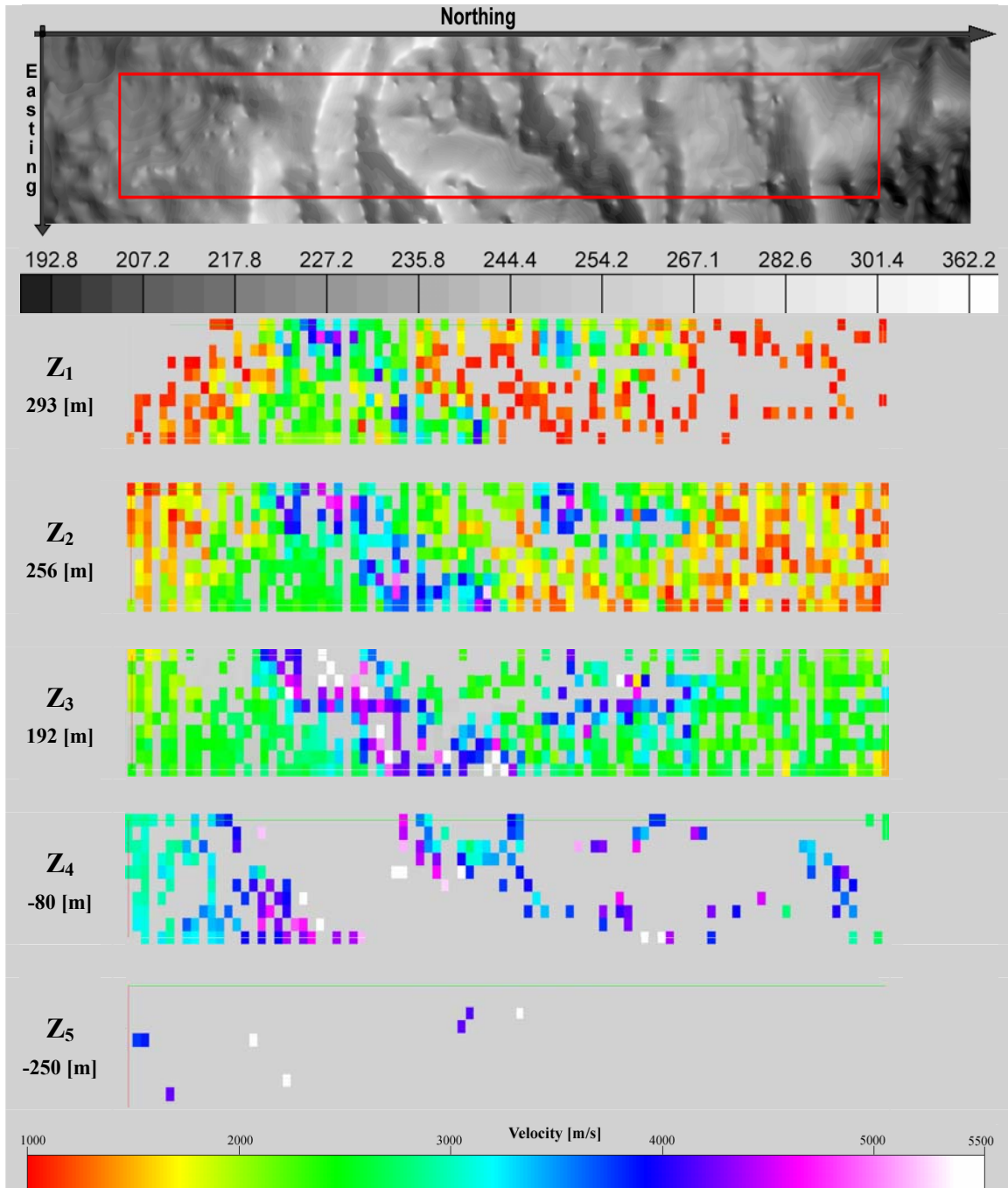


Figure 45: Depth slices along the z-axis (w-axis). The top part shows the surface relief, the processed survey area (red box), while the bottom part shows five depth slices through the seismic velocity model V_{Inv}^{1D} derived from 1D inversion with increasing depth.

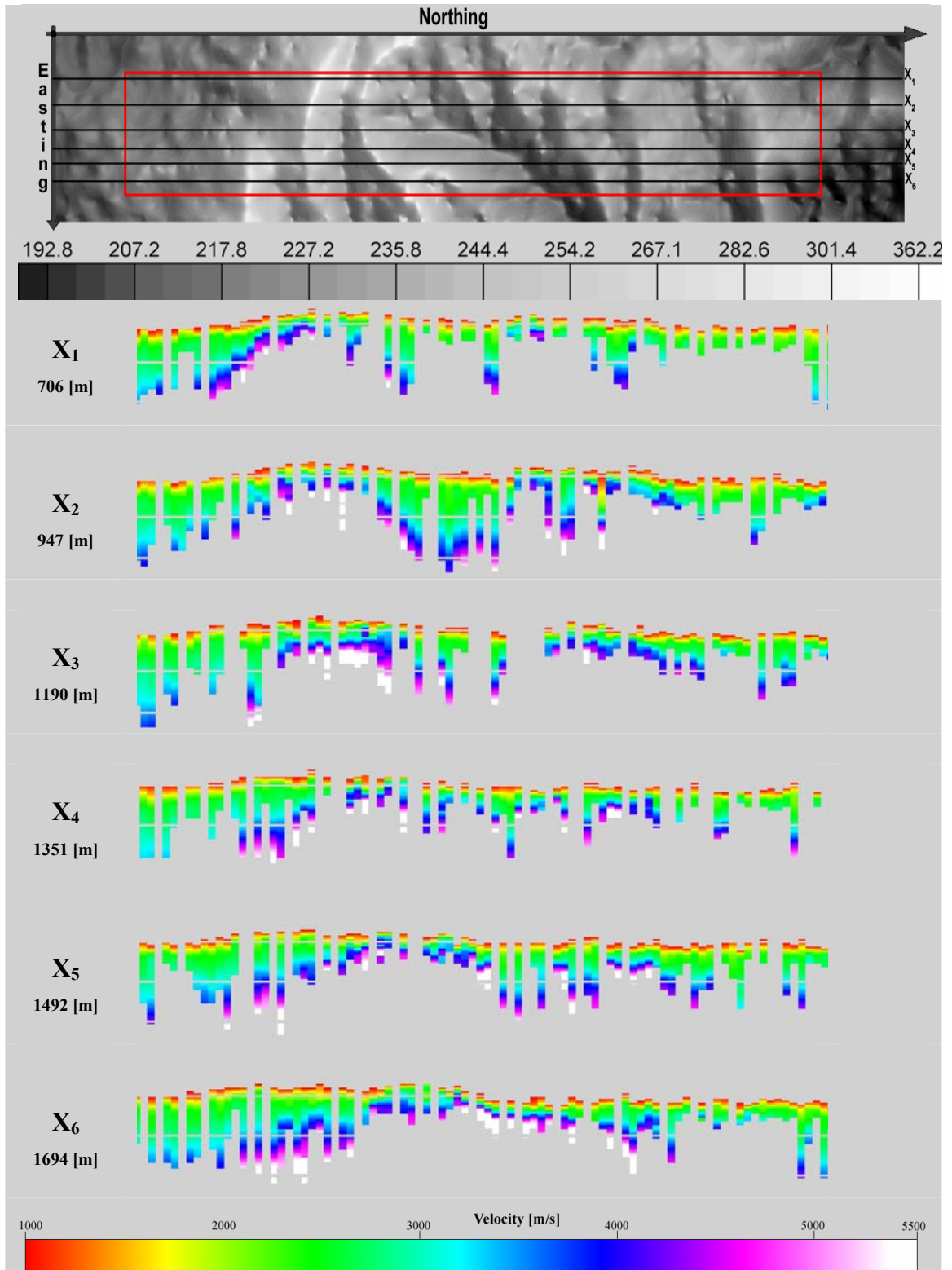


Figure 46: Cross sections along the x-axis (u-axis). The top part shows the surface relief, the processed survey area (red box), while the bottom part shows six cross sections through the seismic velocity model V_{Inv}^{1D} derived from 1D inversion with increasing x-values.

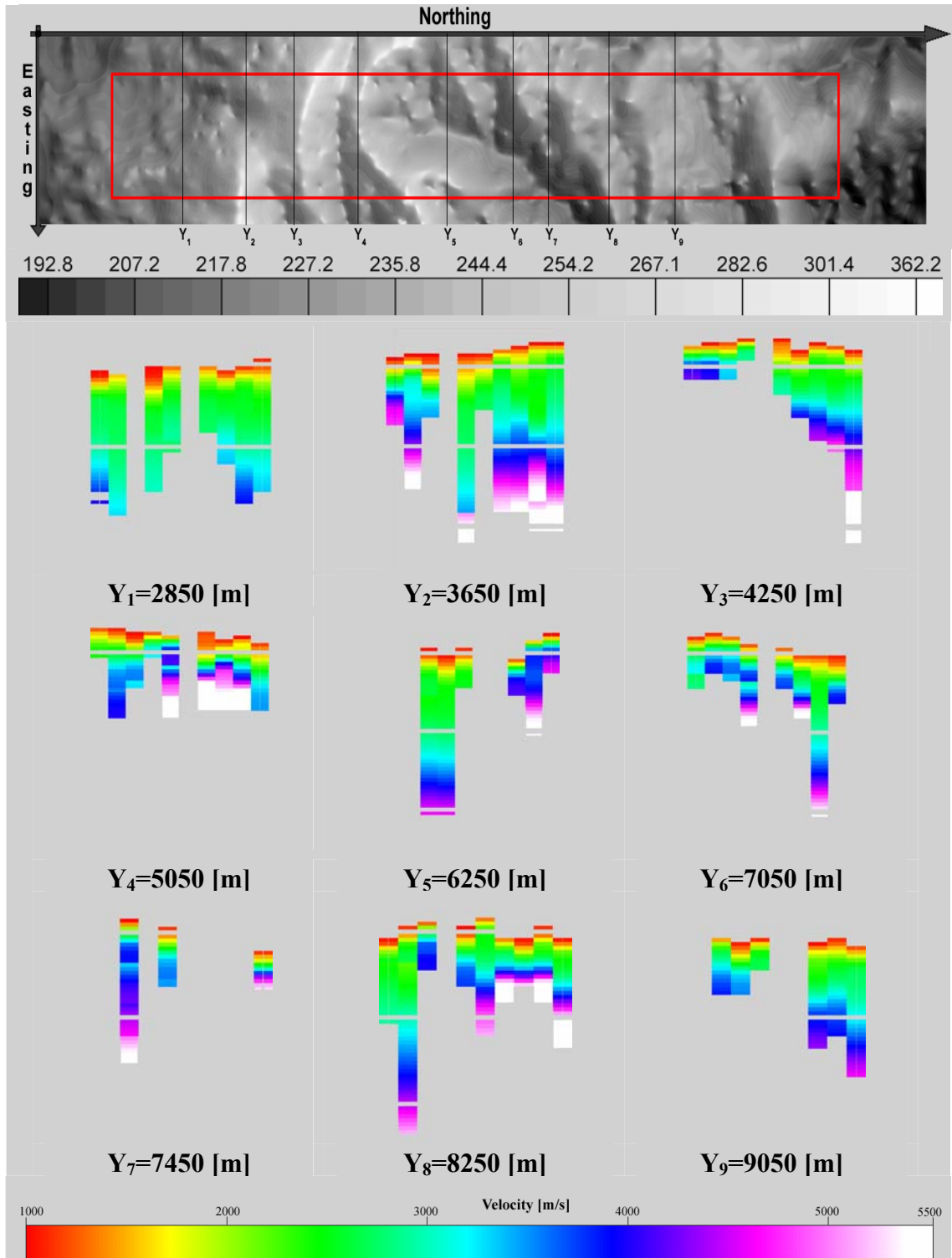


Figure 47: Cross sections along the y-axis (v-axis). The top part shows the surface relief, the processed survey area (red box), while the bottom part shows nine cross sections through the seismic velocity model V_{Inv}^{1D} derived from 1D inversion with increasing x-values.

Since the horizontal distribution of Voxels is quite sparse, the entire model was smoothed by using a cubic average filter with an operator length of six Voxels in each direction. To avoid undesired extrapolations, the model is constrained at the top by the topography and at the bottom by a surface depending on maximum penetration depth of every inverted cell (*Figure 48 - Figure 50*).

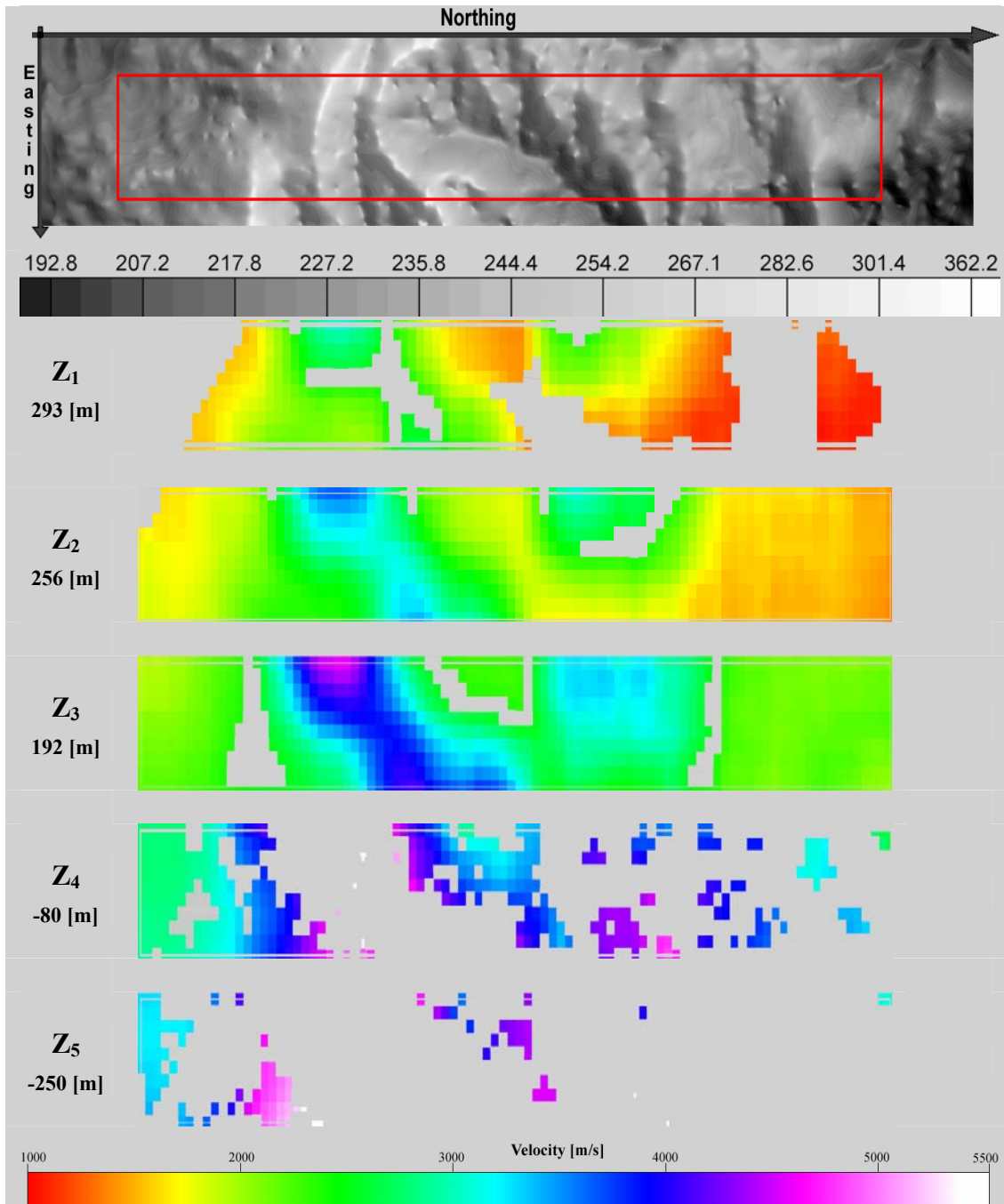


Figure 48: Depth slices along the z-axis (w-axis) with increasing depth through a smoothed velocity model. The top part shows the surface relief, the processed survey area (red box), while the bottom part shows five selected cross sections.

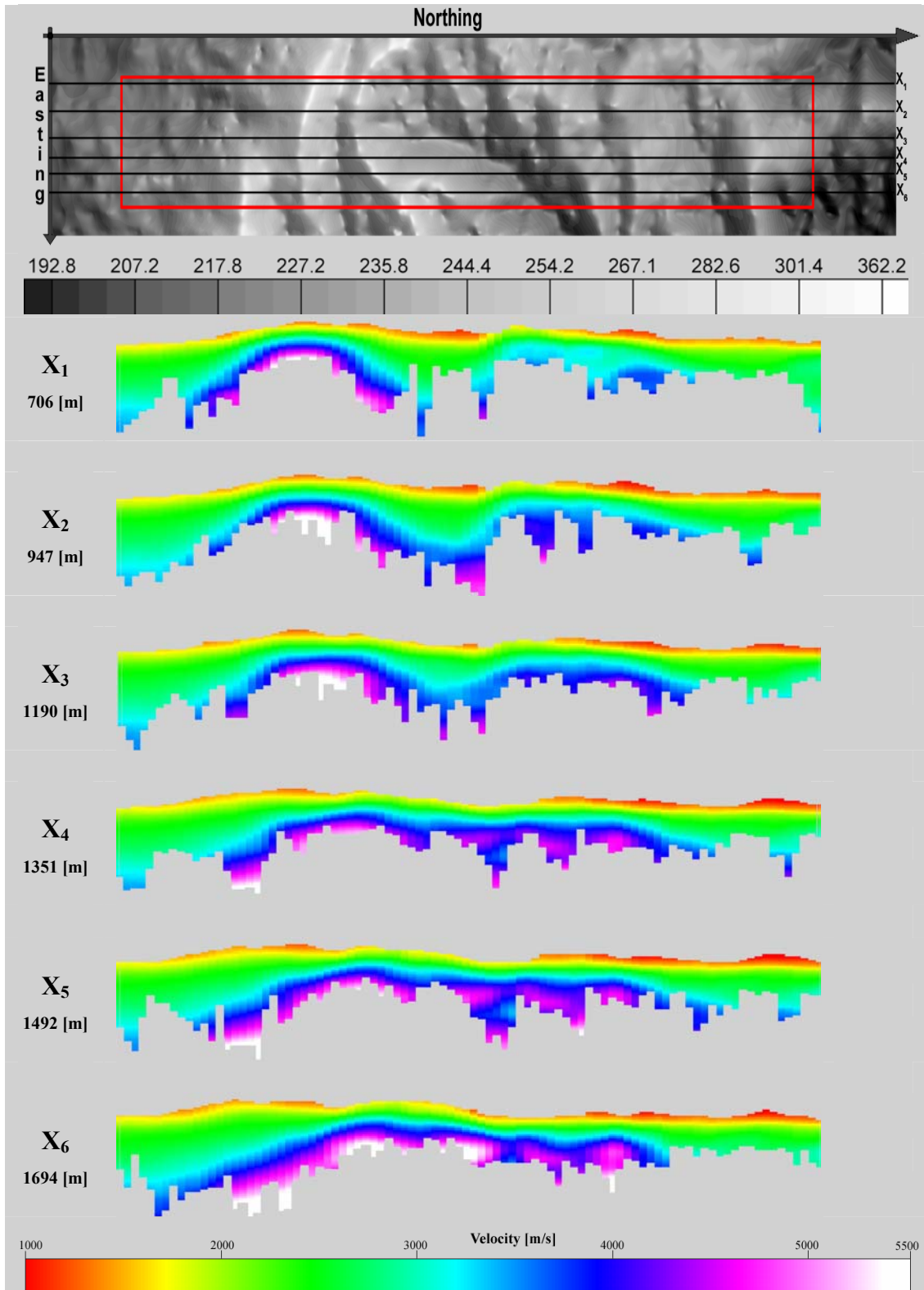


Figure 49: Cross sections along the x-axis (u-axis) with increasing x-values through a smoothed velocity model. The top part shows the surface relief, the processed survey area (red box), while the bottom part shows six selected cross sections.

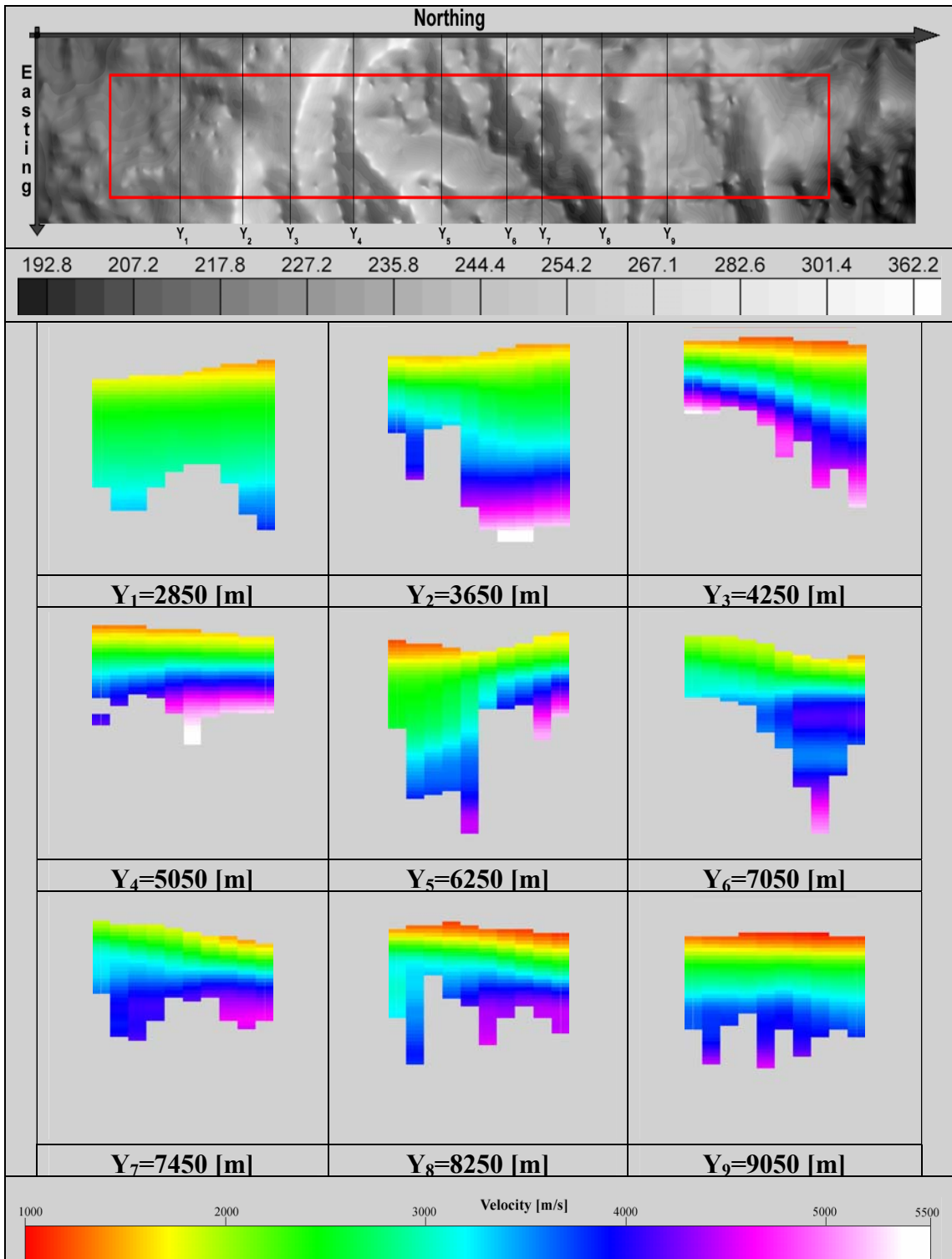


Figure 50: Cross sections along the y-axis (v-axis) with increasing y-values through a smoothed velocity model. The top part shows the surface relief, the processed survey area (red box), while the bottom part shows nine selected cross sections.

To simplify matters the complex 3D model can be considered as series of 2D velocity structures composed of a weathering layer ($V_0 < 1700$ [m/s]), a sediment overburden ($V_1 = 1700-3200$ [m/s]) and a high velocity zone ($V_2 = 3200-5000$ [m/s]). Especially observed rising high velocity zones (HVZ) are of particular interest. These structures, complicating static corrections, divide the survey area into three parts. While the southern and the northern part show thick sediment overlay, the undulating HVZ in the middle part reaches nearly the surface (*Figure 51*). The lateral distribution of the high velocity zones show essentially two rising structures, a long drawn out structure extended from southwest to northeast and a nearly elliptical one between 7100-8300[m] (*Figure 52*).

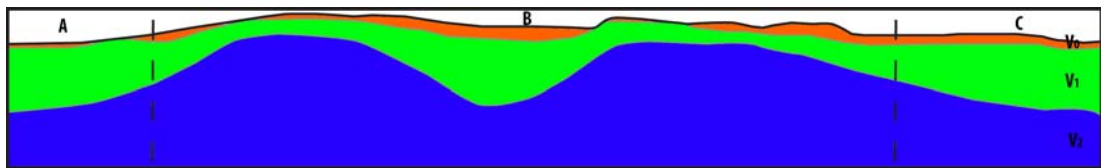


Figure 51: Schematically 2D velocity model ($V_0 = 800-1500$ [m/s]), $V_1 = 1500-3200$ [m/s] and $V_2 = 3200-5000$ [m/s]). In the middle part of the survey area HVZ reaches nearly the surface at some positions (part B). The dashed line indicates the assumed position of rising Mesozoic wedges, since weathering and loose masses reduce rock velocities.

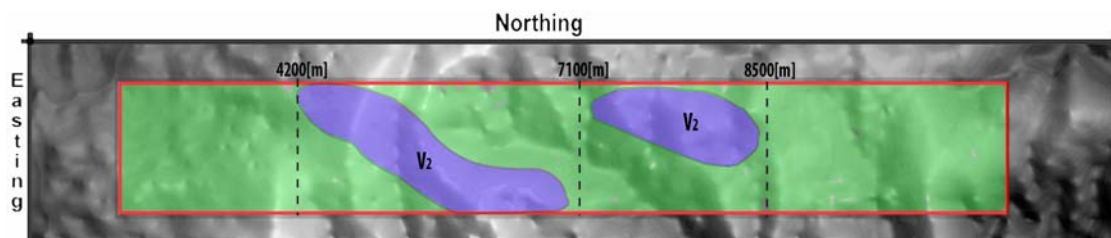


Figure 52: Depth slice through the model with shallow positions of the high velocity zone at a depth of 100[m].

5.2 3D travel time tomography with different initial models

The basic algorithm of this tomographic imaging is the back-projection method by *Hole, J. A., 1992*. Beside estimated travel times, the starting-model is one of the most crucial factors for resolving satisfying results. In this section a simple 1D initial model and a 3D initial model are used to investigate the dependency of the method on initial models.

5.2.1 Processing of nonlinear 3D travel time tomography

The basis for 3D travel time tomography by Hole is the modified ASCII file (*Section 3.2.1*); those traces were sorted by source index number (SIN) and absolute offset. This is an important pre-condition to generate two files containing precise geometry information of every source (*Table 4 and Table 5*). The accomplishment of the program *mk_hirhip* generates these files and over and above an input file (*.his file*)

with an additional elevation shift of 500[m] to prepare data for tomography inherent demands.

| | |
|--------------------|-----------------------|
| SRF_loc | Receiver Index Number |
| FB_Mayerlin | First Breaks |
| Aoffset | Absolute Offset |

Table 4: *.hip file* with associated parameters

| | |
|-----------------|---|
| SRF_loc | Receiver Index Number |
| Sou_Elev | Z coordinate (elevation) of the source |
| dx | relative X-coordinate from source to receiver |
| dy | relative Y-coordinate from source to receiver |

Table 5: *.hir file* with associated parameters

Beside the already mentioned elevation shift, the **maxpickoff parameter** was defined, which controls the maximum radial distance within first break picks will be processed. So all first break picks within an offset of 0.3[km] and finally all first break picks within an offset of 5[km], which is tantamount to the entirety of first break picks, were used. The **smoothing parameters** control the way of iteration. On the one hand side they control interpolation of data between the x-, y- and z-nodes ($N_x N_y N_z$) and on the other hand side the quantity of them controls the number of iterations. For this forward modelling scheme 6 iterations were defined in a control file (*Table 6*).

| | |
|-------------------------------|--|
| set shfile= name.his | name and prefix of the input file |
| set v1dfile= vo.v1d | initial velocity model |
| set zshift=0.5 | defines a elevation shift of 500[m] |
| set maxpickoff=(0.3 5) | defines an area within a radius of 0.3 and 5[km] |
| set smthx=(20 10 6) | smoothing parameters in X-direction |
| set smthy=(20 10 6) | smoothing parameters in Y-direction |
| set smthz=(10 6 2) | smoothing parameters in Z-direction |
| set mvax=(21 11 7) | smoothing parameters in X-direction |
| set mvay=(21 11 7) | smoothing parameters in Y-direction |
| set mvaz=(11 7 3) | smoothing parameters in Z-direction |

Table 6: Processing control file with the most important parameters of travel time tomography.

The layout of the processed survey area was divided into two overlapping parts in respect to their source number index (SIN), due to computational limitations (*Figure 53*).

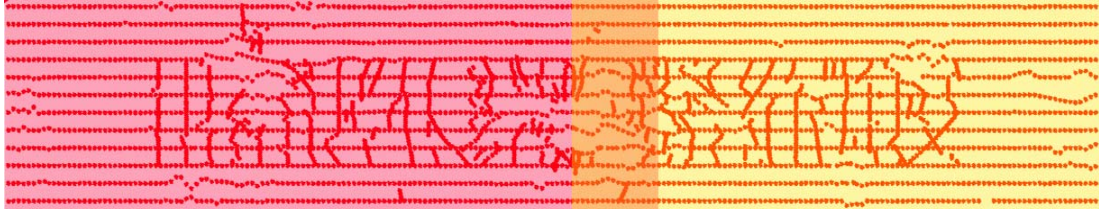


Figure 53: The entire layout from south to north (from left to right) divided into two overlapping parts. The southern part is assigned to `streif1_part1` (red area) containing source points 1-630 and the northern part is assigned to `streif1-part2` (yellow area) containing source points 530-1150.

The execution of travel time tomography was started by the command `hi++` and requires the control file, an initial velocity model (Section 5.2.2) as well as a `.log file`, which records the progress of travel time tomography in the background.

The calculated travel times were stored in a binary output file and were transformed to an ASCII file containing the number of velocity nodes, the origin of the model space, cell size and appropriate shifts (Table 7). Those cells, which were not penetrated by rays during iteration, were removed by utilizing a mask. Finally two ASCII files were generated and will be discussed in Section 5.2.3.

| | |
|--------------------|--------------------------------|
| 0x=600 | X-coordinate of the origin |
| 0y=1900 | Y-coordinate of the origin |
| 0z=0 | Z-coordinate of the origin |
| Nx=121 | Number of nodes in X-direction |
| Ny=941 | Number of nodes in Y-direction |
| Nz=101 | Number of nodes in Z-direction |
| H=10 | Cell size |
| x-shift=0 | Shift in X-direction |
| y-shift=0 | Shift in Y-direction |
| z-shift=0.5 | Shift in Z-direction |

Table 7: Geometric parameters defined in a control file and used to create ASCII files.

5.2.2 1D and 3D starting models for travel time tomography

Choosing a proper initial model is often more complex than ray tracing. Usually, the whole model is divided into individual layers and/or blocks by interfaces of the first order. The interfaces and the velocity distributions within individual layers should be sufficiently smooth to guarantee the application of the ray method (Cerveny, V., 1985). The 1D initial model is a velocity–depth model and consists of a cubic set of data points containing velocity information as a function of depth, named as $V_{Inv_start}^{1D}$. The model is spanned up by all in all 11.499.961 velocity nodes with a vertical varying velocity distribution (Table 8).

| | |
|--------------------------|--------------------------------|
| N_x=121 | Number of nodes in X-direction |
| N_y=941 | Number of nodes in Y-direction |
| N_z=101 | Number of nodes in Z-direction |
| SSI=10 | Spatial sample interval [m] |

Table 8: 3D grid with cubic spaced velocity nodes.

The vertical velocity distribution was defined as polynomial approximation of the second order (*Figure 54*) and assigned to velocity nodes of the 3D model.

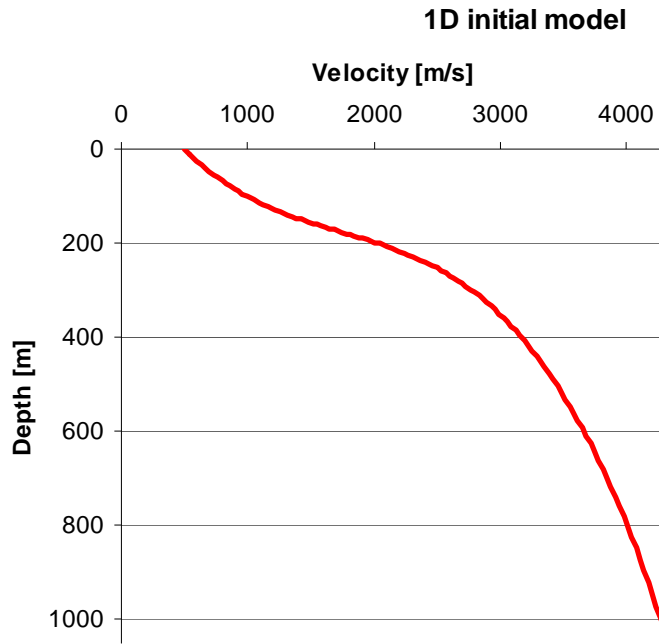


Figure 54: 1D velocity function as a polynomial approximation of the second order.

The 3D initial model was derived from the velocity model V_{Inv}^{1D} based on 1D ray tracing and inversion (*Section 5.1*). Peak anomalous values were spatially spread over the model space, such that only prominent subsurface structures remain. Below an iso surface defined by velocities equal to 3500[m/s], constant velocity values were assigned to the grid cells. To ensure the returning of deep penetrating rays, an additional slight velocity gradient was applied.

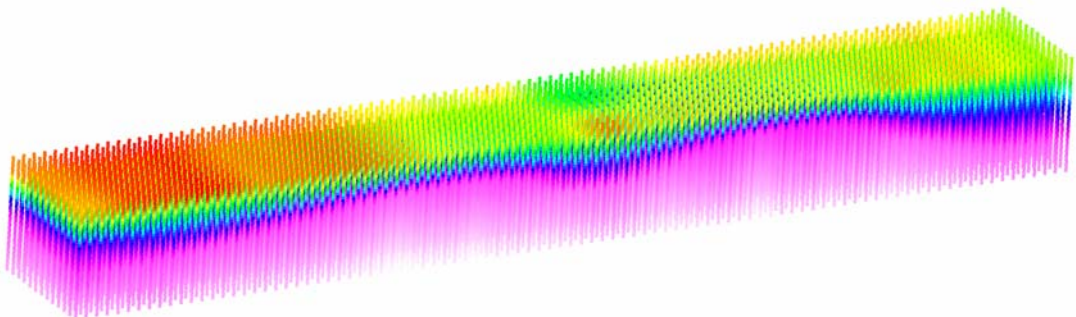


Figure 55: Strongly smoothed 3D initial model $V_{H_start}^{3D}$ obtained by 1D ray tracing & inversion.

5.2.3 Results

The processing sequence utilized in *Section 5.2.1* is called layer stripping, where the upper layers are constrained in the beginning by restricting the offset of the used pick and offers data sets containing velocity information for two overlapping parts of the model that will be finally merged. Beside already mentioned iteration parameters, the number of calculated travel times and the root mean square (RMS) error between observed and calculated travel times are listed in an iteration report for a travel time tomography with a 1D initial model (*Table 9* and *Table 10*).

| Max. offset [km] | Smoothing x/y [km] | Smoothing z [km] | Nr. of iterations | Calculated travel times | RMS error [s] |
|------------------|--------------------|------------------|-------------------|-------------------------|---------------|
| 2 | 20 | 10 | 1 | 167118 | 0,080 |
| 2 | 10 | 6 | 1 | 166527 | 0,030 |
| 2 | 6 | 2 | 1 | 166130 | 0,030 |
| 5 | 20 | 10 | 1 | 165747 | 0,020 |
| 5 | 10 | 6 | 1 | 165696 | 0,020 |
| 5 | 6 | 2 | 1 | 165543 | 0,020 |

Table 9: Iteration report of V_H^{1D} (part one) containing smoothing parameters, the number of travel times and the RMS error after each iteration.

| Max. offset [km] | Smoothing x/y [km] | Smoothing z [km] | Nr. of iterations | Calculated travel times | RMS error [s] |
|------------------|--------------------|------------------|-------------------|-------------------------|---------------|
| 2 | 20 | 10 | 1 | 178206 | 0,080 |
| 2 | 10 | 6 | 1 | 177959 | 0,040 |
| 2 | 6 | 2 | 1 | 176468 | 0,040 |
| 5 | 20 | 10 | 1 | 175790 | 0,030 |
| 5 | 10 | 6 | 1 | 175731 | 0,030 |
| 5 | 6 | 2 | 1 | 175576 | 0,030 |

Table 10: Iteration report of V_H^{1D} (part two) containing smoothing parameters, the number of travel times and the RMS error after each iteration.

The iteration report for a travel time tomography with a 3D initial model is listed in *Table 11* and *Table 12*.

| Max. offset [km] | Smoothing x/y [km] | Smoothing z [km] | Nr. of iterations | Calculated travel times | RMS error [s] |
|------------------|--------------------|------------------|-------------------|-------------------------|---------------|
| 2 | 20 | 10 | 1 | 167108 | 0,040 |
| 2 | 10 | 6 | 1 | 166731 | 0,030 |
| 2 | 6 | 2 | 1 | 165988 | 0,030 |
| 5 | 20 | 10 | 1 | 167596 | 0,020 |
| 5 | 10 | 6 | 1 | 166426 | 0,020 |
| 5 | 6 | 2 | 1 | 166255 | 0,020 |

Table 11: Iteration report of V_H^{3D} (part one) containing smoothing parameters, the number of travel times and the RMS error after each iteration.

| Max. offset [km] | Smoothing x/y [km] | Smoothing z [km] | Nr. of iterations | Calculated travel times | RMS error [s] |
|------------------|--------------------|------------------|-------------------|-------------------------|---------------|
| 2 | 20 | 10 | 1 | 178239 | 0,050 |
| 2 | 10 | 6 | 1 | 178218 | 0,040 |
| 2 | 6 | 2 | 1 | 175339 | 0,040 |
| 5 | 20 | 10 | 1 | 176223 | 0,030 |
| 5 | 10 | 6 | 1 | 176185 | 0,030 |
| 5 | 6 | 2 | 1 | 175969 | 0,030 |

Table 12: Iteration report of V_H^{3D} (part two) containing smoothing parameters, the number of travel times and the RMS error after each iteration.

In both cases the travel time residuals converge to 0.02[s] and to 0.03[s] for the first and the second partition of the survey area, respectively. Since the 3D initial model obtained from 1D inversion is closer to realistic near surface structures, the assigned travel time tomography converges faster without improving the final travel time error.

Similar to the results of 1D inversion the results of the travel time tomography with respect to their different initial models, the obtained velocity information were visualized by a Voxet. Since the spatial resolution of the used travel time tomography is higher than those of 1D inversion, cell sizes became smaller and the dimension of the velocity model was extended (*Table 13*).

| Origin of the Voxet | Number of grid points | End points of the Voxet |
|---------------------|-----------------------|----------------------------------|
| $X_0=750$ [m] | $N_u=10$ | point_u(X,Y,Z)=(1650, 2050, 450) |
| $Y_0=2050$ [m] | $N_v=92$ | point_v(X,Y,Z)=(750, 11150, 450) |
| $Z_0=450$ [m] | $N_w=64$ | point_w(X,Y,Z)=(750, 2050, -450) |

Table 13: Dimension and resolution of the final velocity models V_H^{1D} and V_H^{3D} derived by 3D travel time tomography.

The 3D velocity models were intersected in depth slices and cross sections at the same location as for those obtained by 1D inversion (*Section 5.1*). The selected depth slices and cross sections through the velocity models V_H^{1D} and V_H^{3D} based on a 1D- and 3D-initial model, respectively, along the z-axis (*Figure 56-Figure 57*), along the x-axis (*Figure 58-Figure 59*) and along the y-axis (*Figure 60-Figure 61*).

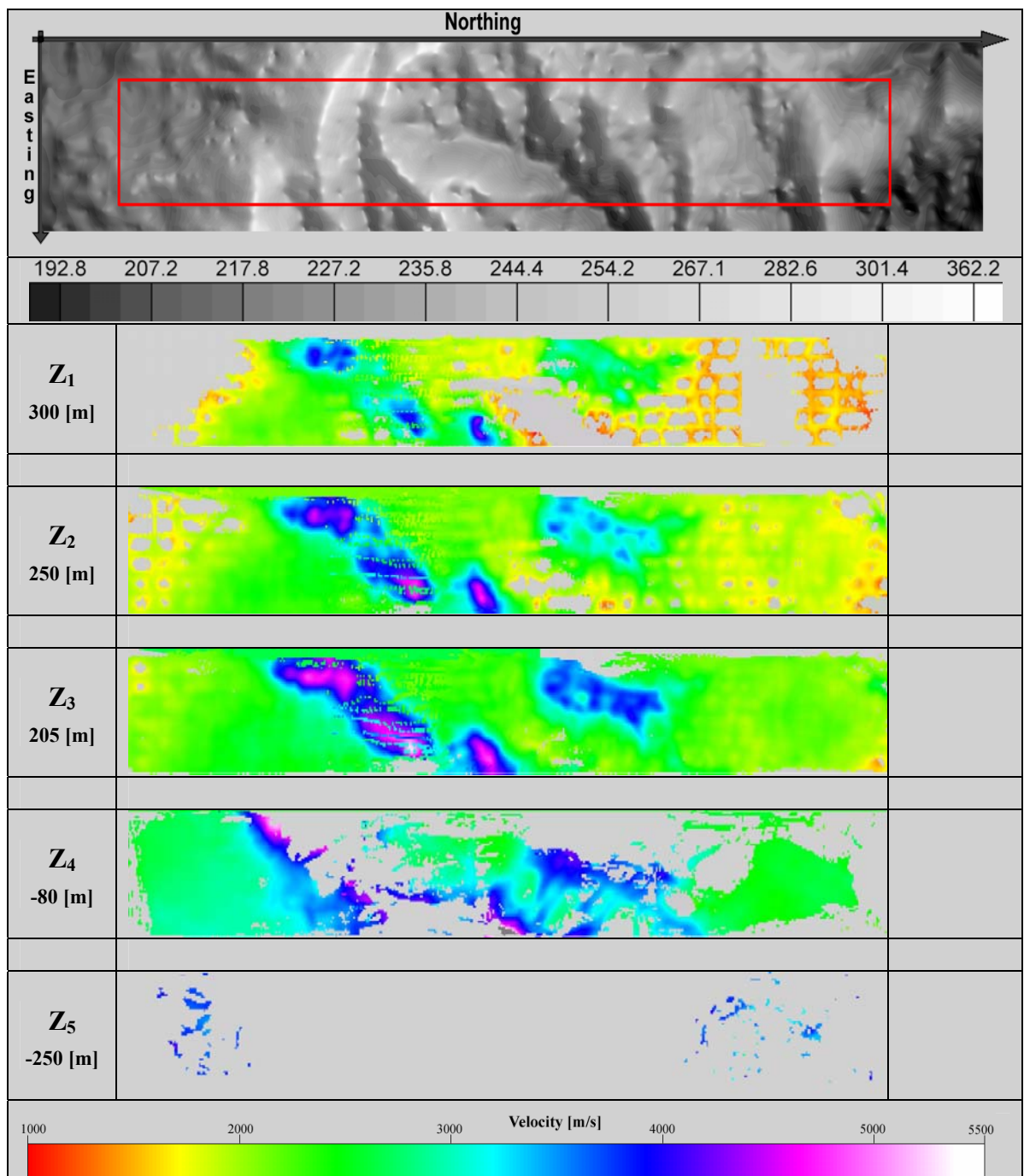


Figure 56: Depth slices along the z-axis (w-axis). The top part shows the surface relief, the processed survey area (red box), while the bottom part shows five depth slices through the seismic velocity model with increasing depth. The velocity model is based on iterative improvement of a 1D initial model by a 3D travel time tomography scheme.

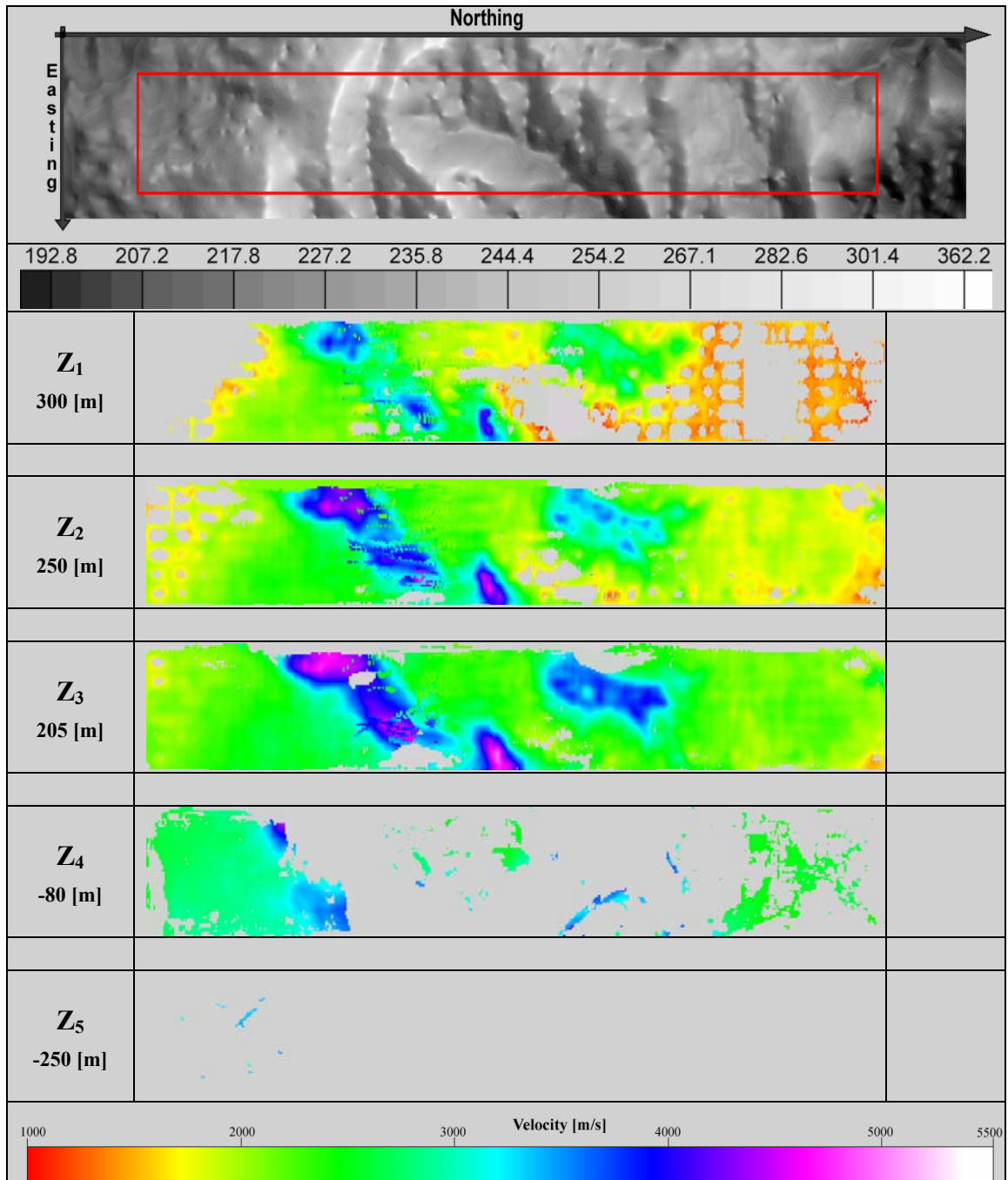


Figure 57: Depth slices along the z-axis (w-axis). The top part shows the surface relief, the processed survey area (red box), while the bottom part shows five depth slices through the seismic velocity model with increasing depth. The velocity model is based on iterative improvement of a 3D initial model by a 3D travel time tomography scheme.

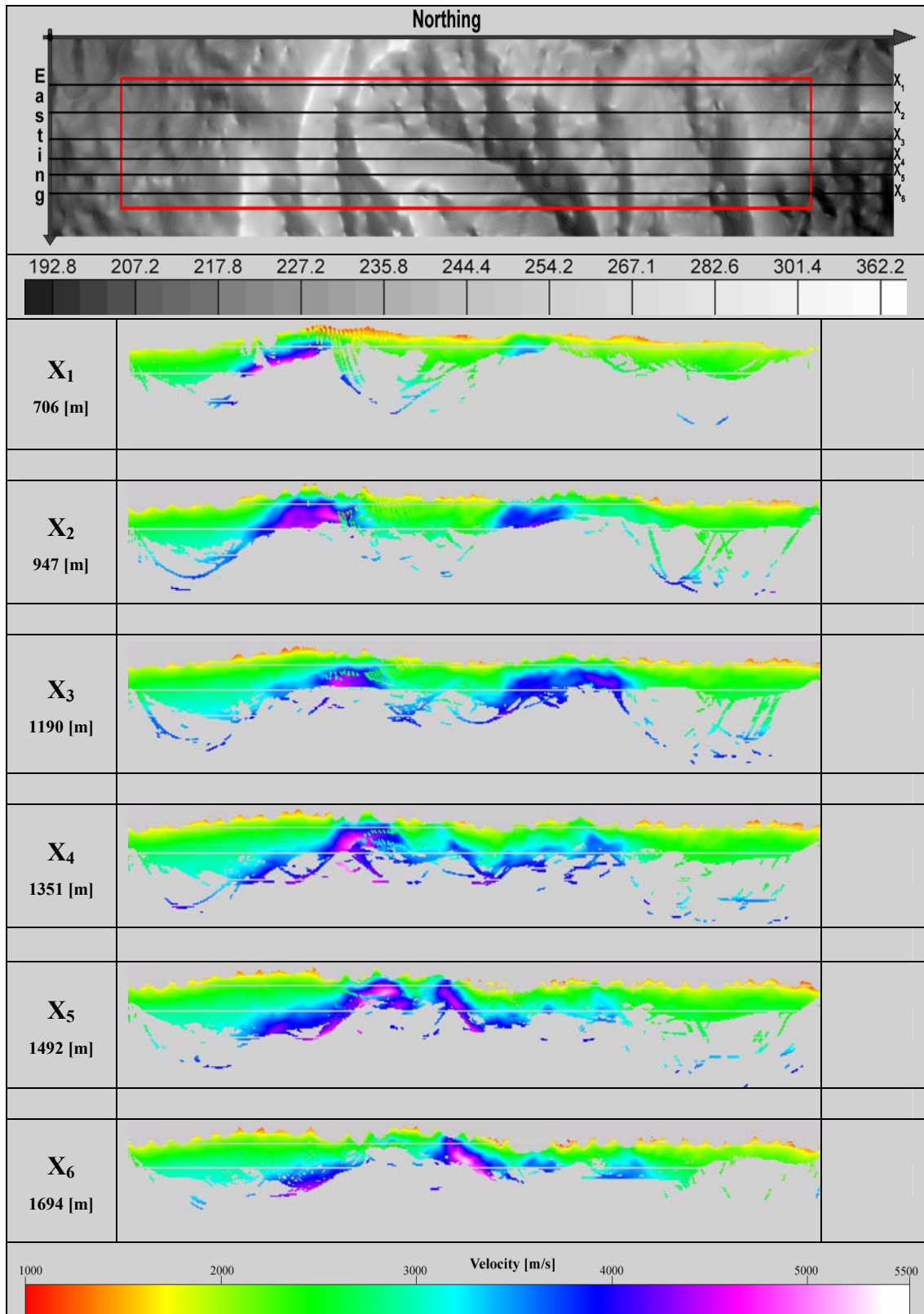


Figure 58: Cross sections along the x-axis (u-axis). The top part shows the surface relief and the processed survey area (red box), while the bottom part shows six cross sections through the seismic velocity model with increasing x-values. The velocity model is based on iterative improvement of a 1D initial model by a 3D travel time tomography scheme.

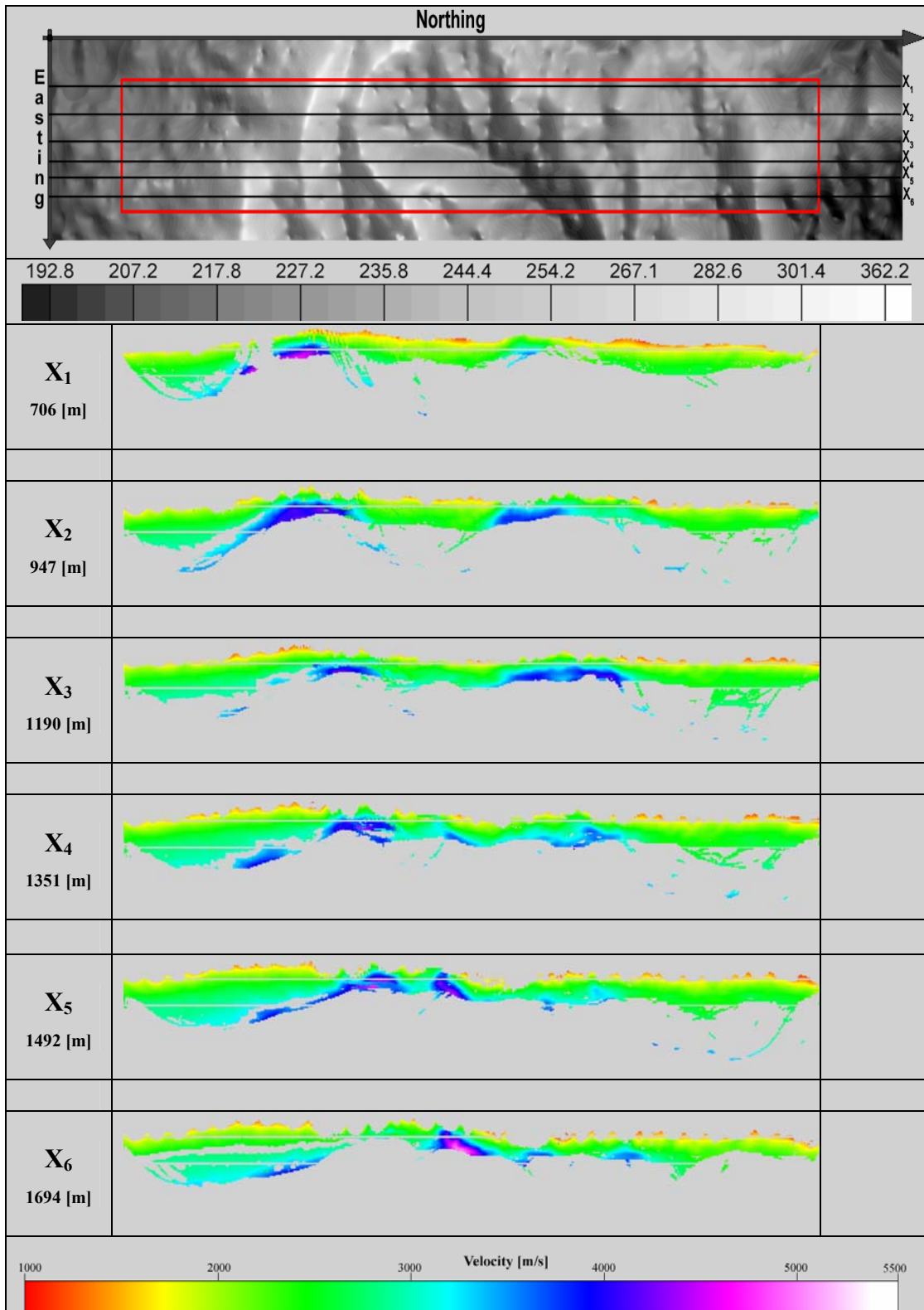


Figure 59: Cross sections along the x-axis (u-axis). The top part shows the surface relief and the processed survey area (red box), while the bottom part shows six cross sections through the seismic velocity model with increasing x-values. The velocity model is based on iterative improvement of a 3D initial model by a 3D travel time tomography scheme.

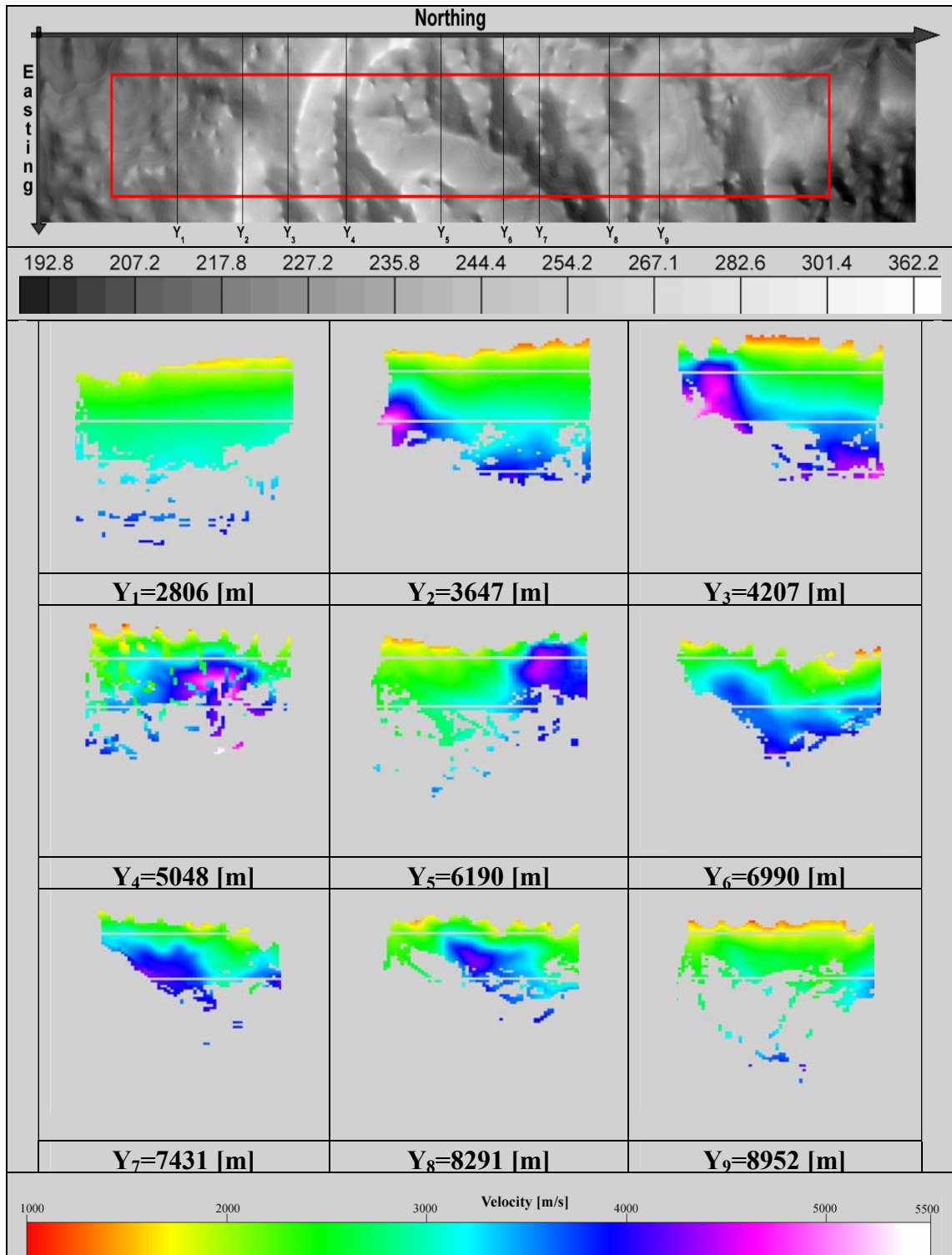


Figure 60: Cross sections along the y-axis (v-axis). The top part shows the surface relief and the processed survey area (red box), while the bottom part shows six cross sections through the seismic velocity model with increasing x-values. The velocity model is based on iterative improvement of a 1D initial model by a 3D travel time tomography scheme.

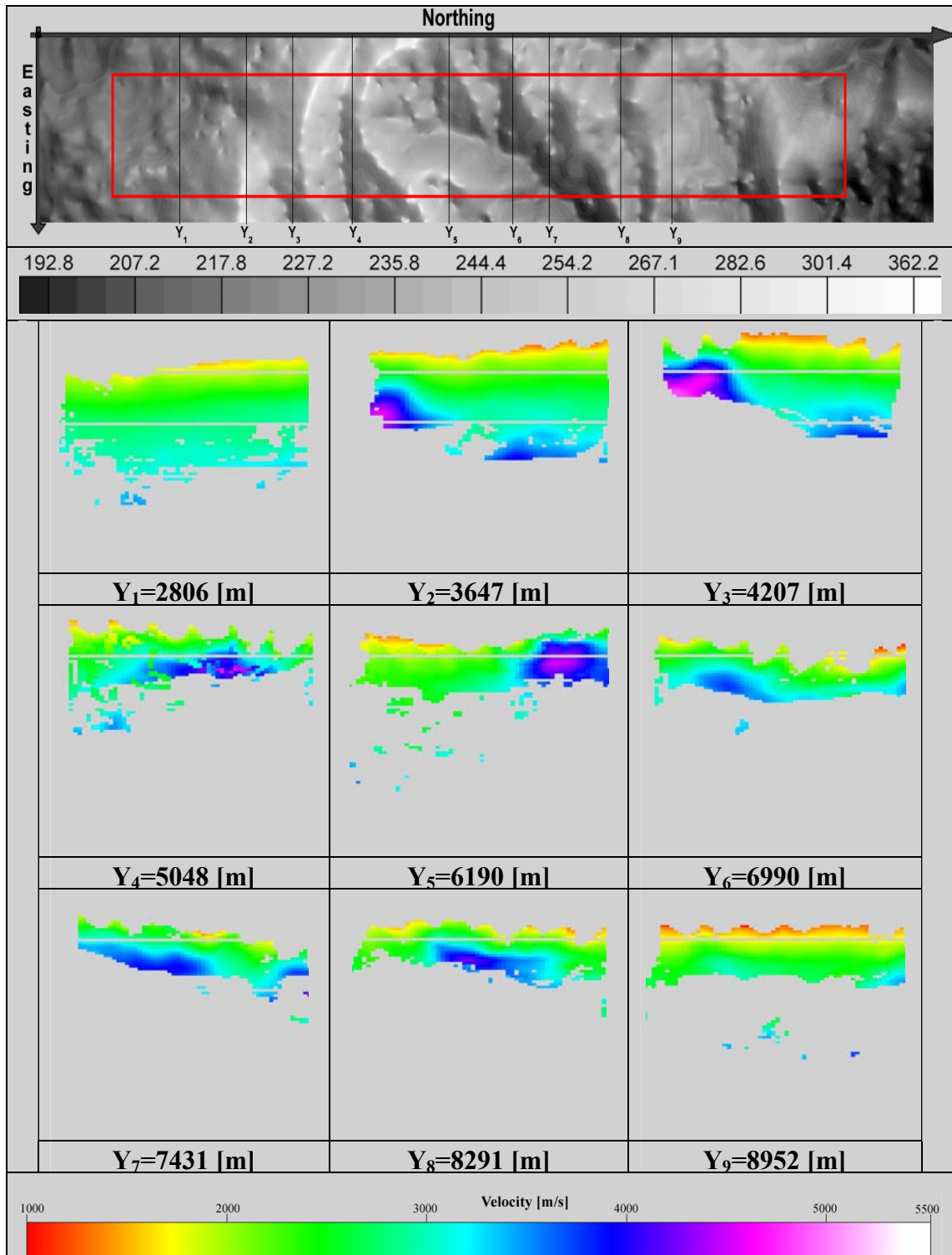


Figure 61: Cross sections along the y-axis (v-axis). The top part shows the surface relief and the processed survey area (red box), while the bottom part shows six cross sections through the seismic velocity model with increasing x-values. The velocity model is based on iterative improvement of a 3D initial model by a 3D travel time tomography scheme.

Both models show approximately the same lateral distribution of subsurface structures as the velocity model described in *Section 5.1*, although they are varying in velocity and penetration depth.

5.3 Comparison of velocity models

The analysis in areas with undulating topography requires a transformation of absolute heights into surface parallel depths, since the mean of seismic velocities, penetration depth and variance will be calculated. This transformation provides a surface consistent estimate of systematic characteristics and the model dependence of the particular results. So the velocity nodes are sorted by depth and for a 10[m] depth interval the mean velocity, the coverage of velocity nodes and the variance for each model are calculated.

Figure 62 shows a general increase of mean velocities for shallow structures down to approximately 200[m] of depth for all models. V_H^{1D} and V_H^{3D} show more or less the same constant velocity gradient down to 150[m], which is also congruent with the methodological independent 3D initial model $V_{H_start}^{3D}$. Below 150[m] to 200[m] the average velocity gradients become slight and both travel time tomography models differ constantly with 300[m/s], which can be considered as systematic gap between models for the Waschberg limestone. An interesting aspect provides the comparison of the final mean velocity models with their assigned initial models. While the considerably slower initial model $V_{H_start}^{1D}$ provides systematic higher velocity values for model V_H^{1D} compared to V_H^{3D} , which relies to comparative a faster initial model $V_{H_start}^{3D}$.

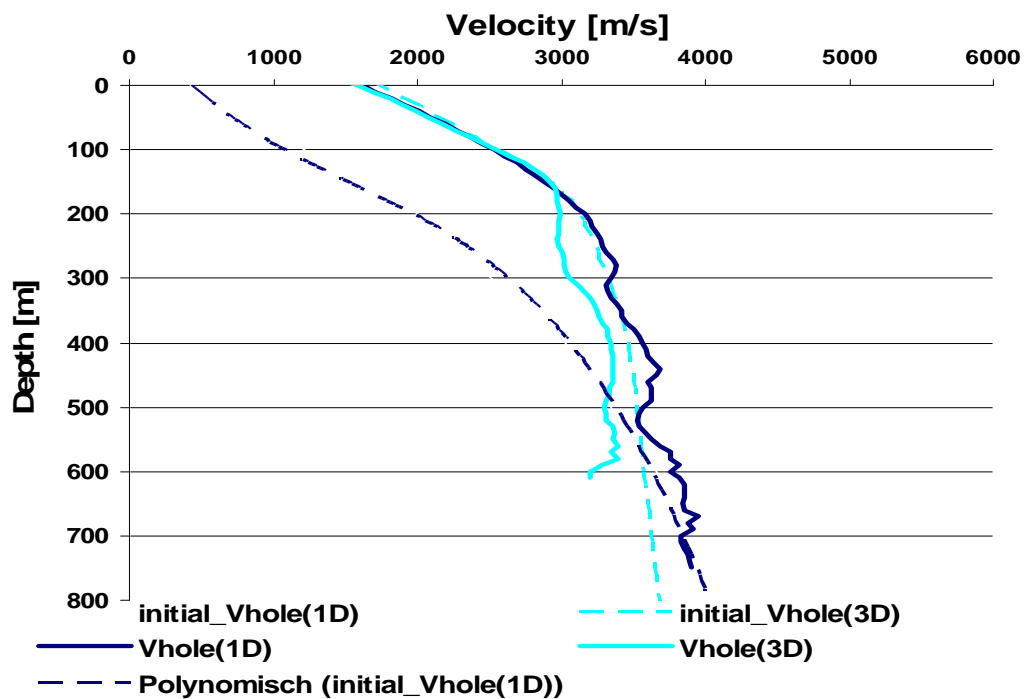


Figure 62: Mean velocity models V_H^{1D} (Vhole[1D]) and V_H^{3D} (Vhole[3D]) with respect to their initial models $V_{H_start}^{1D}$ (initial_Vhole[1D]) and $V_{H_start}^{3D}$ (initial_Vhole[3D]).

In general the ray coverage is quite sparse for that depths (> 400[m]), such that the results become unreliable for further interpretations or the use for static corrections (Figure 63).

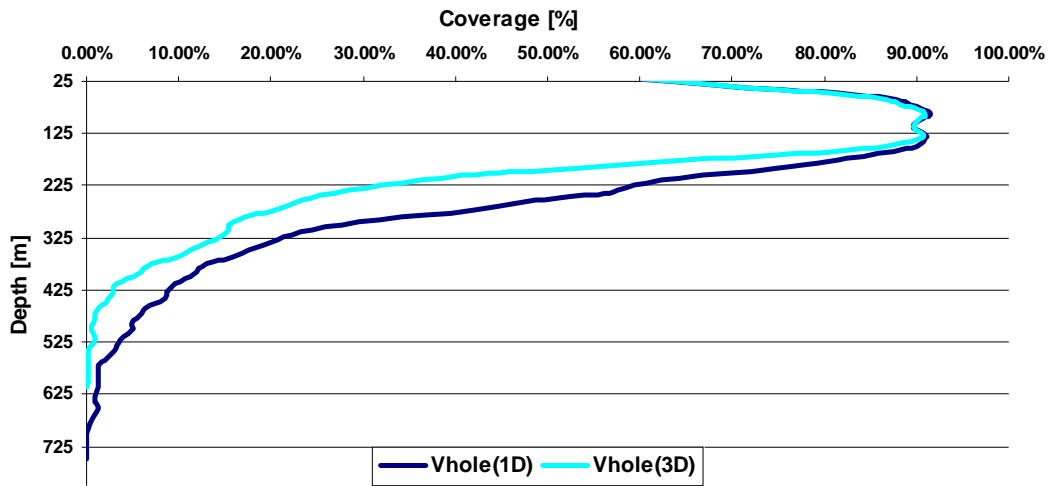


Figure 63: Model coverage as a function of depth.

The standard deviation of models increases for the first 200[m], which indicates a laterally varying subsurface resulting from the uprising high velocity zones in the velocity model. Below 200[m] the variations remain constant or decrease gradually and thus the lateral variability of the substratum also decreases. Comparing standard deviations of V_H^{3D} and V_H^{1D} highlights another interesting detail. In spite of the consistent RMS error (Section 5.2.3), V_H^{3D} has a lesser standard deviation, although it is the slightly smoother model.

Further V_H^{3D} shows lesser standard deviation than V_H^{1D} in spite of consistent RMS error of both models.

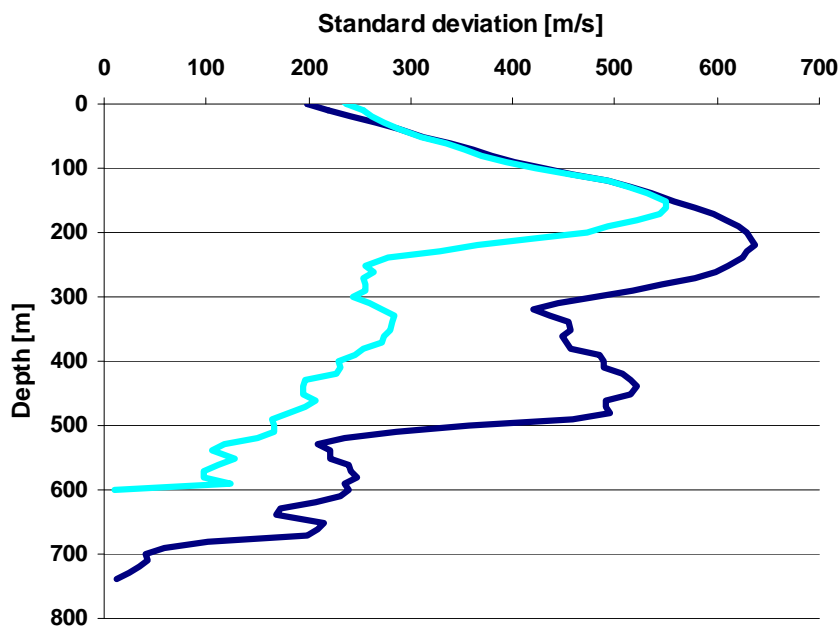


Figure 64: Standard deviation of V_H^{1D} (dark blue line) and V_H^{3D} (light blue line).

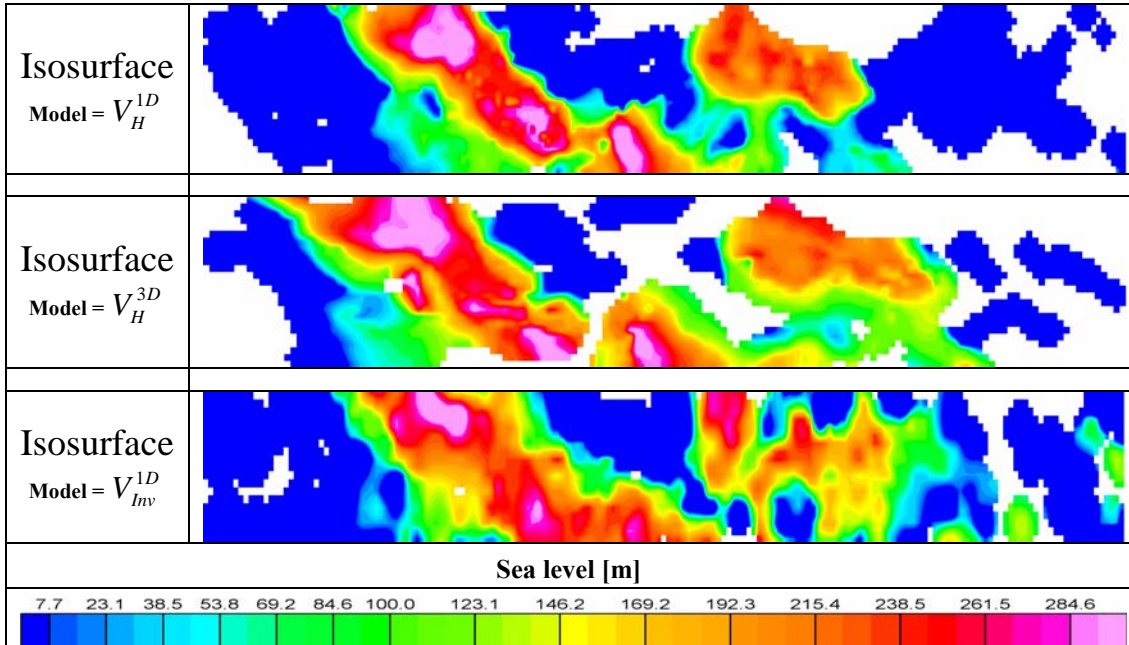


Figure 65: Iso-surfaces with constant velocity 3500[m/s] plotted over heights.

The analysis of the mean velocity is just an appraisal, which strongly depends on the three dimensional distribution of velocity nodes. For more precise information about the disparities between the applied methods, a qualitative analysis of cross sections through the difference models was accomplished (Figure 66). The visual interpretation of difference models confirms the fact that the significant disparities between V_H^{1D} and V_H^{3D} occur at high velocity zones dominated by the uprising limestone. In areas with relative constant velocity gradient and a sufficient thickness of the overburden, the investigated methods provide similar results. The differences between V_H^{1D} and V_H^{3D} feature a random distribution at the first glance, but detailed analysis shows that heterogeneity of velocity distribution increases in areas with uprising autochthones Mesozoic.

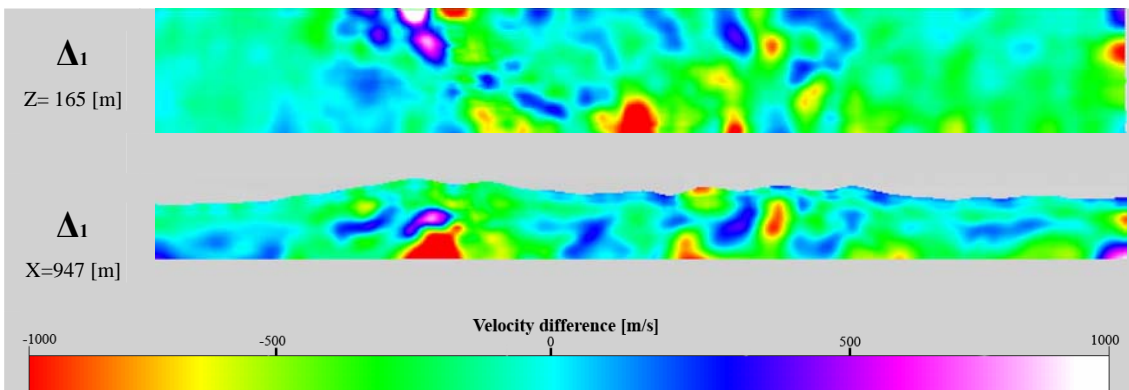


Figure 66: Typical depth slice and cross section through a velocity difference model along the z-axis and x-axis, respectively. Minimum and maximum values are limited with -1000[m/s] and 1000[m/s], respectively.

It can be summarized that velocity models vary from each other stronger in areas with strong velocity gradients and assign varying velocity values to expected

homogeneous structures (e.g. the heterogeneous and apparently arbitrary distributed model differences $\Delta t = V_H^{1D} - V_H^{3D}$). Since the ray paths are deeper in V_H^{1D} and the model indicates at least partial higher velocities than in V_H^{3D} , it can be assumed that longer ray paths require a stronger velocity gradient to fulfil the condition $\tau - \tau_0 = \delta\tau \rightarrow \min$. This additional gradient modifies the real gradient and thus leads to systematic higher velocities in certain areas. Initial models with fewer presumptions (1D initial model) tolerate more possible solutions than 3D initial models that restrict the possibilities of ray paths and thus the possibilities of velocity distribution. This hypothesis has to be proved in a several further tests with synthetic models.

6 Static correction

6.1 Computation of static correction

The different velocity models described in the previous section serve as basis for static correction (*Section 2.4*), which will be calculated for different datums. Further the influence of the inverted velocity models and vice versa the influence of the topography on the static correction will be estimated.

The analysis of the static correction based on mean velocities (*Figure 67*) reveals that the time shifts vary only marginally from each other for penetration depths up to 200[m]. Based on the maximum elevation of the survey area (418[m]), statics can be considered as model independent for a datum up to 200[m]. Below a datum of 200[m] static time shifts based on the velocity model V_{Inv}^{1D} and V_H^{3D} are systematically lower or higher, than that obtained by using model V_H^{1D} .

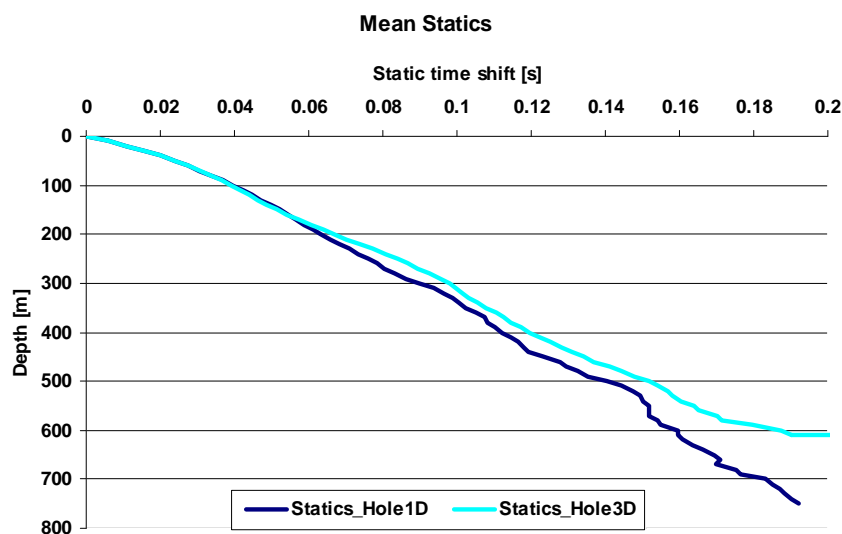


Figure 67: Static corrections based on the mean velocities.

Based on the smoothed velocity models V_H^{1D} , V_H^{3D} (Section 5.1.3 and Section 5.2.3) and the digital terrain model (DTM), the static correction for every grid point $t(P_j)$ of the survey area was calculated analogous to equation (1) as follows:

$$t(P_j) = \sum_{i=0}^n t_i = \sum_{i=0}^n \frac{(z_{i+1} - z_i)}{(v_{i+1} + v_i)} + \frac{(z_r - z_n)}{(v_r + v_n)} \quad (96)$$

where the dividend is the distance between two velocity nodes and the divisor represents the mean velocity between two velocity nodes. Further the statics based on the 3D initial model $V_{H_start}^{3D}$ was calculated to compare the structures of this methodological independent result with statics based on V_H^{1D} and V_H^{3D} .

Due to the diverse velocity models the choice of the datum is not trivial. Since analysis of mean velocities shows no model dependence of the static correction for penetration depths down to 200[m], the default datum in this area at 150[m] above sea level is ideal. The results in *Figure 68* map surface structures relative precise and additional tests confirm a significantly correlation with topography (*Appendix*). Based on the determined correlation coefficients r_{xy} and with

$$R^2 = (r_{xy})^2 \quad (97)$$

all models show nearly identical coefficients of determination R^2 , which represent the certainty in making predictions from the regression line. Practically the coefficient of determination means that all static models depend about 40 percent on elevation correction (*Table 14*).

| Model | Minimum [ms] | Maximum [ms] | Mean [ms] | Coefficient of determination |
|-------|--------------|--------------|-----------|------------------------------|
| T_1 | 34 | 115 | 71 | 0,43 |
| T_2 | 39 | 115 | 73 | 0,42 |
| T_3 | 39 | 114 | 73 | 0,70 |

Table 14: Significant parameters of static models with datum at 150[m] above sea level.

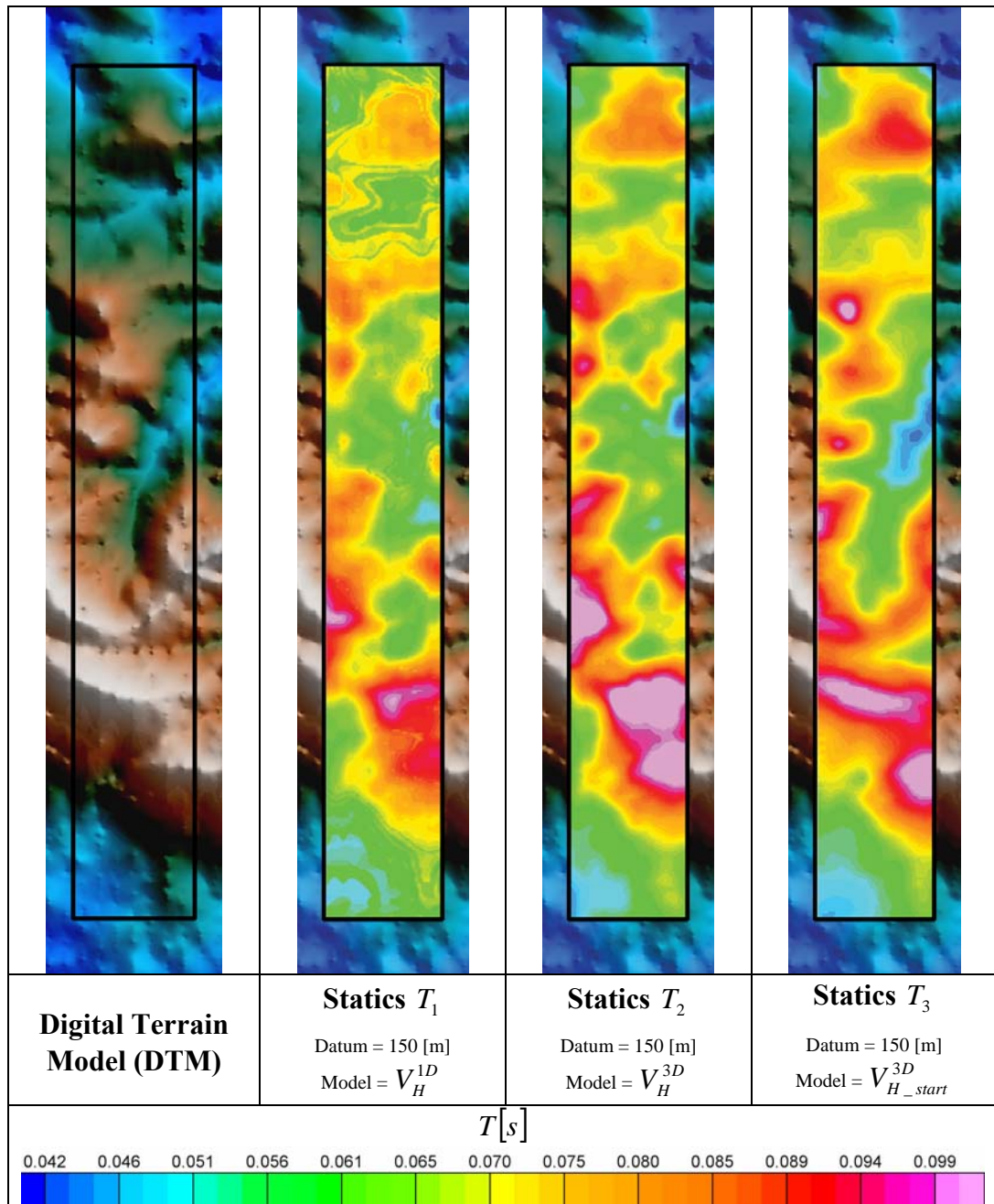


Figure 68: Static corrections down to a datum (=150[m] above sea level) by using different velocity models V_H^{1D} , V_H^{3D} and $V_{H_start}^{3D}$. The results of the different corrections are shown within the digital terrain model to highlight the correlation between the topography and the corrections.

To investigate the influence of velocity models on static correction results, the datum was chosen at 0[m] sea level and additional static corrections for all velocity models were calculated. As expected the influence of velocity models increases with depth and is confirmed by qualitative analysis of *Figure 69*, as well as by the coefficients of determination (*Table 15*). The dependence of static models on topography decreases in general and regional trends become more evident. Comparisons of reference statics T_3 with T_1 and T_2 show regional trends at the hilly structures north and south from the valley structure in the middle of the survey area (*Figure 70*).

| Model | Minimum [ms] | Maximum [ms] | Mean [ms] | Coefficient of determination |
|-------|--------------|--------------|-----------|------------------------------|
| T_1 | 80 | 183 | 123 | 0,11 |
| T_2 | 64 | 163 | 123 | 0,17 |
| T_3 | 83 | 161 | 120 | 0,43 |

Table 15: Significant parameters of static models with datum at 0[m] above sea level.

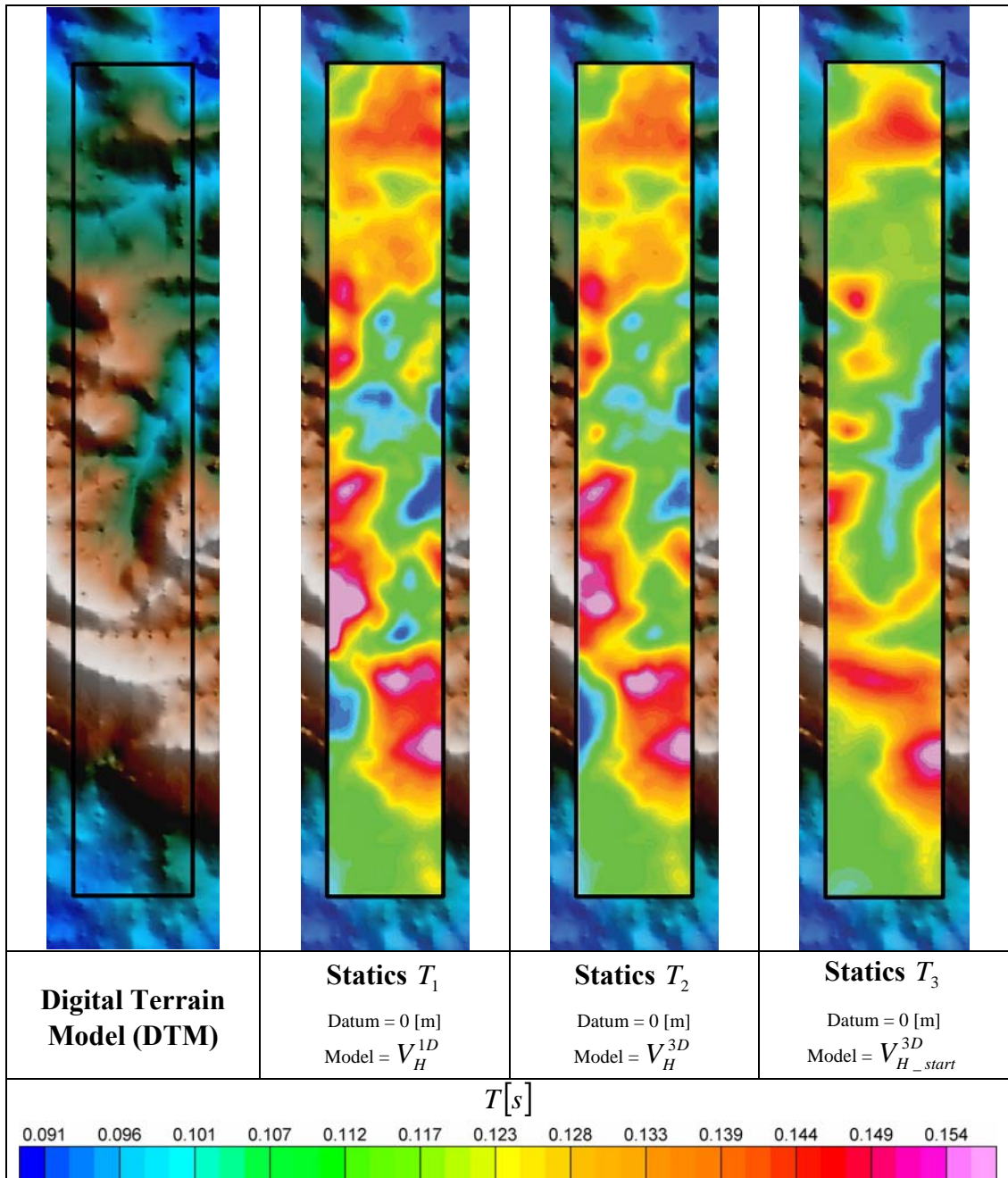


Figure 69: Static corrections down to a datum (=0[m] above sea level) by using different velocity models V_H^{1D} , V_H^{3D} and $V_{H_start}^{3D}$. The results of the different corrections are shown within the digital terrain model to highlight the correlation between the topography and the corrections.

Investigations show that final static corrections T_1 and T_2 depend for more than a half on the chosen velocity model at industrial standard datum. This dependence increases for deeper sections and systematic disparities would be amplified, but differences both models are generally constrained to local variations (*Figure 70*).

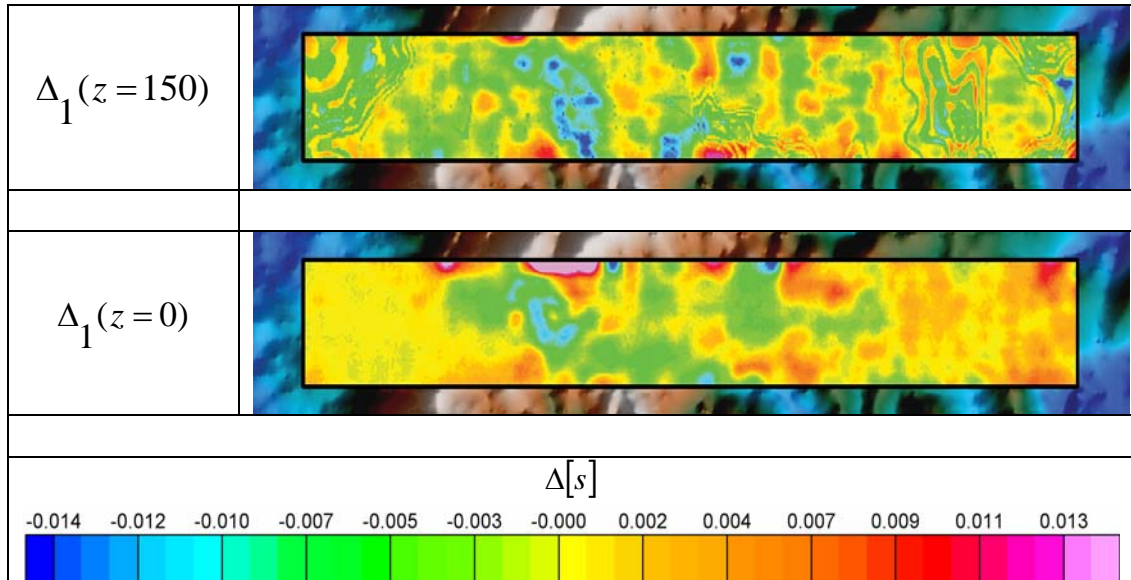


Figure 70: Model differences between calculated static corrections expressed as $\Delta_1(z = 150) = T_1 - T_2$ and $\Delta_1(z = 0) = T_1 - T_2$ at datum 150[m] and datum 0[m], respectively.

6.2 Comparison of static corrections with uphole times

Making assertions about model quality require comparisons of models with direct measured seismic information, like uphole time measurements. These uphole times were recorded during 35 borehole measurements and three of them are located in the investigated survey area (*Figure 71*). WBZ 2 and WBZ 6 are 100[m] deep drillings in the northern part of the survey area near Stützenhofen, while WBZ 7 is a 40[m] deep drilling investigating the near surface structures of one of three hills near the village Falkenstein, called Höllenstein. WBZ 2 and WBZ 6 show a systematic shift compared with their assigned statics T_2 due to the missing weathering layer in velocity model V_H^{3D} . This 6-10[m] thick weathering layer features an average velocity with 600[m/s] and cannot be resolved by the chosen receiver layout. WBZ 7 shows an additional characteristic, since the shallow structure of the Waschberg limestone (3800[m/s]) decreases static correction in comparison with T_2 , which does not detect this formation. On the contrary to WBZ 7 the virtual drilling in *Figure 72* does not penetrate the Waschberg limestone, which is steeply dipping in this section.

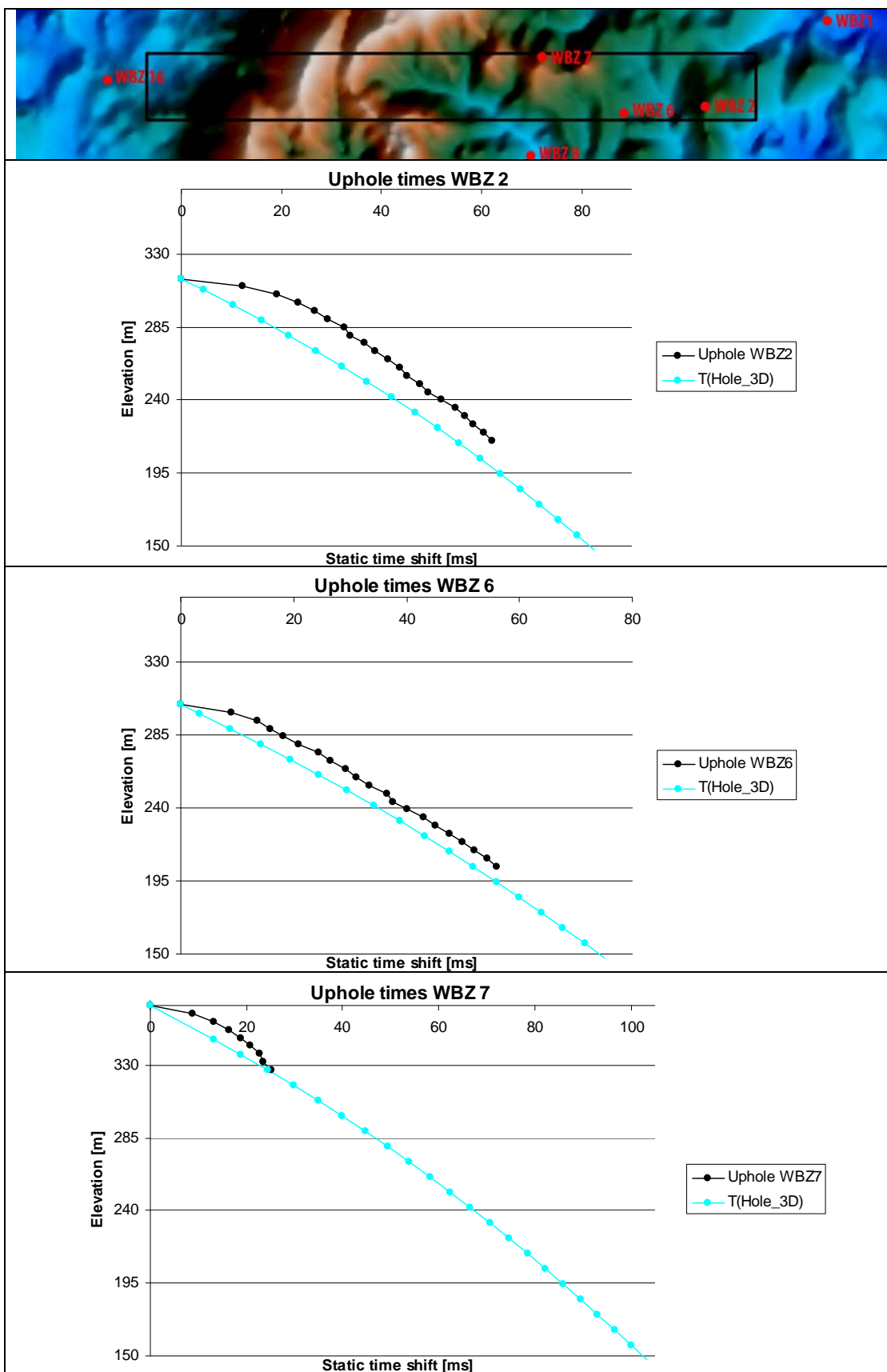


Figure 71: The top part show positions of uphole measurements in the selected survey area. The black frame indicates the model area of T_2 . The bottom part represents the results for the uphole time measurements and for the static model T_2 at the borehole position.

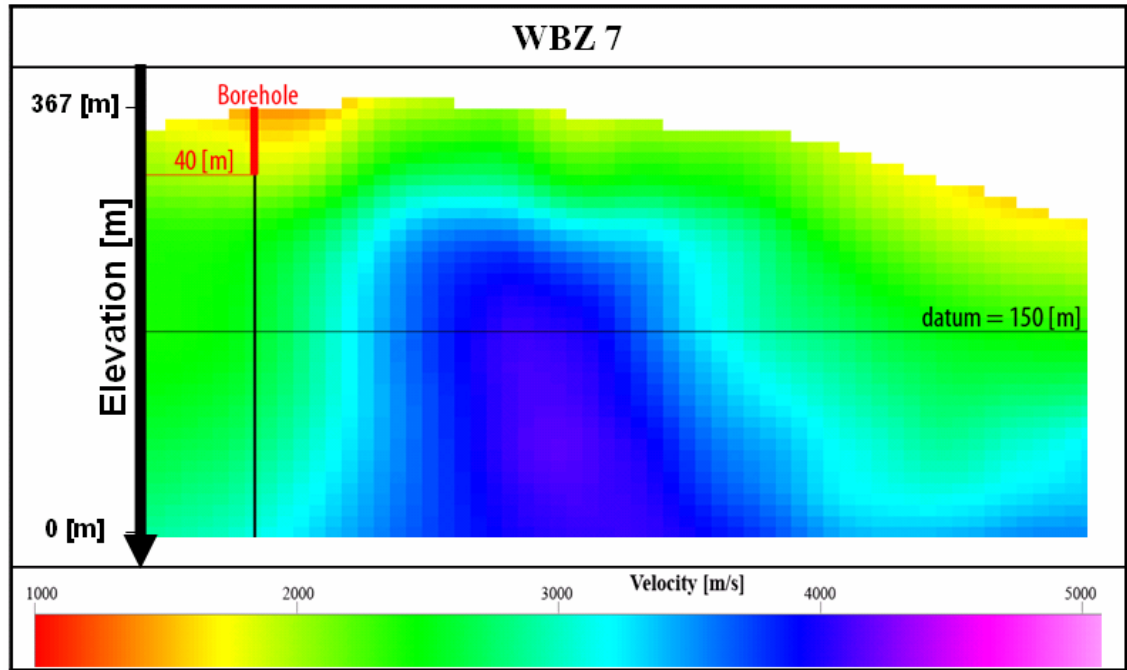


Figure 72: Cross section through V_H^{3D} along the x-axis at borehole WBZ 7.

7 Conclusions

The objective of this thesis was the computation of static corrections for the geological and tectonical complex Waschbergzone1 near the Czech border. Various 3D velocity models created independently from each other, served as basic for this important step in seismic processing. The 3D velocity model V_{Inv}^{1D} is based on travel times obtained from CMP-sorted and stacked data, which are inverted for locally varying 1D velocity-depth functions. In contrast, the 3D velocity models V_H^{1D} and V_H^{3D} are calculated with a 3D travel time tomography by using travel times of unstacked single traces. Both velocity models vary only in the utilization of different initial models (e.g. 1D- and 3D initial model).

V_H^{1D} and V_H^{3D} , for depths down to 200[m], feature a very similar mean velocity-depth relation and a high coverage. Below that depth representing the mean depth of the strongly undulating upper part of the Waschberg limestone and the maximum of the standard deviation, the coverage decreases. The mean velocity of V_H^{1D} appears to be 300[m/s] higher than in V_H^{3D} and visual inspection shows that the reason for this behaviour are local variations of the Waschberg limestone velocity. The local variations are associated with the decrease of coverage below the upper part of limestone. This decrease leads to fewer model improvements during the iteration process and, thus, to fewer modifications of the initial model. This fact inevitably results the influence from the chosen velocity gradient in the initial model. Compared to the 3D initial model of V_H^{3D} , the 1D initial model has an essentially lower velocity

gradient. On the one hand, this fact allows rays to penetrate deeper, but on the other hand, they have to pass through seismically faster media due to the constantly remaining residuals between observed and calculated travel times.

The large-scale structures of the of the Waschberg limestone are very similar in all three models and lead to the assumption that structure analysis is independent from the chosen method. Minor changes of structures, as well as velocity differences, exclusively occur in the middle part of the survey area. This part shows a rougher topography with up to 420[m] high hills surrounding the village Falkenstein and indicates shallow positions of the Waschberg limestone. Sections with a thicker sedimental overburden in the northeast and the southwest of the survey area indicate only marginal differences.

The velocity models V_H^{1D} and V_H^{3D} were chosen for the computation of static corrections T_1 and T_2 , respectively, since they show a more homogeneous and geologically reasonable velocity distribution of the Waschberg limestone and a better coverage with respect to the chosen datum at 150[m], in comparison with V_{Inv}^{1D} . Either static correction indicates, similar to the associated velocity models, only local differences in sections of uprising Waschberg limestone. To two-thirds, they depend on the velocity models at a datum of 150[m]. The static correction T_2 is recommended, since V_H^{3D} provides a more homogeneous result than V_H^{1D} , although the adjustment of travel times is steadily approaching the same RMS error.

Comparisons to three uphole time measurements show, except for a systematic shift, similar results. The systematic shift occurs due to the missing determination of the first weathering layer with a velocity and thickness of 600[m/s] and 5-10[m], respectively. Another judgement of the model quality would be the implementation of the computed static corrections into the seismic processing and the comparison of various seismic sections by OMV.

Regardless of the actual results, some assertions about methodological characteristics, processing efforts and computational cost of particular methods can be made. 3D modelling of subsurface velocities by local 1D velocity-depth functions is definitely faster, since picking travel times from stacked traces and the subsequent computation demands less time than picking travel times from the original record sections and the subsequent 3D travel time tomography.

8 References

Literature:

Aki, K., Christoffersson, A., Husebye, E.S., 1977, Determination of the three-dimensional seismic structure of the lithosphere, *Geophysical Research*, 82, 277-296

Aki, K., Richards, P., 2002, *Quantitative Seismology*, Second Edition, University Science Books

Behm, M., Brückl, E., Chwatal, W., Thybo, H., 2007, Application of stacking and inversion techniques to three-dimensional wide-angle reflection and refraction seismic data of the Eastern Alps, *Geophysical Journal*, 170, 275-298

Berryhill, J., 1979, Wave-equation datuming, *Geophysics*, 44, 1329-1344

Bjerhammar, A., 1973, *Theory of errors and generalized matrix inverses*, Elsevier Scientific Publishing Company

Brix, F., 1993, *Erdöl und Erdgas in Österreich*, Naturhistorisches Museum Wien

Brückl, E., Bodoky, T., Hegedüs, E., Hrubcová, P., Gosar, A., Grad, M., Guterch, A., Hajnal, Z., Keller, G.R., Špicak, A., Sumanovic, F., Thybo, H., Weber, F. and ALP2002 WORKING GROUP, 2003, ALP2002 Seismic Experiment. *Studia geophysica geodaetica*, Academy of Sciences of the Czech Republic, 47, 671-679

Cerveny, V., 1985, The application of ray tracing to the numerical modelling of seismic wave fields in complex structures, *Seismic Shear waves, Part A: Theory*, 1-124, Geophysical Press, London

Cerveny, V., 1987, *Seismic Tomography, Ray tracing algorithms in three-dimensional laterally varying layered structures*, Reidel publishing Company, 99-133

Cox, M., 1999, *Static Corrections for Seismic Reflection Surveys*, Society of Exploration Geophysicists, 39-277

Dines, K.A. and Lytle, R.J., 1979, Computerized geophysical tomography. *Proceedings of the IEEE*, 67, 1065-1073

Eckart, G. and Young, G., 1939, A principal axis transformation for non-Hermitian matrices, *Bull. American Math. Soc.*, 45, 118-121

- Guterch, A., Grad, M., Špicak, A., Brückl, E., Hegedüs, E., Keller, G.R., Thybo, H. and CELEBRATION 2000, ALP2002, SUDETES 2003 WORKING GROUPS, 2003**, An Overview of Recent Seismic Refraction Experiments in Central Europe. *Studia geophysica geodaetica*, Academy of Sciences of the Czech Republic, 47, 651-657
- Hatton, L., 1986**, Seismic data processing: theory and practice, Blackwell Scientific Publications,
- Herndler, E., 2001**, Design of 3D Seismic Survey in the Waschbergzone Austria, OMV Internal Report, 11-59
- Hole, J.A., 1992**, Nonlinear High-Resolution Three-Dimensional Seismic Travel Time Tomography. *Journal of Geophysical Research*, 97, 6553-6562
- Koch, M., 1985a**, A theoretical and numerical study on the determination of the 3D structure of the lithosphere by linear and nonlinear inversion of teleseismic travel times, *Geophys. J. R.*, 80, 73-93
- Koch, M., 1992**, Geophysical inversion, Optimal regularization of the linear seismic inverse problem, Society for industrial and applied mathematics, Philadelphia, 170-234
- Lanczos, C., 1961**, Linear differential operators, D. van Nostrand, Co., London
- Menke, W., 1984**, The resolving power of cross hole tomography, *Geophysical Research Letter*, 11, 105-108;
- Michalena, R. J., and Harris, J. M., 1990**, Tomographic travelttime inversion using natural pixels, *Geophysics*, 56, 635-644
- Moczo, P., 2004**, Theory of seismic waves, Lecture notes, Comenius University Bratislava, 2-39
- Nelson, G. D. and Vidale, J. E., 1990**, Earthquake location with finite difference travel times in Bear Valley, *Bulletin of the Seismological Society of America*, 80, 395-410
- Nolet, G., 1987**, Seismic Tomography, Seismic wave propagation and seismic tomography, D. Reidel publishing Company, 1-23

Officer, C. B., 1958, Introduction to the theory of sound transmission. McGraw-Hill Book Company

Sambridge, M., Mosegaard, K., 2002, Monte Carlo methods in geophysical inverse problems, *Reviews of Geophysics.*, 40, 1009

Sheriff, R.E., 1991, *Encyclopaedic Dictionary of Exploration Geophysics*, Society of Exploration Geophysicists

Spitzer, R., 2001, 3D-Waschbergzone (I) Model for static corrections – phase1: Internal Report.

Stenonis, N., 1669; *Dissertationis prodromus*

Tikhonov, A., Arsenin, V., 1977, *Solution of ill-posed problems*, American Mathematical Society

Vidale, J. E., 1990, Finite-difference calculation of traveltimes in three dimensions, *Geophysics*, 55, 521-526

Yilmaz, Ö., 2001, *Seismic data analysis*, 2nd edition. Society of Exploration Geophysicists

9 Abstract

Static correction is an essential step during seismic processing and is utilized to minimize topographic and near surface effects due to inhomogeneous weathering layers. The objective of this thesis is the realization of static corrections based on different velocity models. Since static correction demands precise information about the velocity distribution in the subsurface, the used velocity models should image velocity structures as exact as possible. Two methodological different tomography techniques from lithosphere investigations were applied on a 3D seismic data set from oil industry to obtain seismic velocity models of geological and tectonically complex Waschberg unit near the Czech border. Alternatively to a 1D ray tracing and inversion scheme used to invert travel times of stacked traces, a 3D tomographic approach is used to invert travel times from the single fold section. Both methods are iteratively improved from simple 1D initial models and the result of stacking technique provides an additional 3D initial model for the 3D tomography technique. It turns out that dependency of the 3D tomography on the initial model occurring in areas with increasing geological complexity. The disparities between velocity models and the resulting static corrections are compared, investigated on systematic as well as regional effects and interpreted.

Kurzfassung

Die statische Korrektur stellt einen wesentlichen Schritt in der Auswertung reflexionsseismischer Daten dar. Diese Korrektur wird zur Eliminierung topographischer und Verwitterungseffekte herangezogen, indem man ein neues Bezugsniveau für die Empfänger seismischer Signale bestimmt. Das Ziel dieser Diplomarbeit ist die Berechnung von statischen Korrekturen basierend auf unterschiedlichen Geschwindigkeitsmodellen, die neben dem Geländemodell als wichtigste Eingangsgröße für präzise Korrekturen anzusehen sind. Zu diesem Zweck werden zwei methodologisch differente Methoden aus der Lithosphärenforschung auf einen 3D Datensatz der Erdölindustrie angewendet, um voneinander unterschiedliche Geschwindigkeitsmodelle der geologisch und tektonisch komplexen Waschbergzone nahe der tschechischen Grenze zu konstruieren. Dies wird einerseits durch Invertieren von Einzelaufzeiten im Rahmen einer 3D Tomographie, sowie andererseits durch Invertieren von Laufzeiten gestapelter Spuren mittels einer 1D Ray tracing- und Inversionsmethode verwirklicht. Beide Modelle beruhen auf der iterativen Verbesserung von frei gewählten 1D Startmodellen. Zusätzlich wird ein drittes Geschwindigkeitsmodell durch die 3D Tomographie geschaffen, dessen Startmodell aus dem Ergebnis der 1D Inversion erzeugt wurde. In den Modellabschnitten mit größerer geologischer Komplexität lässt sich dadurch zeigen, dass eine Modellabhängigkeit vom Startmodell gegeben ist und die Wahl des Startmodells daher nicht trivial ist. Weiters werden alle Geschwindigkeitsmodelle und die daraus resultierenden statischen Korrekturen miteinander verglichen, auf systematische sowie regionale Effekte untersucht und schlussendlich interpretiert.

10 Appendix

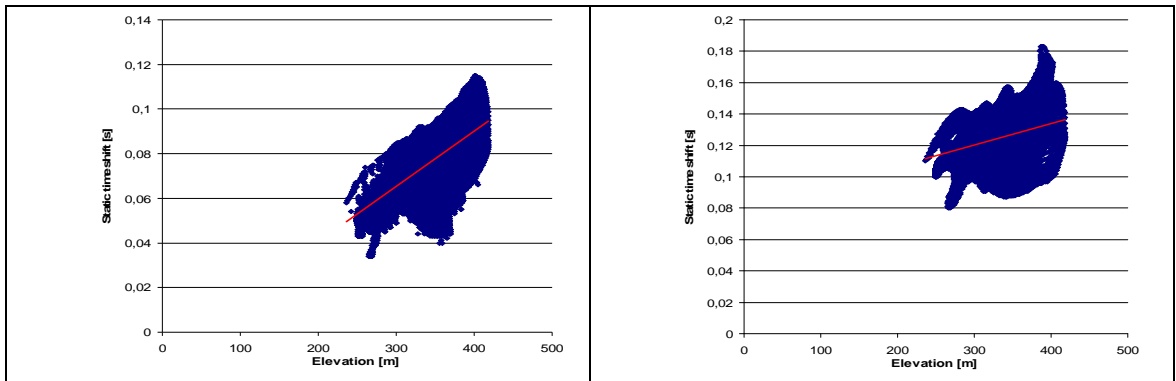


Figure 73: Height correlation of model T_1 at datum 150[m] (left diagram) and at datum 0[m] (right diagram) with correlation coefficients $r_{xy} = 0,65$ and $r_{xy} = 0,33$, respectively. The red line symbolizes the linear regression line through the scatter plot.

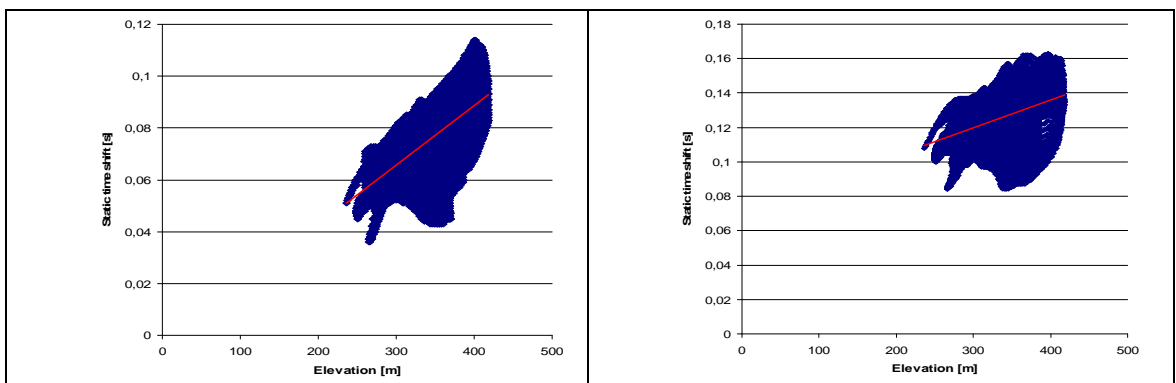


Figure 74: Height correlation of model T_2 at datum 150[m] (left diagram) and at datum 0[m] (right diagram) with correlation coefficients $r_{xy} = 0,65$ and $r_{xy} = 0,42$, respectively. The red line symbolizes the linear regression line through the scatter plot.

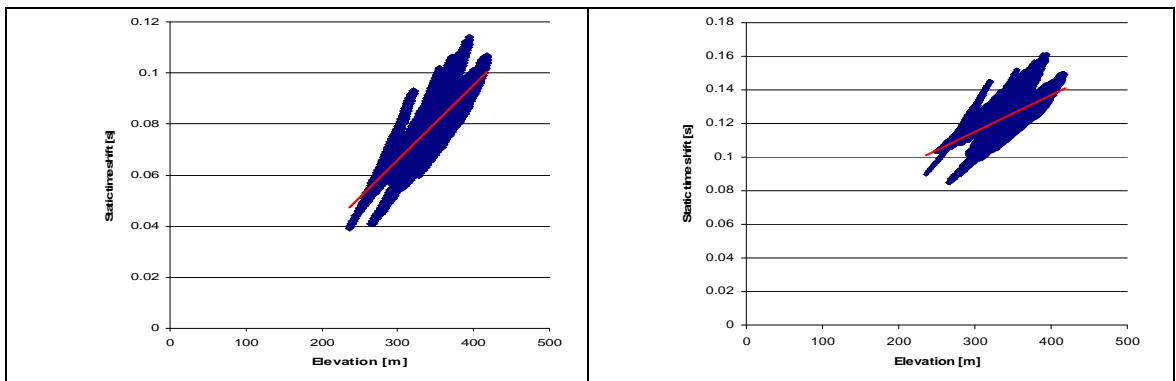


Figure 75: Height correlation of model T_3 at datum 150[m] (left diagram) and at datum 0[m] (right diagram) with correlation coefficients $r_{xy} = 0,66$ and $r_{xy} = 0,16$, respectively. The red line symbolizes the linear regression line through the scatter plot.

11 Curriculum Vitae

Personal Information

Name Klaus Mayer
Address Ludwig von Hoehnelgasse 9/113, 1100 Vienna,
Austria
Mobile phone +43-650-6376655
E-mail klaus.mayer@aon.at
Birth date 30th November 1978
Citizenship Austria

Education

10/1998 – 11/2008 **University of Vienna, Department of
Meteorology and Geophysics, Austria**
Master of Science (ISCED 5a)

- Principal subjects: Mathematics; Physics with focus on theoretical and applied geophysics
- Master thesis in English at the Technical University of Vienna – „Application of 3D tomography methods on a seismic 3D data set“

09/1993-06/1997 **BORG Murau focusing on natural scientific
Disciplines, Austria**
*Graduation diploma focusing on math and science
(ISCED 3a)*

- Award for the best student magazine of Styria
- Participation at Mathematical Olympiads with distinction

Other university activities

- GTTC course: The rock physics behind seismic amplitudes
www.gttc-vienna.at
- Certified Explosives Expert
www.baunat.boku.ac.at
- Research visits on the isle of Vulcano, Italy